Structure sensitivity of H_2/D_2 Isotopic Exchange on Pt/Al_2O_3 catalysts

Ricardo Pool Mazun

Thesis submitted to the Faculty of the

Virginia Polytechnic Institute and State University

in partial fulfillment of the requirements for the degree of

Master of Science

in

Chemical Engineering

Ayman M. Karim, Chair

John Morris

Hongliang Xin

August 9, 2022

Blacksburg, Virginia

Keywords: Heterogeneous catalysis, Kinetics, Hydrogen activation, Reactors engineering

Structure sensitivity of H_2/D_2 Isotopic Exchange on Pt/Al_2O_3 catalysts

Ricardo Pool Mazun

(ABSTRACT)

Pt-supported catalysts are widely used industrially for hydrogenation reactions. However, the kinetics of hydrogen activation, a critical step for any hydrogenation reaction, is still not well understood on supported Pt surfaces. Recent studies had shown that activity and selectivity vary with Pt nuclearity for the acetylene semihydrogenation reaction, increasing in activity and decreasing in selectivity while increasing the particle size from single atoms (SA) to sub-nanoclusters to nanoparticles (NP), attributing the cause of these differences on activities to the activity of H_2 activation in the H/D isotopic exchange reaction. In this work, the kinetics of H_2 is studied by performing the H_2-D_2 isotopic exchange reaction on Pt-supported catalysts with different nuclearity to extract the activation barriers and pre-exponential factors for dissociating adsorption and associative desorption (ΔE_{ads}, ΔE_{des} and v_{ads}, v_{des} respectively) from the microkinetic model derived from the Bonhoeffer Farkas mechanism, this to perform a more in-depth analysis regarding the differences in activity when comparing the H_2 adsorption energy ($\Delta E^{+}_{ads} = \Delta E_{ads}$-$\Delta E_{des}$) and frequency factors as a function of nuclearity. Experiments were carried out in a quartz tubular fixed bed reactor coupled with a Mass Spectrometer to analyze the product gas by carrying out both, an integral analysis (from 0 to equilibrium conversion) by performing light-off experiments and differential analysis (low conversions) by performing Arrhenius experiments in the low and high coverage regions.

Structure sensitivity of H_2/D_2 Isotopic Exchange on Pt/Al_2O_3 catalysts

Ricardo Pool Mazun

(GENERAL AUDIENCE ABSTRACT)

Hydrogenation is a chemical reaction widely used in the petrochemical industry for the refining process where a substance reacts with molecular hydrogen H_2 adding pairs of H atoms to compounds. However, hydrogen is unreactive towards other substances in the absence of metal catalysts such as platinum (Pt), which dramatically accelerates the reaction rates making hydrogenation reaction possible. In industry, metallic catalysts are found as supported catalysts where the precious metal is supported on materials with higher thermal and mechanical stability to endure the operation conditions. Depending on the pretreatment conditions the size of metallic particles on the support can be manipulated, giving place to samples made of the same materials but different particle sizes with different properties. There are two critical steps during hydrogenation reactions the first one is the hydrogen activation which consists of the dissociation and adhesion of the two hydrogen atoms from the molecular hydrogen on the metallic surface and the second one is the reverse process where two hydrogen atoms recombine and are released from the metallic surface. Both steps involve a minimum amount of energy to dissociate and recombine hydrogen atoms which are strongly dependent on the metallic particle sizes. The goal of this thesis is to extract these dissociation and recombination energies of hydrogen on platinum particles of different sizes supported on alumina.

Dedication

For my beloved family, my friends, and my partner

Acknowledgments

To Dr.Ayman M. Karim who provided constant advice and feedback throughout the development of this project. He performed the data treatment for the EXAFS fittings.

To Dr. Dionisios G. Vlachos group (University of Delaware). For the collaborative work and feedback during the project "Molecularly Tailored Subnanometer Hydrogenation Catalysts".

To the Simon Bare Group (SLAC National Accelerator Laboratory) who helped to carry out the EXAFS experiments.

To my labmates, Dr. Coogan Thompson, Dr. Mi Yoo, Malik Albrahim, and Md. Raian Yousuf. Who helped me with their advice and instructions during my stay in Dr. Karim's lab group. Dr. Coogan Thompson, Malik Albrahim, and Md. Raian Yousuf also helped by carrying out the EXAFS experiments at SLAC National Accelerator Laboratory.

To the different institutions that provided financial support during the development of this project: Virginia Tech, The Department of Energy (DOE BES Award DE-SC0022144), and Fulbright-COMEXUS (scholarship "Fulbright-Garcia Robles").

Contents

List of Tables

Chapter 1

Literature Review

1.1 Structure Sensitivity: from Single Atoms to Nanoclusters and Nanoparticles

Hydrocarbon reactions on supported platinum catalysts as a function of particle size were extensively studied during the 1960s and 1970s. In those pioneering works, it was found that some reactions were strongly dependent on the particle size (alkane hydrogenolysis and isomerization) while other reactions were independent of the particle size. The expression structure sensitive reaction was first used by Michel Boudart who classified the first type of reaction using this term. Conversely, reactions that are not dependent on particle size were classified as structure insensitive. Previous studies were able to establish structure-reactivity correlations by using transmission electron microscopy and gas chemisorptions. Researchers found that changes in the catalyst particle size derive in different relative concentrations of terraces, steps, kinks, edges, and corner sites with variations of adsorbate binding energies due to changes in local atomic structure. Thus, it was reasonable to suggest that the modification of reaction rates was due to changes in the local atomic structure[1].

The resolution of the characterization techniques 60 years ago didn't allow us to see metal particles below 1nm. However, as the resolution of equipment's increased over the years, nowadays is possible to see single atoms and subnanometric clusters by using aberration-

corrected electron microscopy. These new technological advances allowed a more in-depth analysis of the catalytic properties of supported single atoms and subnanoclusters since now they can not only be imaged by STEM techniques but also studied by X-Ray absorption spectroscopy (XAS) under reaction conditions, which provides more information regarding the coordination environment of the metals present on the catalyst [2].

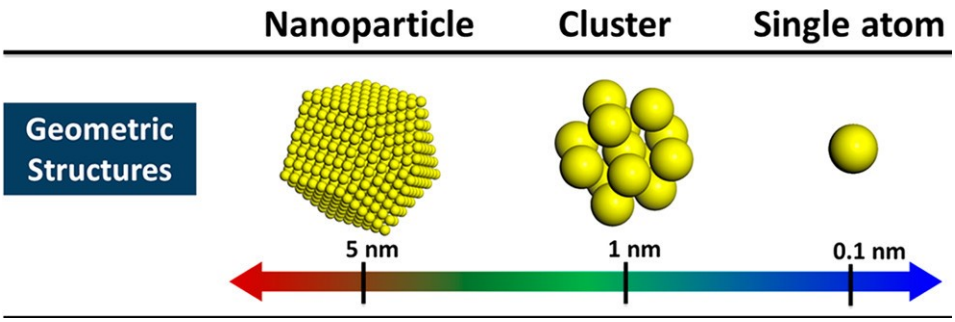

Figure 1.1: Geometric structures of a single atom, clusters, and nanoparticles.[2] Reprinted with permission from (Lichen Liu and Avelino Corma. Metal Catalysts for Heterogeneous Catalysis: From Single Atoms to Nanoclusters and Nanoparticles. 18(10):4981–5079). Copyright (2018) American Chemical Society.

On this ground, Single-atom catalysts (SACs) and nanoclusters have been calling the attention of researchers during the last years because of their excellent catalytic activity and selectivity in various chemical reactions, including CO oxidation, water-gas shift, oxidation of alcohols, hydroformylation, dehydrogenation and hydrogenation reactions. Furthermore, the study of supported metals at the atomic scale provides a new platform to study unique properties and structure-activity relations in catalysis.

Since to this day Pt-group metals are still extensively used in hydrogenation reactions, understanding the origin of the selectivity differences and structure-activity relations in the different size regimes, SA, nanoclusters, and NP is of great importance.

1.2 Hydrogenation Structure sensitivity

The design of supported metal catalysts with both high selectivity and high catalytic activity for selective hydrogenation reactions is still a crucial challenge that needs to be overcome in the heterogeneous catalysis field [3]. Gas-solid heterogeneous catalysis involves mainly three steps: adsorption of reactants, surface reaction, and desorption of products, and each step involves an inherent activation barrier so that the catalytic efficiency of a heterogeneous reaction involves the energetics of adsorbate adsorption, the transformation of intermediates into products, and desorption of the products[4]. During hydrogenation reactions, the adsorption and activation of H_2 are critical steps that are directly dependent on the geometric and electronic structure of the metallic active phase. Such changes can occur as a consequence of particle size. As we downsize the metallic particles to the nanoparticle, subnanometer, and single atoms regimes, electronic structure changes from continuous energy bands to discrete energy levels (quantum confinement effect).

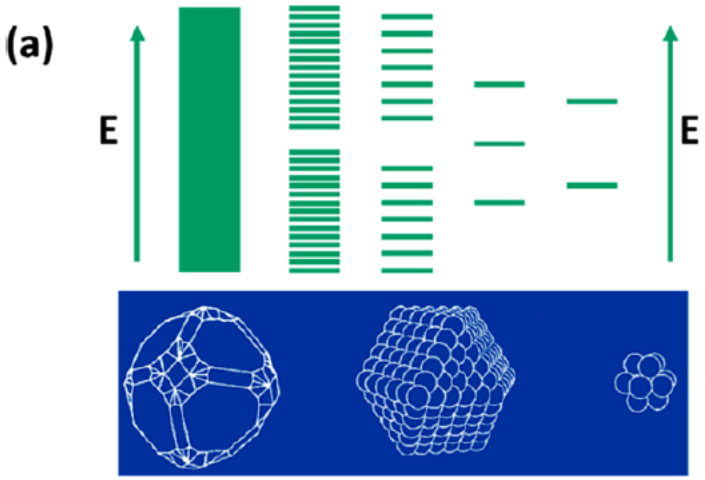

Figure 1.2: Quantum confinement effect.[3] Reprinted with permission from (Leilei Zhang, Maoxiang Zhou, Aiqin Wang, and Tao Zhang. Selective hydrogenation over supported metal catalysts: From nanoparticles to single atoms. 120(2):683–733). Copyright (2020) American Chemical Society.

As a consequence, different types of interactions with different energetics along the catalytic path can be taking place on catalysts with contrasting particle sizes, especially when comparing nanoparticles to nanoclusters and single atoms.

Oxide-supported Pt samples are widely used industrially for hydrogenation reactions. However, despite the scientific efforts from the catalysis community, the effect of Pt particle size on the kinetics of H_2 during hydrogenation reactions is still not well understood. Previous studies had shown that the nuclearity of supported Pt particles has an important effect on activity and selectivity when comparing Single Atoms (SA) to subnanometer to Nano-Particles (NP). Among some relevant studies, we have the structure sensitivity case for Pt/TiO_2 on the acetylene semi-hydrogenation carried out by Chun-Teh Kuo et al.[5]. In this study Pt/TiO_2 catalyst with different supported particle sizes ranging from SA (Pt_{SA}) to subnanometer clusters ($Pt_{SA-0.7nm}$ and $Pt_{0.9nm}$) to nanoparticles ($Pt_{1.5nm}$ and $Pt_{2.1nm}$) were evaluated showing that an increase in the particle size from SA to NP is accompanied by an increase of catalytic activity when using same amounts of Pt. However, a decrease in the particle size for Pt/TiO_2 to Single Atoms (SA) increases the selectivity of acetylene towards ethene production but lowers the activity (Fig 1.3).

To try to elucidate this unusual behavior H/D experiments were carried out. They found that the HD formation TOF (s^{-1}) increases as increasing the particle size from $Pt_{SA-0.7nm}$ to $Pt_{2.1nm}$ (Fig 1.3). These results were relevant since they provided evidence of the structure sensitivity for the H_2 activation being strongly related to the acetylene semi-hydrogenation activity. The structure sensitivity of Pt/Al_2O_3 on the propene hydrogenation has been studied by Zhivonitko et al. [6]. They found that an increase in the particle size shows a nonmonotonic character showing maximum conversion values of propene for Pt sizes between 2-4 nm. For this case of study, the authors attributed the differences in activity and selectivity toward pairwise H_2 in addition to the different relative concentrations of the sur-

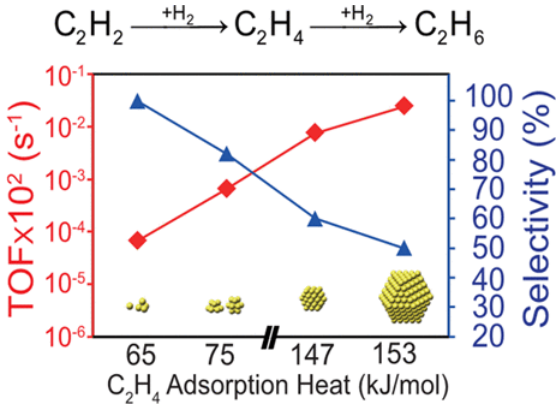

Figure 1.3: Structure Sensitivity of Acetylene Semi-Hydrogenation on Pt Single Atoms and Subnanometer Clusters.[5] Reprinted with permission from (Chun-Te Kuo, Yubing Lu, Libor Kovarik, Mark Engelhard, and Ayman M Karim. Structure sensitivity of acetylene semi-hydrogenation on pt single atoms and subnanometer clusters. 9(12):11030–11041. Copyright (2019) American Chemical Society.

face active sites as a function of particle size. Despite previous evidence shown regarding structure-sensitive hydrogenation reactions, to this day it is not clear whether the nature of these differences in activities has an energetic or entropic origin. Nevertheless, a wider understanding of the kinetic phenomena requires a deeper analysis of the samples' ability on the dissociative adsorb and associative desorp H_2, critical steps for any hydrogenation reaction.

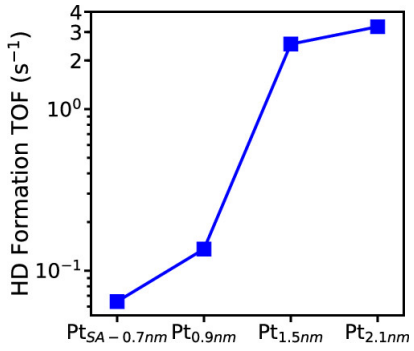

Figure 1.4: Particle size dependence of H_2-D_2 isotope exchange activity over Pt/TiO_2 catalysts.[5] Reprinted with permission from (Chun-Te Kuo, Yubing Lu, Libor Kovarik, Mark Engelhard, and Ayman M Karim. Structure sensitivity of acetylene semi-hydrogenation on pt single atoms and subnanometer clusters. 9(12):11030–11041. Copyright (2019) American Chemical Society.

1.2.1 Heats of adsorption for H_2 on supported Pt catalyst

Heats of adsorption of H_2 for Pt supported on different metal oxides (Al_2O_3, TiO_2, SiO_2, CeO_2) have been previously determined by different methods including temperature-programmed desorption and direct measurements of heats of adsorption using microcalorimetry studies. In this section, we will present a summary of different adsorption heat values for Pt-supported samples and single crystals/lattice planes. In his microcalorimetric studies, Vannice et al.[7] determined the H_2 heats of adsorption ($\Delta H_{H_2,ads}$) at 25 °C for Pt/Al_2O_3 Pt/TiO_2, and Pt/SiO_2 nanoparticles prepared by incipient wetness impregnation and reduced in a H_2 environment at 450 °C. For 2.1% w/w Pt/Al_2O_3 and Pt/SiO_2 catalysts (non-reducible supports) with crystallite sizes 1.5 and 6.7 nm respectively, Vannice and collaborators determined a $\Delta H_{H_2,ads}$ equal to 105 and 116 kJ/mol. On the other hand, for a 2%w/w Pt/TiO_2 samples (reducible support) he determined an $\Delta H_{H_2,ads}$ of 107 kJ/mol. These results are significant since they could indicate that in the nanometer regime the effect of different support whether reducible (TiO_2) or irreducible (Al_2O_3, SiO_2) does not have a strong influence on the heat of adsorption for H_2 over Pt nanoparticles. Among other relevant studies in the nanoparticle regime, Spiewak et al. also determined the differential heat of adsorption of H_2 (defined as the negative of the enthalpy change of adsorption per mole of gas adsorbed i.e. heat generated divided by the amount of gas adsorbed) on a 1.2wt% Pt/SiO_2 [8] and Pt powder [9] sample at 403 K. They found that as they increased the H_2 coverage the differential heat decreased from 90-100 kJ/mol to 50-60 kJ/mol for the 1.2wt% $Pt/Si0_2$ sample (Fig 1.5), showing a strong dependence with coverage. For Pt powder, they found an initial heat of 90 kJ/mol, in agreement with the heat for Pt/SiO_2. However, at higher hydrogen uptakes the differential heat decreases to values lower than 50 kJ/mol when the surface becomes saturated with H_2.

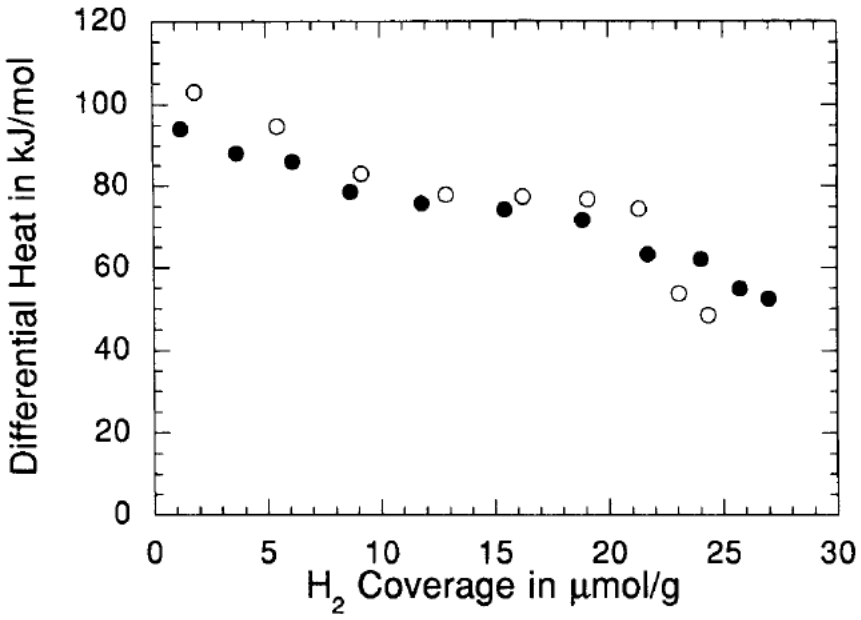

Figure 1.5: Differential heat of H_2 adsorption Vs H_2 coverage at 403 K on 1.2wt%Pt/SiO_2.[8] Reprinted with permission from (B.E. Spiewak and J.A. Dumesic. Microcalorimetric measurements of differential heats of adsorption on reactive catalyst surfaces. 290(1):43–53. Copyright (1997) Elsevier.

1.2.2 Pt lattice planes

Chemisorption and surface reactions strongly depend on both the electronics and the geometric structures of the surface. The correlation of chemisorption energies of different adsorbates (i.e. CO and H_2) on transition metal is strongly dependent on the local center of the metal d states, well known in the literature as the d-band center model of Hammer and Nørskov [10]. In this theory, the description of the quantum mechanics of atoms and molecules with a metal surface is modeled as a one-electron state outside of a metal surface interacting with all valence states of the surface atoms. When a band is broad and low only a single resonance can be seen. However, as the energy of the center of the band e_d increases, antibonding states start to appear above the Fermi level. Since these antibonding states are empty the bond energy between adsorbate and metallic surface increases. This behavior illustrates a general rule about chemisorption energies at a metallic surface: Strong chemisorption occurs when

empty antibonding states appear up through the Fermi level which is illustrated in Fig 1.6.

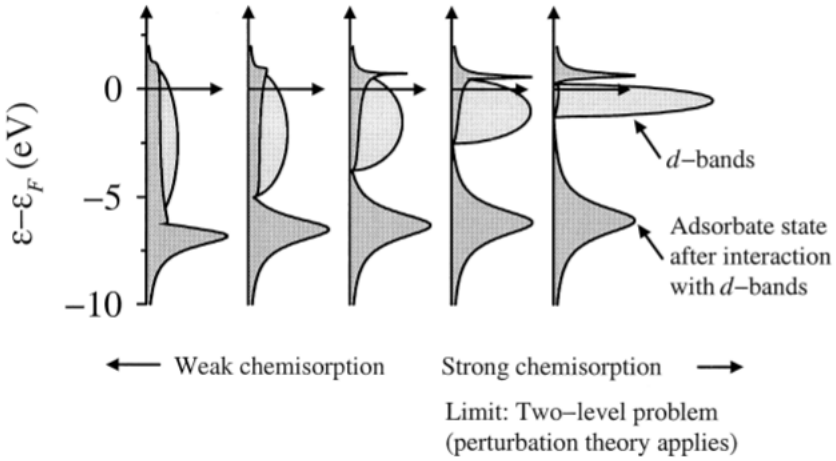

Figure 1.6: Local density of states projected onto an adsorbate state interacting with the d bands at the surface.[10] Reprinted with permission from B. Hammer and J.K. Nørskov. Theoretical surface science and catalysis calculations and concepts. In Advances in Catalysis, volume 45, pages 71–129. Academic Press. Copyright (2000) Elsevier.

Another model that describes both physisorption and chemisorption is the Lenard-Jones model for adsorption. In this model shown in Figure 1.7, the chemisorption state is reached from a physisorption state when while approaching the metallic surface, physisorbed adsorbate molecules overcome an adsorption activation barrier, ΔE_{ads}. On the other hand, a physisorption state is reached when chemisorbed atoms from the metallic surface overcome a desorption activation barrier, ΔE_{des} [11]. So that the total coverage of the system can be described as the difference in adsorption and desorption rates by the following equation:

$$\frac{\theta}{\mathrm{d}t} = k'_{ads} exp\left(\frac{\Delta E_{ads}}{kT}\right) - \theta k'_{des} exp\left(\frac{\Delta E_{des}}{kT}\right) \tag{1.1}$$

Thus, under steady state conditions and given that $\Delta H_{ads} = \Delta E_{ads} - \Delta E_{des}$ Coverage is equal to:

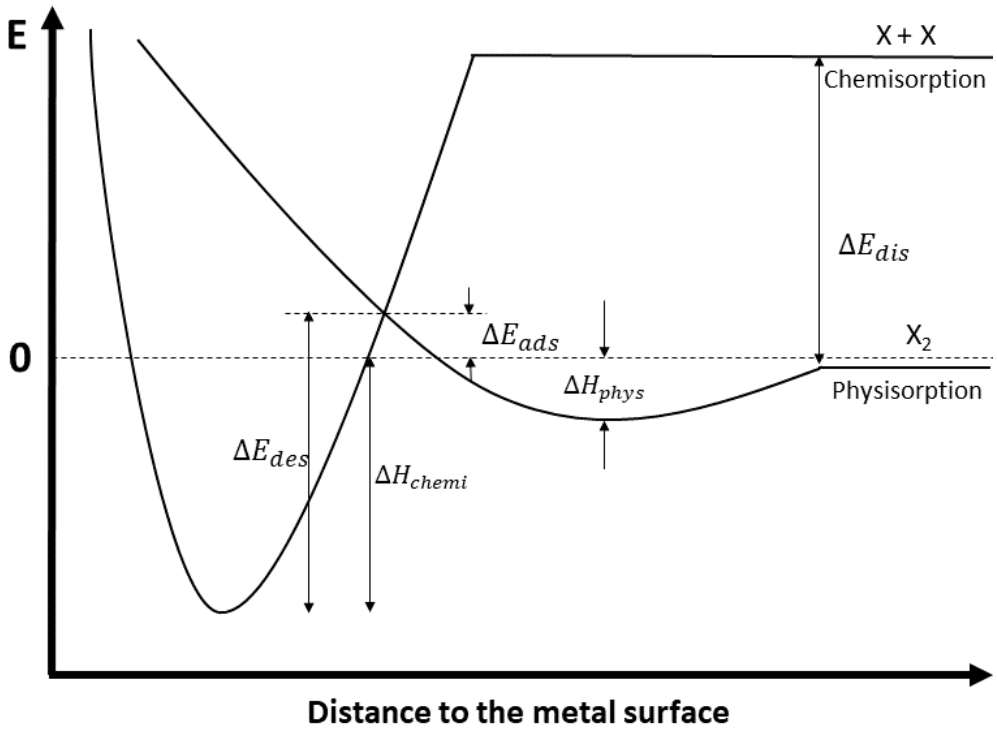

Figure 1.7: Lenard Jones Diagram. Physisorption and Chemisorption of X_2 and 2X on metallic surface

$$\theta = \frac{k'_{ads}}{k'_{des}} exp\left(\frac{\Delta H_{ads}}{kT}\right) \tag{1.2}$$

Depending on the arrangement of the atoms, metal single crystals can present different lattice facets, usually identified by the Miller index as a triplet of integer values (hkl) as well as steps and defects like steps and kinks. Different surface facets have different electronic structures. Thus, some of these lattice planes and defect sites can be more active than others, changing the heat of adsorption of the adsorbates on the catalytic surface. In their studies, Chang Lu et al. [12] correlated the heat of adsorption of CO and H_2 to the positions of the energy center of the d-band for several Pt lattices comparing both Density Functional Theory (DFT) simulations and results from temperature programmed desorption experiments. Their experimental results indicate that hydrogen binds more strongly to Pt(111) than to

surfaces Pt(110), comparable to (111) steps and (111) terraces with values ranging from 100 to 75 kJ/mol. These results are relevant since they might indicate that H_2 is more stable on Pt center atoms from the Pt(111) facet than on step or kinks sites. These experimental results are summarized in Fig 1.8, where it should be noticed that experimentally, $\Delta H_{H_2,ads}$ decreases as the energy of the d-band increases. Conversely, DFT simulations show the opposite behavior, following the d-band theory trends. This discrepancy between experimental and theoretical values is of great importance since it indicates that the interaction between H_2 and different Pt facets might be affected by different external factors other than the interaction of the d bands at the surface with the adsorbate. Other experimental values of heats of chemisorption of H_2 on single crystal surfaces determined by calorimetry and thermal desorption had been reported by I. Toyoshima G. A. Somorjai [13]. For Pt(100) the $\Delta H_{H_2,ads}$ determined by thermal desorption was 66 kJ/mol. On the other hand heats of adsorption of H_2 for Pt(111) ranged from 75 to 130 kJ/mol determined by thermal desorption at room temperature and 40 kJ/mol at 150 K.

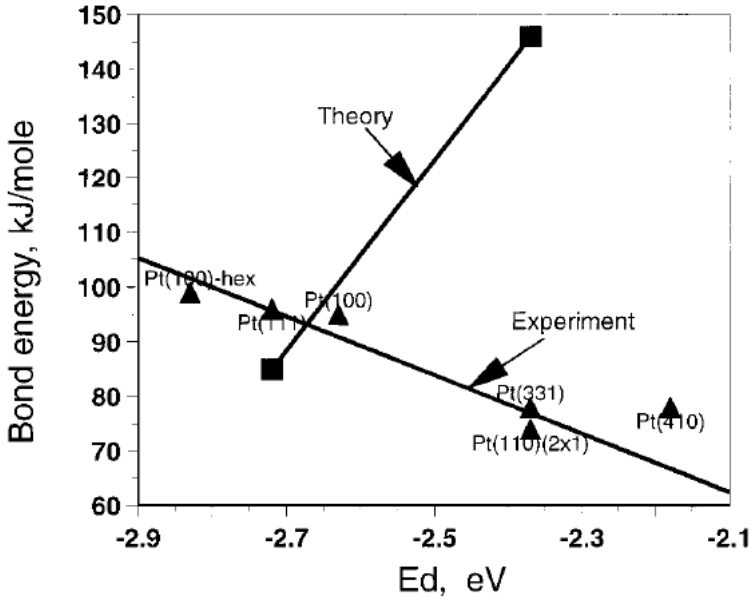

Figure 1.8: Hydrogen heat of adsorption against the energy of the center of the d-band of the surface atoms on different Pt lattice planes [10] Reprinted with permission from Chang Lu, Ivan C Lee, Richard I Masel, Andrzej Wieckowski, and Cynthia Rice. Correlations between the heat of adsorption and the position of the center of the d-band: Differences between computation and experiment. 106(13):3084–3091. Copyright (2002) American Chemical Society.

1.2.3 H_2 heats of adsorption on supported Pt nanoparticles and lattice plane summary

In this section, we present a summary of $\Delta H_{H_2,ads}$ values for both supported Pt particles and different lattice planes discussed in the previous 2 subsections.

Table 1.1: Hydrogen heats of adsorption for supported Pt catalysts and different lattice planes

Catalyst	**$\Delta H_{H_2,ads}$ [kJ/mol]**	**crystallite size [nm]**	**Technique**	**Ref.**
2.1wt%Pt/Al_2O_3	105	1.5	Calorimetry	[7]
2.1wt%Pt/SiO_2	116	6.7	Calorimetry	[7]
1.2wt% Pt/$Si0_2$	90-100[a]	-	Calorimetry	[9]
1.5wt% Pt/SiO_2-Al_2O_3	115-122	2.9	Calorimetry	[7]
2wt% Pt/TiO_2	107	1.1	Calorimetry	[7]
Pt powder	90[a]	-	Calorimetry	[9]
Pt(111)	98	-	TPD	[10]
Pt(110)	75	-	TPD	[10]
Pt(100)	66	-	TPD	[13]

a: Initial heat of adsorption

Retaking the major points previously discussed we should notice that for Pt particles on both irreducible (Al_2O_3 and SiO_2) and reducible supports(TiO_2) in the nanoparticle regime we have similar $\Delta H_{H_2,ads}$ ranging from 106 to 116 kJ/mol. Something important to notice is how remarked size increases in the nanoparticle regime do not show a big effect on the heat of adsorption. i.e. 2.1wt%Pt/SiO_2 with 6.7 size and 2.1wt%Pt/Al_2O_3 with 1.5 nm crystallite size shows just a difference of just 10 kJ/mol. On the other hand regarding the differences on Pt facets, experimental values indicate that H_2 is more stable on Pt(111) than on Pt(110) and Pt(100). This is important since it could indicate that H_2 is more stable on Pt central atoms than on kinks, defects, or step sites. Furthermore, for different Pt facets, experimental $\Delta H_{H_2,ads}$ seems to decrease as the energy of the d-band increases, contrary to the d-band center theory trends.

1.3 H_2-D_2 isotopic exchange

The Bonhoeffer-Farkas mechanism [14] is a simple but powerful kinetic model for HD exchange (H_2 + D_2 -> 2HD) that can help us to extract the intrinsic energetic barriers and frequency factors for dissociative adsorption and associative desorption (ΔE_{ads}, ΔE_{des} and v_{ads}, v_{des} respectively) for the different catalysts evaluated in this study. A complete description of the model and assumptions are described in Appendix C.1.

Table 1.2: Bonhoeffer and Farkas mechanism

Reaction Number	Elementary step	σ
1	$H_2 + 2* \rightleftharpoons 2H*$	1
2	$D_2 + 2* \rightleftharpoons 2D*$	1
3	$H^* + D^* \rightleftharpoons 2HD + 2*$	2
Overall rxn	$H_2 + D_2 \rightleftharpoons 2HD$	

$\sigma : Horiuti's number$

The importance of this model relies on the quantitative determination of the adsorption and desorption kinetic parameters which allowed us to perform a more in-depth analysis regarding whether the differences in the activity as a function of particle size have an energetic or entropic origin. This H_2-D_2 isotopic exchange model has been previously studied over Pd, Cu, and Pd-Cu foil surfaces by O'Brien et al.[15]. In their studies, they tested the reduced diced foil catalyst in a fixed bed reactor coupled with a mass spectrometer to record the composition of the reactor effluent by performing integral reactor experiments (catalytic evaluation over a wide T range from 0 to equilibrium conversion of H_2/D_2). Among some important conclusions, they attribute the differences in activity mainly to the different energies of adsorption of H_2 ($\Delta E^{+}_{ads} = \Delta E_{ads}$-$\Delta E_{des}$) for their different samples. On the other hand, Van der Hoeven et al. [16] carry out Arrhenius experiments (activity measurement over narrow T ranges and conversions below 20%) for the H/D exchange reaction and found that on dilute Pd-in-Au alloy nanoparticle catalysts an increase in Pd ensemble size results in

an enhanced rate due to entropic effects, with a pronounced increase of the pre-exponential factors. Although there are studies regarding H/D exchange on mono-disperse Pt clusters and single crystals[17], a numerical determination of the kinetic parameters derived from the microkinetic model analysis for supported Pt/Al_2O_3 on a nanoparticle, sub-nanoparticle, and SA scale has not yet been reported in the literature. Therefore, this case of study aims to contribute to the elucidation of the kinetic phenomena by determining the numerical values of the kinetic parameters of interest.

1.3.1 Alternative H/D isotopic exchange mechanism over supported Pt nanoparticles

Leung et. al. [18] had reported that for Pt/Al_2O_3 and Pt/SiO_2 samples with d_p of 1.9 and 3.2 nm respectively, dissociative—recombinative (1-3) and non-competitive adsorption (4-5) elementary steps happen during the H/D exchange reaction (Table 1.3). Equations 1.3 and 1.4 represent the reaction rates as a function of P_{H_2} and P_{D_2} derived from the Recombination mechanism (steps 1-3) and the recombination mechanism + non-competitive adsorption (steps 1-3 and 4-5). Among the most important features of this case of study are that if the H/D exchange reactions rate follows the recombination mechanism (equation 1.1) experimental data of $r_{HD,f}$ Vs P_{H_2} should show a maximum along the P_{H_2} range. Conversely, if the non-competitive adsorption elementary steps are predominant $r_{HD,f}$ should continue increasing as P_{H_2} increases (last term in equation 1.2).

$$r_{HD,f} = k_{des}\frac{P_{H_2}P_{D_2}}{(P_{H_2}+P_{D_2})^2} \tag{1.3}$$

$$r_{HD,f} = k_{des}\frac{P_{H_2}P_{D_2}}{(P_{H_2}+P_{D_2})^2} + 2k_4\frac{P_{H_2}P_{D_2}}{(P_{H_2}+P_{D_2})} \tag{1.4}$$

Experimentally the authors found that for their Pt/Al_2O_3 sample $r_{HD,f}$ Vs P_{H_2} plots at fixed P_{D_2} and 383 K showed a continuous increase of $r_{HD,f}$ as they increase P_{H_2}. This linear trend is attributed to the predominant non-competitive adsorption elementary steps toward HD generation as explained before.

The relevance of this study is that it provides deep insights regarding the reaction mechanism predominant during the H/D isotopic exchange. In specific, the $r_{HD,f}$ Vs P_{H_2} plots turn out to be a simple and practical experiment that will help us to provide an explanation of which mechanism is predominant for our samples in further chapters.

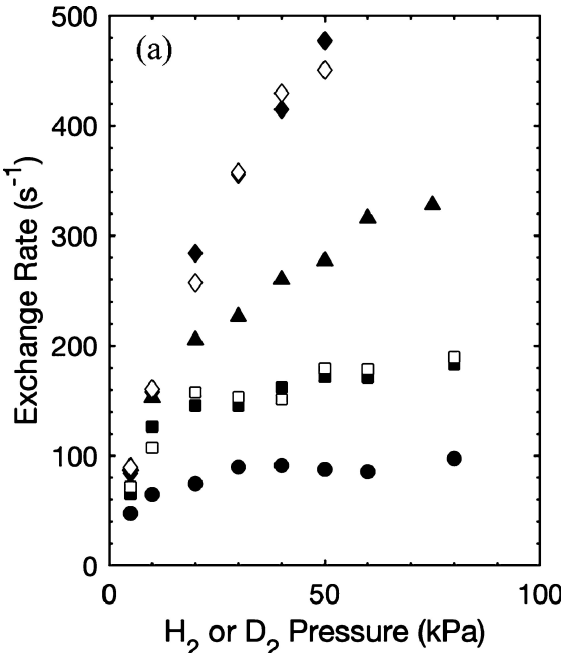

Figure 1.9: H_2−D_2 exchange rates as a function H_2 or D_2 pressure on (a) 1% wt. Pt/γ-Pt/Al_2O_3 (d_p=1.9nm) at 5 (●, ○), 10 (■, □), 20 (△, ▲), and 40 (◇) kPa H2 (open symbol) or D2 (closed symbol) at 383 K.[18] Reprinted with permission from Samuel L. Leung, David Hibbitts, Mónica Gárcia-Diéguez, et al. The Journal of Physical Chemistry C 126(8):3923–3938. Copyright (2022) American Chemical Society.

Table 1.3: Alternative reactions mechanisms for H/D exchange

Reaction Number	Elementary step	σ
1	$H_2 + 2* \rightleftharpoons 2H*$	1
2	$D_2 + 2* \rightleftharpoons 2D*$	1
3	$H^* + D^* \rightleftharpoons 2HD + 2*$	2
4	$H_2 + D* \rightarrow 2HD + 2*$	2
5	$D_2 + H* \rightarrow 2HD + 2*$	2
Overall rxn	$H_2 + D_2 \rightleftharpoons 2HD$	

$\sigma : Horiuti's number$

1.4 H_2 high-temperature phenomena on supported Pt catalysts

Some difficulties could arise regarding the evaluation of activity for Pt-supported catalysts since they may undergo high-temperature phenomena under the reaction conditions when evaluating wide temperature ranges, affecting the measured catalytic activity. In their work, Lisitsyn et al. [19] reported that pronounced desorption of H_2 on reduced Pt/Al_2O_3 happens along the T range 100-500 °C when performing H_2-TPD which can directly impact the determination of the catalytic activity between these T ranges. In addition, they showed that small H_2O concentrations can substantially increase the amount of H_2 desorption and shift the desorption peaks towards lower temperatures. Furthermore, they hypothesize about additional H_2O and H_2 effects at moderate temperatures on the Pt/Al_2O_3, where both species can induce the generation of anionic oxygen vacancies in the support and consequently cause reversible 2D-3D transitions for the shape of the Pt clusters. Is important to notice that this type of transition has not been experimentally proven, however, is well-predicted by DFT calculations since the transition from 2D to 3D particle distribution can maximize the adsorption capacity towards hydrogen by weakening the metal-support interaction (Fig 1.10).

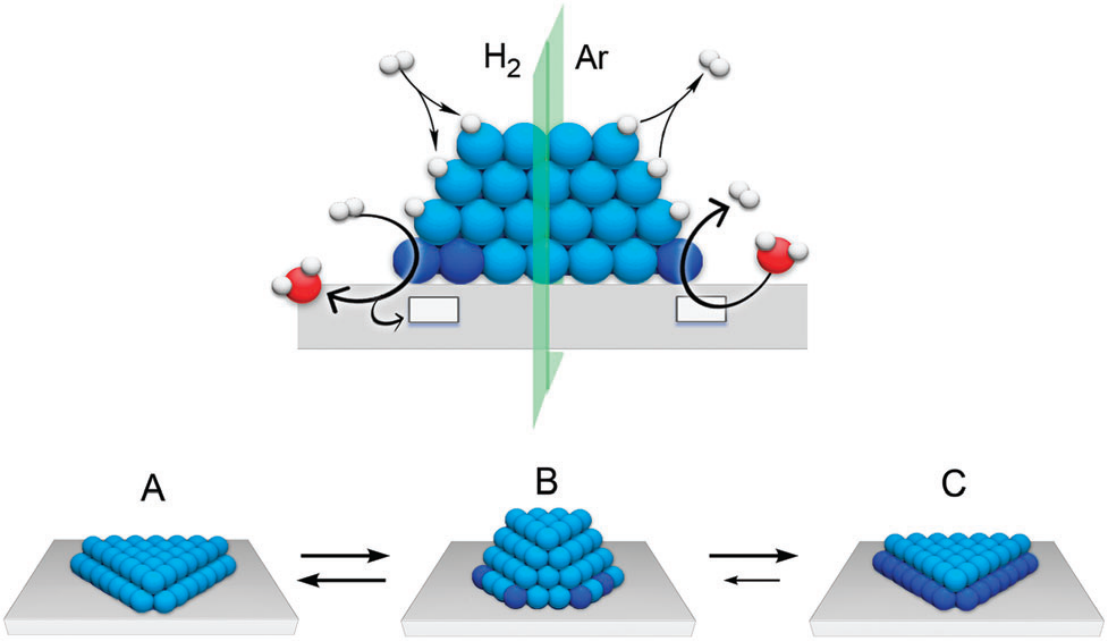

Figure 1.10: Schematic of the 2D-3D Pt particle transition during high-temperature H_2-treatments. H atoms are denoted by white circles, O atoms by red circles, Pt atoms by blue circles, and oxygen vacancies in Al_2O_3 by rectangles. [19] Reprinted with permission from Alexander S. Lisitsyn and Olga A. Yakovina. On the origin of high-temperature phenomena in Pt/Al_2O_3. 20(4):2339–2350. Copyright (2018) The Royal Society of Chemistry.

Regarding mobility of Pt particles (SA and NP) on the support, Steven A Bradly et al. [20] performed an analysis by using aberration-corrected STEM imaging while reducing the Pt catalyst on different oxide supports. They showed that the mobility of Pt atoms is different depending upon the catalyst support. The mobility according to their results increase as follows: $TiO_2 < Al_2O_3 < SiO_2$. This is in line with the decreasing strong metal support interactions (SMSI) of Pt on the respective oxide support. As a consequence of this mobility, supported SA on calcined samples tends to agglomerate under H_2 environments as we increase the reduction temperature. For example, 0.35 wt% Pt/Al_2O_3 samples just showed individual Pt atoms and a few dimers and trimers dispersed on the support after oxidation at 500°C. However, after reduction at 500 °C under H_2 atmosphere and air-exposed during transfer into the microscope, 0.6-1 nm Pt subnanoclusters were observed. In contrast, cluster sizes

between 0.6 to 2 nm were already on the oxidized at 500 °C 0.35 wt% Pt/SiO_2, even before reduction. Something interesting to note about the 0.35 wt% Pt/Al_2O_3 sample in this study is that the Pt clusters formed after reduction with H_2 present a raft-like morphology (flat distribution). Further studies regarding Pt/Al_2O_3 SACs stability were provided by Dessal. et al. [21]. In their studies, they confirmed that Pt SA under a H_2 environment tends to sinter from SA to subnanoclusters for the Pt/Al_2O_3 system by using STEM-ADF images. Their own DFT simulations regarding H_2-induced clustering and mobility effects predict aggregation from Pt_1 to Pt_{13}. Something important to notice is that according to the most stable systems found in their DFT calculations, the Pt_{13} clusters are expected to be of biplanar morphology (flat clusters) in the absence of H_2, interacting with Pt-Al and Pt-O bonds with the support. On the other hand, under a H_2 atmosphere at high pressures and at low temperatures, the nanoparticles tend to reconstruct in a cuboctahedron and disconnect from the support. These DFT calculations are of great importance since they provide more evidence regarding possible 2D-3D particle morphology transitions under high H_2 partial pressures. Furthermore, the presence of particle mobility on the support under H_2 environment can derive in difficulties when determining the catalytic activity of Pt SA on the H/D exchange reaction. In addition to the previous high-temperature effects, Spill-over effects might be taking place on Pt/Al_2O_3 and Pt/TiO_2 samples. Evidence of this was provided by Clelia Spreafico et al. [22] in their Kinetic Monte Carlo simulations. Their studies predict that hydrogen atoms can spread homogeneously on the TiO_2 surface, while on Al_2O_3 hydrogen can only be found a few nm away from the Pt clusters because of a kinetic competition between diffusion and desorption of H atoms on the surface.

1.5 Problem Statement

In the previous sections, we provide evidence from different cases of study for supported Pt catalysts where a decrease in particle size from nanoparticles to subnanoclusters to SA causes a decrease in activity [5] [6] during hydrogenation reactions and H_2 activation. Given the previous evidence, it is clear that during hydrogenation reactions the size of the supported particles plays an important role in the kinetics of the reaction, especially during the activation of H_2, a critical step during any hydrogenation reaction. However, to this day it is not clear whether the differences in activity have an energetic or entropic origin when considering Arrhenius-like models.

The important questions that we are trying to address in this case of study are the following:

- the activity differences during H_2 activation and hydrogenation reactions on supported Pt samples with different nuclearity are due to different adsorption and desorption energy barriers along the catalytic path?

- and/or the activity differences are due to different adsorption and desorption pre-exponential factors during the H_2 activation steps?

- What is the dependence of particle size on the binding energy of H_2 on the metallic surfaces?

By numerically determining both the energetic barriers and pre-exponential factors for dissociative adsorption and associative desorption we would be able to provide a more in-depth analysis regarding the difference in activity as a function of nuclearity from a quantitative perspective.

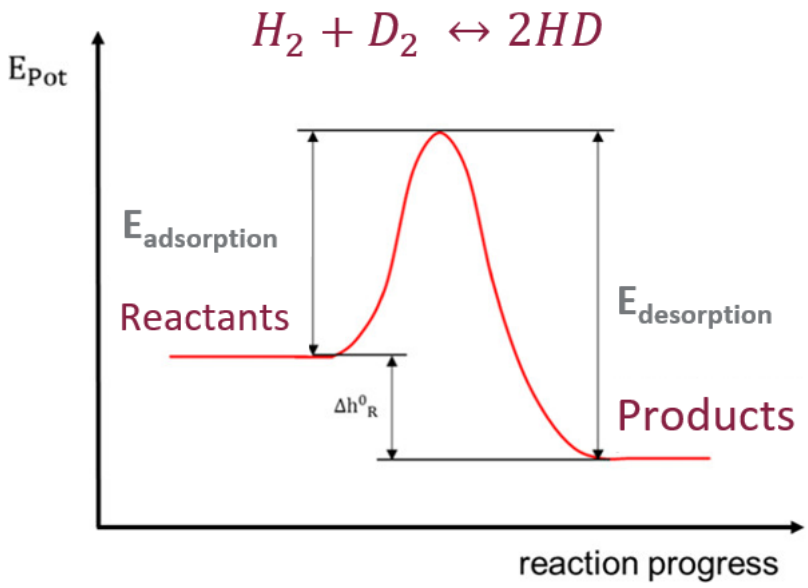

Figure 1.11: Energetic barriers Vs Reaction Coordinate

1.5.1 Approach

The H_2-D_2 isotopic exchange experiments follow a simple but powerful microkinetic model that helped us to extract the energetic and pre-exponential factors for dissociative adsorption and associative desorption during H_2 activation. Nevertheless, the catalytic evaluation of supported Pt catalyst can get complicated since it involves high-temperature phenomena that can occur while evaluating the catalytic activity. Such phenomena include modifications in adsorption, desorption, mobility of metallic particles on the support, and spillover of H_2/D_2 over the metallic particles and the support. To overcome these limitations in this work we decided to perform both integral and differential experiments testing the catalyst at atmospheric pressure in a PBR using the HD isotopic exchange reaction. Light-off experiments allowed us to determine the activity over a wide temperature range from 0 to equilibrium conversion. In contrast, Arrhenius's experiments allowed us to determine the catalytic activity in the low and high coverage regime while keeping low conversions.

Chapter 2

Methodology

2.1 Pt/Al_2O_3 Preparation

Pt/Al_2O_3 samples with weight loading 0.01, 0.05, and 5% were prepared using a wet impregnation method described by Ebbesen et al. [23]. Commercial γ-Al_2O_3 (Sasol, Puralox TH 100/150) and Chloroplatinic acid solution H_2PtCl_6 8% wt in H_2O (Sigma-Aldrich) was used as precursor. Prior to synthesis, the Al_2O_3 support was calcined in air in the muffle furnace at 550 °C for 5h using a Temperature ramp of 5°C/min. The precursor-support solution was mixed for 2h and then left to dry out overnight at 60 °C on the heating plate. The resulting powder was calcined in the muffle furnace. A synthesis example is provided in Appendix A.1

2.2 Catalyst Characterization

2.2.1 Aberration-Corrected Scanning Transmission Electron Microscopy (AC-STEM)

AC-STEM images were taken on an FEI TITAN 80-200 in STEM mode using a high-angle annular dark-field (HAADF) detector. Analysis was performed ex-situ for the Pt/Al_2O_3

samples after reduction in 20 %v/v H_2 (balance with Ar at atmospheric pressure) for 2h at the respective reduction temperature for each sample. The resolution was 0.1 nm with the CEOS GmbH double-hexapole aberration corrector. The surface average particle diameters were determined using [24]:

$$d_{SA} = \frac{\sum n_i d_i^2}{\sum n_i d_i^3} \tag{2.1}$$

To ensure particle diameters are statistically representative we analyze a population of more than 400 NP from different AC-STEM images. Particle size distribution is represented as Pt Atomic percentage in Appendix A.2 where the total number of atoms per particle was estimated with the equation:

$$N_T = \frac{\pi D^3 \rho N_A}{6 M_w} \tag{2.2}$$

where D is the mean nanoparticle diameter for each particle size range measured by STEM, is the bulk density of Pt (21.45 g/cm3), N_A is Avogadro's number (6.02 x 1023 mol^{-1}), and M_w is the molecular weight for Pt (195.08 g/mol).

2.2.2 CO and H_2 volumetric chemisorption

Volumetric chemisorption of both H2 and CO was performed on both 0.05 and 5% Pt/Al_2O_3 samples. Experiments were performed in a 3-Flex Micromeritics equipment. Pretreatment of samples was performed in-situ in static mode in a step-wise manner. First, the quartz sample holder packed with the pelletized sample (400-700 microns) and a filler rood was evacuated below 1 x 10^{-3} mmHg. Then, we started a heating ramp rate of 10°C/min from room temperature to the corresponding reduction temperature for each sample. The reduction

step started by adding H_2 at 760 mmHg at the corresponding reduction temperature for 1h. The sample was then evacuated at the same reduction temperature and refilled with H_2 at 760 mmHg for 1h more (2h reduction in total). After pretreatment, the sample was evacuated and cooled down at 35 °C while still under vacuum before H_2 volumetric chemisorption. Chemisorption isotherms were obtained at 35 °C with an evacuation step between them to remove the physisorbed H_2. CO chemisorption was performed after H_2 chemisorption with an evacuation step at the reduction temperature of the sample between experiments to remove any H_2 that could be still adsorbed. A summary of the dispersion values from chemisorption experiments as well as the particle diameters determined from STEM images and notation of the samples from now on is provided in Table 3.1.

2.2.3 Diffuse Reflectance Infrared Fourier Transform Spectroscopy (DRIFTS)

Experiments using CO as a probe molecule for 0.05 and 5% Pt/Al_2O_3 samples were performed in a Thermo Scientific Nicolet iS50 FTIR Spectrometer equipped with a praying mantis and a mercury cadmium telluride (MCT) detector. Spectrum series were collected using an average of 32 scans for each spectrum with a data spacing of 0.482 cm^{-1} in K-M units. Samples were activated in-situ in a 20%v/v H_2 environment at atmospheric pressure (balanced with N2, 100 sccm total flow). Spectras can be found in Appendix 1,3. Background spectra were collected after reduction at 35 °C using 100 sccm of N_2. Following, 20 sccm of a 1% CO gas flowed through the activated sample for 20 min. Finally, the system was purged with 100 sccm of N_2 to remove the gas-phase CO on the Pt/Al_2O_3 samples while a series of spectra were collected. H_2 and N_2 lines were purified by high-capacity moisture traps (Restek 20600). CO gas line was equipped with a metal carbonyl purifier (Matheson, NanoChem Metal-X). Flow rates were regulated by mass flow controllers (5850EM, Brooks Instrument).

2.2.4 X-ray absorption spectroscopy

X-ray absorption spectroscopy (XAS) was performed at Pt L_3-edge (11564 eV) for the Pt/Al_2O_3 samples to probe the local environment of the Pt species and their oxidation state. solid samples between 100-180 microns were loaded in quartz tube reactors. The XAS experiments were carried out at the Stanford Synchrotron Radiation Light Source (SSRL) at beamline 9-3 in fluorescence mode. Beamline 9-3 is a 16-pole, 2-Tesla wiggler side station with a vertically collimating mirror for harmonic rejection and a cylindrically bend mirror.

Table 2.1: Beamline 9-3 at SSRL details

Beamline	SSRL BL 9-3 2-Tesla wiggler
Flux at 23220 eV (photon/s)	3.22 x 10^{11}
Beam size (mm x mm)	1 x 3
Flux density (photon/s/mm^2)	1.1 x 10^{11}

Pt foil was used as a standard scanned at the same time with each different sample for energy calibration. Step-scanning X-ray absorption spectra were collected using k-range 3-14.75 Data processing and analysis for the X-ray absorption near edge structure (XANES) and the EXAFS were performed using the Athena and Artemis programs of the Demeter data analysis package. After the normalization of the absorption coefficient, The smooth atomic background was subtracted using the AUTOBKG code in Athena to obtain χ (k) (where k is the photoelectron wavenumber). The theoretical EXAFS signal for the Pt−O and Pt-Pt scattering paths was constructed using the FEFF627 code using the crystal structure of Pt metal. The theoretical EXAFS signals were fitted to the data in r-space using Artemis by varying the coordination numbers of the single scattering paths, the effective scattering lengths, the bond-length disorder, and the correction to the threshold energy, ΔE_0, for the Pt-Pt path. S_0^2 (the passive electron reduction factor) was obtained by first analyzing the

first shell of the Pt foil spectrum, and the best-fit value (x ± y for data collected at SSRL BL 9-3) was fixed for the fit. The k range used for the Fourier transform of (k) was 3−14.75 $Å^{-1}$ for the reduced catalyst, and the r range for fitting was 1.2−3.1 Å

2.3 H_2-D_2 Isotopic exchange

2.3.1 Experimental Setup

Reduction in-situ and H/D isotopic exchange were performed in a 4 mm I.D quartz tubular fixed bed reactor coupled with an online Mass Spectrometer (Pfeiffer Thermostar GSD 350) to determine H_2, HD, and D_2 compositions based on the ion current signals intensity for m/q=2,3,4 respectively. A thermocouple was attached to the outer wall of the tubular reactor touching the mid-height of the catalyst bed to record the temperature. The reactor was heated using a temperature-programmed furnace (Mellen SC12.5R). Mass flow controllers (Brooks Instrument, 5850EM) were used to regulate the flow rates of H2(UHP 99.999%), D2(certified UHP 99.9999%), and Ar (UHP 99.999%) from Airgas Inc. H_2 and D_2 were purified by high-capacity moisture traps (Restek 20600). Figure 2.1 shows a schematic of the described setup.

2.3.2 Catalyst reduction with H_2

Reductions of Pt/Al_2O_3 samples were performed in-situ prior to H/D experiments. Catalysts were diluted with SiO_2 after calcination at 850 °C for 8 h. The diluted samples were grounded using an agate mortar and pestle, pelletized, and sieved into 106-180 μm pellets. samples were then placed inside a 4 mm I.D quartz tubular reactor, dried at 120°C (ramp rate 5°C/min) for 2h in Ar flow (40 sccm) and reduced in situ for 2h in H_2 20%v/v environ-

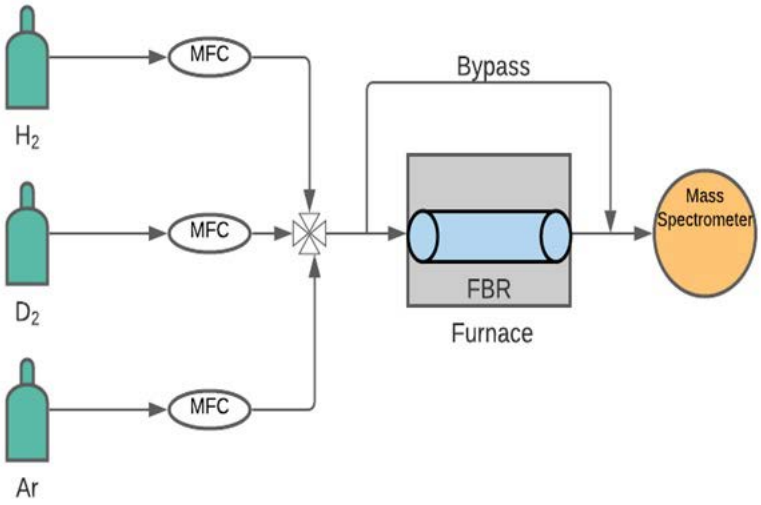

Figure 2.1: Experimental set up for H/D exchange experiments. MFC: Mass Flow controller. FBR: Fixed Bed Reactor.

ment balance with Ar at atmospheric pressure (50 sccm total) at the respective reduction temperature for each sample, T_{red} using a ramp rate of 5°C/min (Fig 2.2).

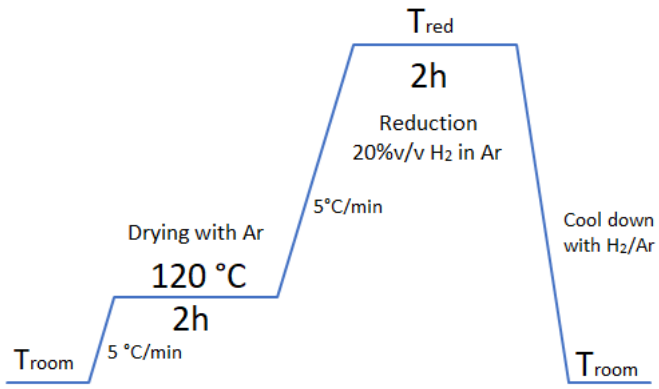

Figure 2.2: Temperature profile for reduction of Pt/Al_2O_3 samples.

2.3.3 Conversion, reaction rate and TOF

The reactive mixture consists of an equimolar mixture of H_2 and D_2 in balance with Ar. The flow rate used was 5-5-10 sccm (H_2-D_2-Ar).

$$H_2 + D_2 \rightleftharpoons 2HD \tag{2.3}$$

Since we have an equimolar mixture of H_2/D_2 and following the 1:2 stoichiometric relation between H_2 and HD

$$Conversion : X = \frac{F_{H_2,feed} - F_{H_2,outlet}}{F_{H_2,feed}} = \frac{F_{HD}}{2F_{H_2,feed}} \tag{2.4}$$

where $F_{H_2,feed}$ and $F_{H_2,outlet}$ are the molar flow rates [mol/s] of H_2 at the inlet and outlet of the reactor respectively and F_{HD} the molar flow rate of HD generated.

The experimental reaction rate were determined based on the following equation:

$$Reactionrate : r_{HD} = \frac{F_{HD}}{g_{Pt} * Dispersion} \tag{2.5}$$

The Turnover frequency (TOF) can be determined as follows:

$$TurnOverFrequency : TOF = \frac{F_{HD}}{g_{Pt} * \frac{molPt}{g_{cat}} * Dispersion} \tag{2.6}$$

where both the $\frac{molPt}{g_{cat}}$ and Dispersion values can be obtained from the CO chemisorption experiments

2.3.4 H/D exchange integral reactor experiments

For the integral reactor experiments a mass of 250 mg of diluted catalyst corresponding to a bed length ≈ 5.5 cm was placed inside the reactor in order to avoid external mass diffusion limitations (Appendix B.1 and B.2). The amount of diluted sample corresponds to a Pt content of 6−9 E-07 g depending on the dilution ratio used. Feed gas condition was 5,5 and 10 sccm of H_2, D_2, and Ar respectively at atmospheric pressure. The temperature was increased from room temperature to the reduction temperature of the sample using a heating ramp rate of 1°C/min. The composition of the reactor effluent was determined using an online Mass Spectrometer (Pfeiffer Thermostar GSD 350) assuming that the Ion Current signals at m/q=2,3,4 amu from the product gas were proportional to the H_2, HD, and D_2 partial pressures between the baseline signals and conversion values of H_2 and D_2 at equilibrium described by McQuarrie (Equation 2.7) [25]:

$$K(T) = 4.24exp\left(\frac{-77.7}{T}\right) \tag{2.7}$$

The objective of this type of experiment was to extract the energetic barriers and pre-exponential factors for dissociative adsorption and associative desorption (ΔE_{ads}, ΔE_{des} and v_{ads}, v_{des} respectively) by minimizing the error function between experimental and theoretical $F_{HD,out}$=f(T) from equation C.12 (See Appendix C.1 and C.2 for the derivation of the integral model from the reaction mechanism). Minimization of error function was performed in Matlab by applying the integrated numerical solver Fminsearch to the mean squared error equation (Equation 2.8).

$$Error = \frac{1}{N}\sum_{i=1}^{N}\left(F_{HD,out,i}^{exp} - F_{HD,out,i}\right)^2 \tag{2.8}$$

2.3.5 H/D exchange differential reactor experiments

For the differential reactor experiments, the amount of sample and dilution ratios were varied in order to keep conversion values below 5% of conversion. The flow rate was composed of 5,5 and 10 sccm of H_2, D_2, and Ar respectively at atmospheric pressure. The temperature was increased using a heating ramp rate of 1°C/min in a step-wise manner using intervals of 5°C and keeping the temperature constant for 35 minutes during each step. The main objective of these experiments was to extract the dissociative adsorption and associative desorption kinetic parameters when evaluating the activity in the low and high coverage regimes respectively by performing Arrhenius experiments. Equations C.17 and C.20 show the correlation of the meaning of the apparent activation energies and apparent pre-exponential factors (See Appendix C.3 for the full derivation of equations from the microkinetic model). The composition of the reactor effluent was determined using a Mass Spectrometer with the same methodology described in the previous section for integral experiments.

Chapter 3

Results

3.1 Particle Size Summary

Samples with 0.01, 0.05, and 5% wt loadings of Pt on alumina were prepared by using the Wet Impregnation technique (Appendix A.1) using different calcination and reduction temperatures (T_c and T_r). By performing a statistical analysis we were able to determine the particle size distribution by using HAADF-STEM images as shown in Appendix A.2. Surface average particle diameters,d_{SA}, were determined by using equation 2.1. CO-chemisorption dispersion results were in good agreement with the particle sizes determined by STEM or all samples. H_2 chemisorption was performed as well, however, H_2 was adsorbed at room temperature only on the $Pt_{1.9nm}$ and $Pt_{>1.9nm}$ samples, suggesting stronger binding energy with bigger particle sizes. Table 3.1 summarizes the pretreatment conditions, dispersion from CO and H_2 volumetric chemisorptions, and d_{SA} determined from STEM images.

DRIFTS results of previously calcined and after reduction in H_2 20 % v/v environment are shown in Fig 3.1. The difference between wavenumbers for the linear CO-Pt interaction (2055-2083 m^{-1}) peak maxima suggests a difference in particle size where an increase in the wavenumber corresponds to an increase in the particle size. For the $Pt_{1.9nm}$ and $Pt_{>1.9nm}$ linear CO-Pt interaction appears at a Wavenumber 2071 cm^{-1} suggesting the presence of Pt nanoparticles. However, the $Pt_{>1.9nm}$ also shows a greater relative intensity for the shoulder that appears at 2083 cm^{-1} when compared with the $Pt_{1.9nm}$ sample, suggesting

the presence of bigger nanoparticles for this sample. In fact, the H_2 and CO volumetric chemisorption confirm this last statement by showing lower dispersion values (30% Vs 51.3 % for CO chemisorption). On the other hand for $Pt_{1.3nm}$,$Pt_{0.8nm-SA}$ and Pt_{SA} linear CO-Pt interaction appears at 2055-2058 cm^{-1}, suggesting a smaller particle size. Even though both $Pt_{1.3nm}$ and $Pt_{0.8nm-SA}$ showed similar dispersion values for CO chemisorption (74 Vs 78 %) we believe that the more symmetric spectra for the $Pt_{0.8nm-SA}$ was a strong indication that this sample has a smaller average particle size. This was confirmed from the STEM images results (Appendix A.2) where we got d_{SA} of 0.8 and 1.3 nm respectively for $Pt_{0.8nm-SA}$ and $Pt_{1.3nm}$ samples. The difference in size between these two samples is attributed not only to the different calcination and reduction temperatures but also to the different precursors used during Wet Impregnation, where the usage of tetraamineplatinum (II) nitrate precursor results in smaller average surface diameter.

Table 3.1: Dispersion values and average size of Pt/Al_2O_3 catalysts

				Dispersion[a]		
Method	Pt w/w %	Tc/Tr [°C]	Denoted as	H2	CO	Surface Average diameter[b] [nm]
WI[c]	0.01	300/200	Pt_{SA}	-	-	SA
WI[c]	0.05	300/200	$Pt_{0.8nm-SA}$	-	74 %	0.8nm and SA
WI[d]	0.05	300/250	$Pt_{1.3nm}$	-	78%	1.3
WI[d]	5	400/400	$Pt_{1.9nm}$	53%	51.3%	1.9
WI[d]	5	550/700	$Pt_{>1.9nm}$	30%	30%	>1.9

a: Determined by chemisorption

b: Determined by STEM images analysis

c: Using Tetraammineplatinum(II) nitrate precursor

d: Using Chloroplatinic acid solution precursor

Figure 3.2 showed a comparison of the intensity in absorbance units for the $Pt_{1.9nm}$, $Pt_{0.8nm-SA}$, and Pt_{SA} samples. It should be noted that the intensity of the signals where the CO-Pt interactions appear decreased by orders of magnitude from 1.25 to 0.035 to 0.0025 absorbance units for $Pt_{1.9nm}$, $Pt_{0.8nm-SA}$ and Pt_{SA} respectively. We attribute this difference in intensities

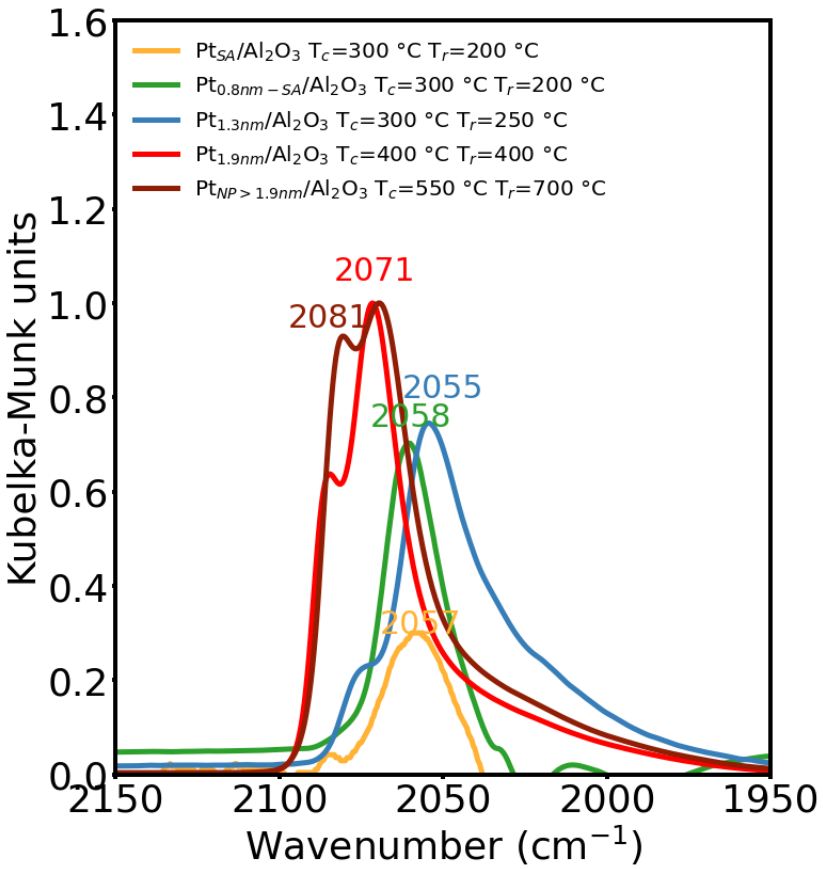

Figure 3.1: DRIFTS spectra of CO adsorption on the Pt/Al_2O_3 samples after reduction in H_2 20% environment.

to the different atomic percentages of Pt coming from NP and subnanoclusters determined from STEM images (Appendix. A). Since the $Pt_{1.9nm}$ was mainly conformed by NP we can assign the corresponding signal at 2071 cm^{-1} to NP. On the other hand, $Pt_{0.8nm-SA}$ and Pt_{SA} samples showed the presence of subnanoclusters to which we attribute the signal at 2057 cm^{-1}.

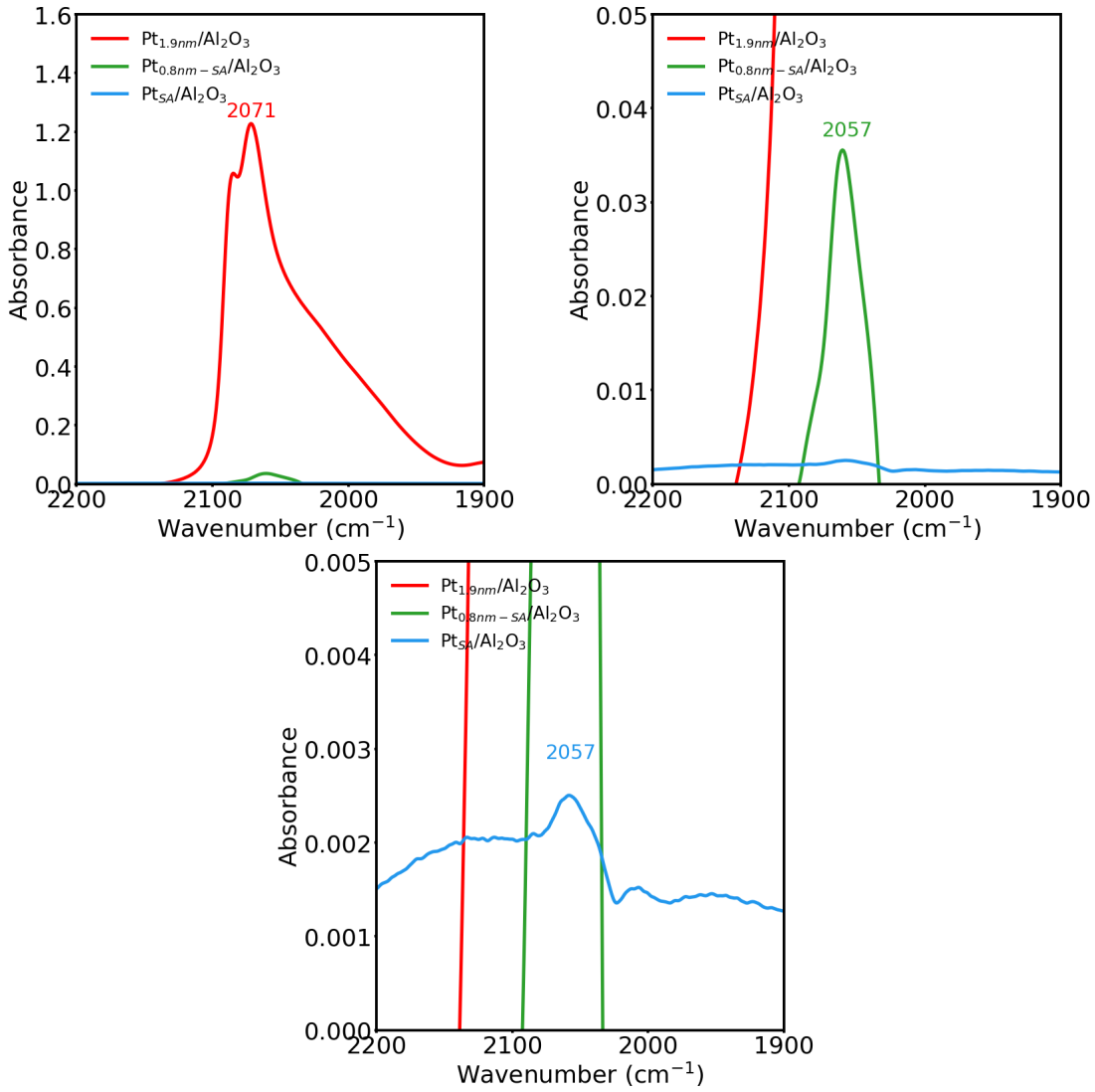

Figure 3.2: DRIFTS in Absorbance units for $Pt_{1.9nm}$, $Pt_{0.8nm-SA}$, and Pt_{SA} on Al_2O_3

3.2 X-ray absorption spectroscopy

3.2.1 $Pt_{1.9nm}/Al_2O_3$ under H_2 environment at different T

To probe the local environment of the Pt species and their oxidation state, X-ray absorption spectroscopy (XAS) was performed at Pt L_3-edge. Spectra were collected at room temperature, 100, 200,300 and 400 °C for the $Pt_{1.9nm}/Al_2O_3$ sample under a 50 % v/v H_2 environment in He after in situ pretreatment in 20% v/v H_2 at 400 °C and cooling down in H_2 and He environment. The objective of this experiment was to verify whether or not the coordination of Pt atoms changed along this T range given the 2D-3D particle shape transitions and mobility of NP previously reported in the literature at high temperatures for Pt/Al_2O_3 samples [19] [20]. Figure 3.3 shows the XANES and R-space for $Pt_{1.9nm}/Al_2O_3$ sample at different temperatures. Table 3.2 summarizes the EXAFS modeling fitting parameters for Pt-Pt at different temperatures.

From Figures 3.3 and 3.4 in R-space for the $Pt_{1.9nm}/Al_2O_3$ it can be noticed that the intensity of the $|\chi(R)$ Re $[\chi(R)]$ and Im $[\chi(R)]$ parts decreases with increasing temperature. This is due to the increasing value of the Debye-Walle factor σ^2_{Pt-Pt}, which accounts for the disorder in a sample by modeling it as a Gaussian distribution; as σ^2_{Pt-Pt} increases with temperature, scattering amplitude decreases. Table 3.2 summarizes the parameters fitting values in r-space using Artemis by varying the coordination numbers of the single scattering paths (N_{Pt-Pt}), the effective scattering lengths (R_{Pt-Pt}), the bond-length disorder (σ^2_{Pt-Pt}), and the correction to the threshold energy, ΔE_0, for Pt-Pt path. The changes in the first-shell coordination number N_{Pt-Pt} under a 50%v/v H_2 varied from 7.69 ± to 6.2 ± 0.8 from room T to 400 °C respectively. This changes are important since they indicate that the structure of the nanoparticles formed after pretreatment can change over wide temperature in H_2 rich environments. In fact, and as shown in Fig 3.5, this change in structure has been

experimentally observed while performing light-off experiments during the H/D exchange reaction on the $Pt_{1.9nm}/Al_2O_3$. A dip in activity can be noticeable between 275-375 °C which happens inside the same T range where the anomaly on the N_{Pt-Pt} change is observed.

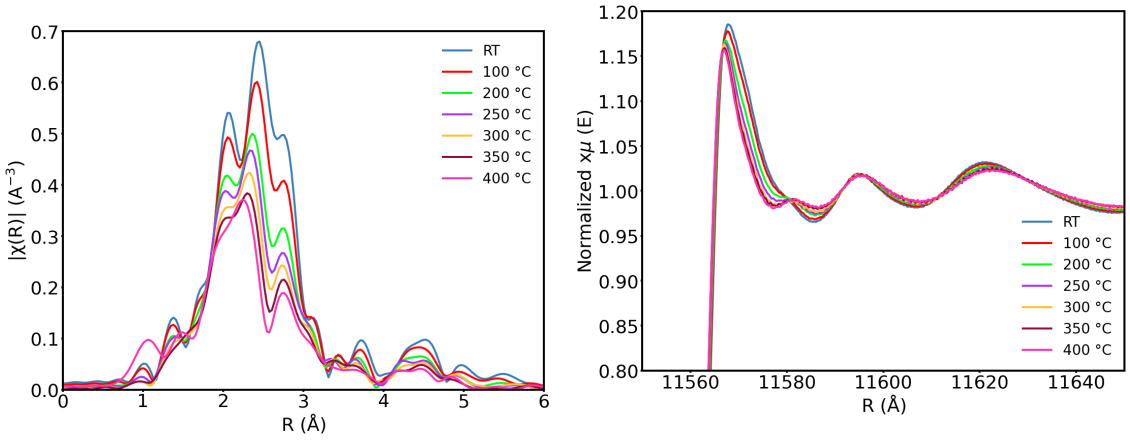

Figure 3.3: Magnitude of the Fourier-transformed k2 -weighted χ (k) data (Δk = 3—14.75 Å—1) in R-space of $Pt_{1.9nm}/Al_2O_3$ and XANES Spectra after pretreatment under a 50% v/v H_2 balance with He from RT to 400 °C

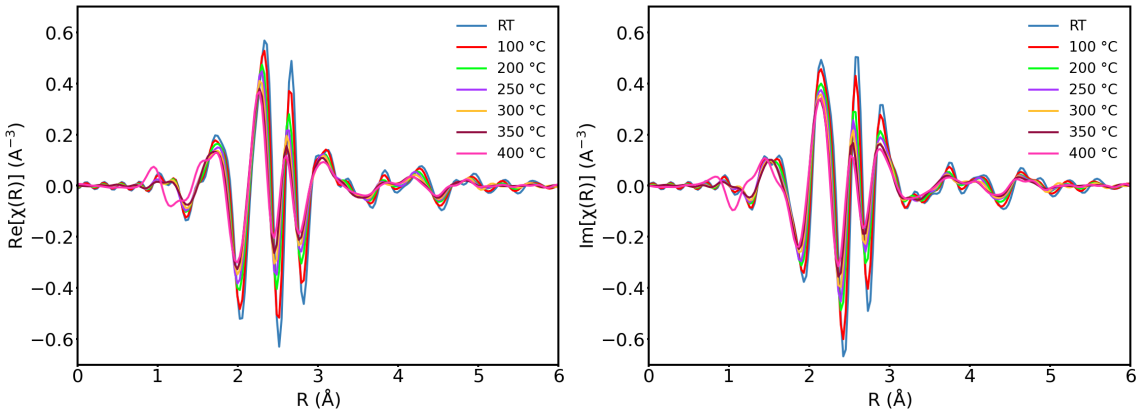

Figure 3.4: Real (Re) and Imaginary (Im) parts of the Fourier-transformed k2 -weighted χ (k) data (Δk = 3—14.75 Å—1) in R-space of $Pt_{1.9nm}/Al_2O_3$ after pretreatment under a 50% v/v H_2 balance with He environment from room temperature to 400 °C

Table 3.2: Summary of the EXAFS modeling parameters fitting results for $Pt_{1.9nm}/Al_2O_3$ after in situ reduction under 50%v/v H_2 environment from Room temperature to 200 °C

Parameter	RT[a]	RT	100 °C	200 °C
N_{Pt-Pt}	7.42 ± 0.4	7.69 ± 0.4	7.42 ± 0.5	6.98 ± 0.5
R_{Pt-Pt} (Å)	2.71 ± 0.003	2.73 ± 0.003	2.71 ± 0.0038	2.69 ± 0.005
σ^2_{Pt-Pt}(Å^2) x 10^3	8.41 ± 0.3	8.53 ± 0.3	9.3 ± 0.4	10.4 ± 0.6
ΔE_{0Pt-Pt} (eV)	4.25 ± 0.5	4.23 ± 0.5	4.11 ± 0.6	3.13 ± 0.7
reduced χ^2	582.5	846.1	539.8	332
R factor	0.0051	0.0054	0.0079	0.011

a, under He flow only at Room Temperature, N, the coordination number of the absorber-backscatter pair; R, radial absorber-backscatter distance;σ^2, mean-square displacement of the half-path length; ΔE_0, correction to the threshold energy.

Table 3.3: Summary of the EXAFS modeling parameters fitting results for $Pt_{1.9nm}/Al_2O_3$ after in situ reduction under 50%v/v H_2 environment at different temperatures.

Parameter	250 °C	300 °C	350 °C	400 °C
N_{Pt-Pt}	6.79 ± 0.6	6.34 ± 0.7	6.32 ± 0.6	6.2 ± 0.8
R_{Pt-Pt} (Å)	2.69 ± 0.006	2.68 ± 0.007	2.67 ± 0.007	2.67 ± 0.005
σ^2_{Pt-Pt}(Å^2) x 10^3	11.1 ± 0.7	11.4 ± 0.8	12.3 ± 0.9	13.1 ± 1.2
ΔE_{0Pt-Pt} (eV)	3.05 ± 0.9	2.87 ± 1	3.14 ± 0.9	2.8
reduced χ^2	384	293	200	426
R factor	0.0168	0.02	0.018	0.026

N, the coordination number of the absorber-backscatter pair; R, radial absorber-backscatter distance;σ^2, mean-square displacement of the half-path length; ΔE_0, correction to the threshold energy.

The changes in N_{Pt-Pt} and the anomaly in $Pt_{1.9nm}/Al_2O_3$ activity during the H/D exchange reaction are relevant since this is the first time experimental evidence is provided regarding the effect of small H_2O concentrations coming from the reduction step of the sample and H_2 presence on the coordination number for $Pt//Al_2O_3$ samples at moderate temperatures. Recalling Lisitsyn et. al. [19] hypothesis, H_2O and H_2 can induce the generation of anionic oxygen vacancies in the support and consequently cause reversible 2D-3D transitions for the shape of the Pt clusters (Fig. 1.9) this in order to maximize the adsorption capacity towards hydrogen by weakening the metal-support interactions. Thus we believe that this kind of 2D-3D transition is taking place between 275-375 °C since both the dip in F_{HD} generation

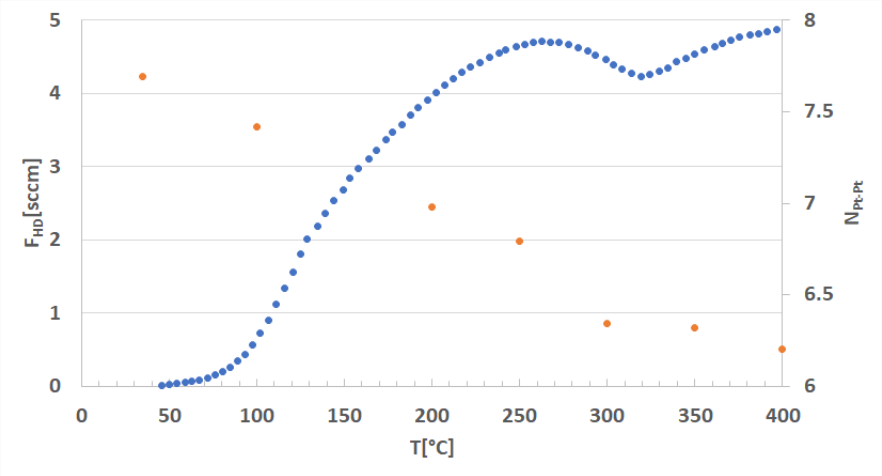

Figure 3.5: Light-off plot (blue dots) and N_{Pt-Pt} (orange dots) Vs T for $Pt_{1.9nm}/Al_2O_3$ after pretreatment under a 50% v/v H_2 balance with He from RT to 400 °C
. H/D exchange using 5-5-10 sccm (H_2-D_2-Ar)

and N_{Pt-Pt} can be strongly related to any kind of Pt nanoparticles restructuring.

The reversibility of the Pt nanoparticles restructuring was confirmed by taking the Spectra at room T under 50% v/v H_2 and He of the sample after being exposed to 400 °C. As shown in Fig 3.6 the Spectra of the $Pt_{1.9nm}/Al_2O_3$ samples at room T show the same intensity after being exposed at high T. Table 3.4 shows the EXAFS fitting values for the spectra shown in Figure 3.6. An interesting effect is a slight difference between the spectra under 50% v/v H_2 and He only. R_{Pt-Pt} changed from 2.73 to 2.71 (Table 3.4) at room temperature under 50% v/v H_2 and He only environments respectively. This increase in the distance under a 50% v/v H_2 although it seems negligible is in fact a product of the H_2 adsorption on the Pt nanoparticles at room T. Showing how sensitive the sample is to compositional changes in the reaction environment.

Table 3.4: Summary of the EXAFS modeling parameters fitting results for $Pt_{1.9nm}/Al_2O_3$ after in situ reduction under 50%v/v H_2 environment at different temperatures.

Parameter	He	50%v/v H_2
N_{Pt-Pt}	7.42 ± 0.4	7.69 ± 0.4
R_{Pt-Pt} (Å)	2.71 ± 0.003	2.73 ± 0.003
σ^2_{Pt-Pt}(Å^2) x 10^3	8.41 ± 0.3	8.53 ± 0.3
$\Delta E_{0\,Pt-Pt}$ (eV)	4.25 ± 0.5	4.23 ± 0.5
reduced χ^2	582.5	846.1
R factor	0.0051	0.0054

N, coordination number of the absorber-backscatter pair; R, radial absorber-backscatter distance;σ^2, mean-square displacement of the half-path length; ΔE_0, correction to the threshold energy.

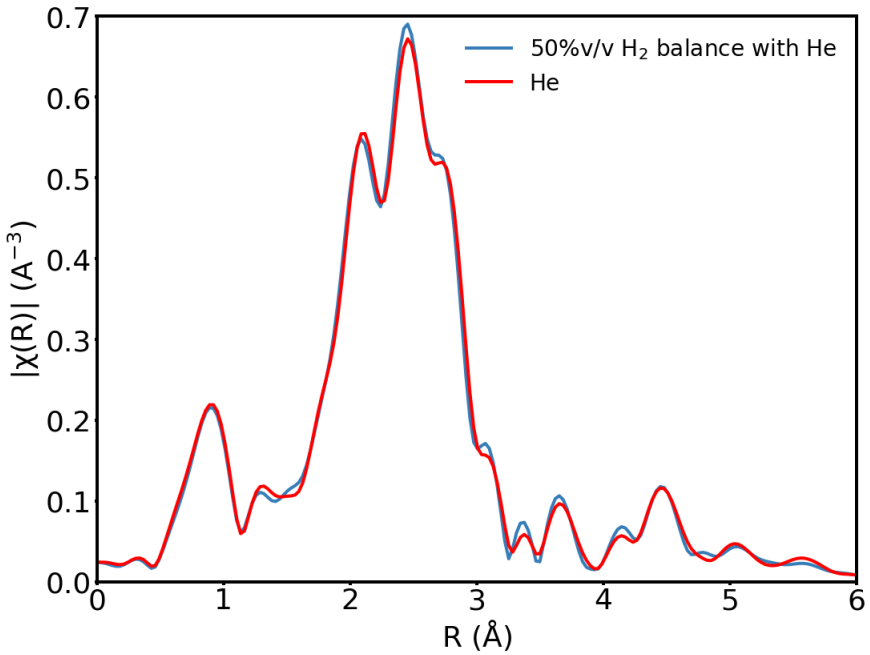

Figure 3.6: Magnitude of the Fourier-transformed k2 -weighted χ (k) data (Δk = 3−14.75 Å−1) in R-space of $Pt_{1.9nm}/Al_2O_3$ after pretreatment under a 50% v/v H_2 balance with He and He only environment at room temperature

3.2.2 $Pt_{1.3nm}/Al_2O_3$ EXAFS

On the other hand for the $Pt_{1.3nm}$ Spectra were collected at room temperature after in situ pretreatment in 20% v/v H_2 at 250 °C in 20 and 50% H_2 environment at room temperature (Figure 3.7). The goal of this experiment was to see if the particle size/average coordination number changes with different concentrations of H_2 since smaller particles tend to sinter easier due to their increased mobility. Table 3.5 shows the EXAFS fitting parameters values. As it can be noticed N_{Pt-Pt} doesn't significantly change under different H_2 concentrations (20 and 50 % v/v) going from x to y respectively at room T. Similarly, R_{Pt-Pt} change from x to y for the 20 and 50 % v/v H_2 in He environments. Something important to notice is that the first-shell N_{Pt-Pt} values determined by EXAFS for this $Pt_{1.3nm}$ corresponds to a smaller particle size than the ones determined by STEM images analysis and CO-chemisorption. We think that these differences in average particle sizes are due to the presence of a "raft-like" particle shape on the support (See Appendix A.2 for STEM images). These 2-D/raft-like structures have been previously reported in the literature for low weight loading Pt/Al_2O_3 with similar pretreatment temperatures i.e. below or equal to 300 °C for calcination and reduction with H_2. The different assumptions regarding the morphology of the Pt nanoparticles either hemispherical or flat particles can derive in different N_{Pt-Pt}, the reason to which we attribute this coordination number difference. Unlike the $Pt_{1.9nm}$ sample which has a nominal weight of 5% Pt/Al_2O_3 It is important to notice that the nominal weight for this sample was 0.05 % Pt/Al_2O_3 which made more difficult to detect smalls differences on the spectra over T during reduction which is why the spectra were taken only after reduction at room temperature.

Table 3.6 shows the EXAFS fitting values for the different Pt particle sizes $Pt_{1.9nm}$ and $Pt_{1.3nm}$ after pretreatment at room T. Contrasting N_{Pt-Pt} values of x and y and R_{Pt-Pt} values of x and y for $Pt_{1.9nm}$ and $Pt_{1.3nm}$ respectively were found. The first-shell coordi-

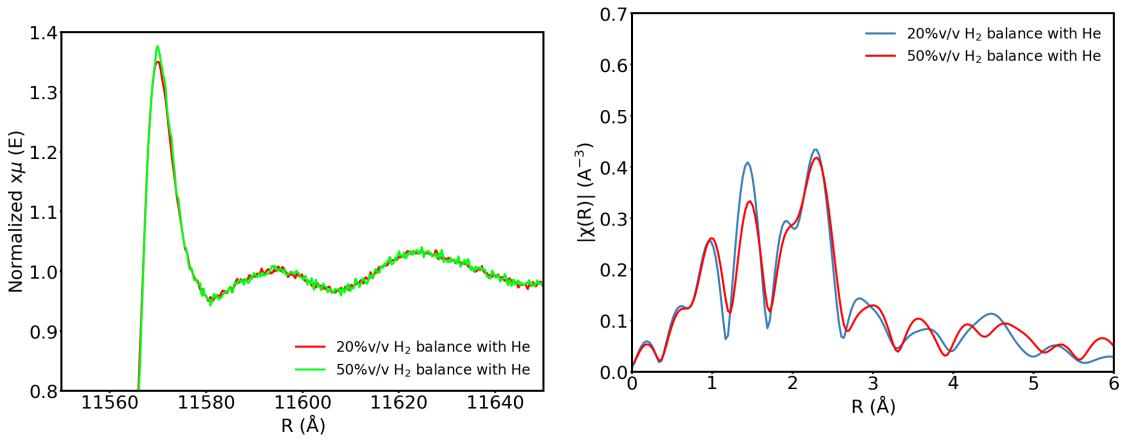

Figure 3.7: Pt L3 XANES and magnitude of the Fourier-transformed k2 -weighted χ (k) data (Δk = 3−14.75 Å−1) in R-space of $Pt_{1.3nm}/Al_2O_3$ after pretreatment under 20 and 50% v/v H_2 balance with He environment at room temperature

Table 3.5: Summary of the EXAFS modeling parameters fitting results for $Pt_{1.3nm}/Al_2O_3$ after in situ reduction under 20 %v/v H_2 environment at room temperature.

Parameter	20%v/v H_2
N_{Pt-Pt}	4.85 ± 1.33
R_{Pt-Pt} (Å)	2.715 ± 0.011
σ^2_{Pt-Pt}(Å^2)	9.85 ± 2.48
ΔE_{0Pt-Pt} (eV)	4.5
reduced χ^2	2.273
R factor	0.0311

nation numbers N_{Pt-Pt} were in strong agreement with the particle sizes determined by CO chemisorption and STEM images analysis shown in Table 3.1 for the $Pt_{1.9nm}$ sample. On the other hand, N_{Pt-Pt} for $Pt_{1.3nm}$ corresponds to a smaller particle size than the one determined by STEM image analysis. We believe the difference in the average particle is due to the presence of raft-like/2D particle structures present on the $Pt_{1.3nm}$ sample.

Table 3.6: Summary of the EXAFS modeling parameters fitting results for $Pt_{1.9nm}/Al_2O_3$ and $Pt_{1.9nm}/Al_2O_3$ after in situ reduction under 20 %v/v H_2 environment at room temperature.

Parameter	$Pt_{1.9nm}/Al_2O_3$	$Pt_{1.3nm}/Al_2O_3$
N_{Pt-Pt}	7.69 ± 0.4	4.85 ± 1.33
R_{Pt-Pt} (Å)	2.73 ± 0.003	2.715 ± 0.011
σ^2_{Pt-Pt}(Å^2)	8.53 ± 0.3	9.85 ± 2.48
$\Delta E_{0\,Pt-Pt}$ (eV)	4.23 ± 0.5	4.5
reduced χ^2	846.1	2.273
R factor	0.0054	0.0311

3.3 Light-off experiments

3.3.1 Exploration for optimal operation conditions: dilution ratio

In order to evaluate the kinetic activity under the kinetic regime, dilution of catalysts with SiO_2 (calcined at 850 °C for 8h) was necessary. The effect of the dilutions ratio during light-off experiments is shown in the following graph where we evaluated the catalytic activity for the $Pt_{1.9nm}/Al_2O_3$ (5%wt of Pt on Al_2O_3) while keeping the mass of diluted catalyst constant at 300 mg (sieve fraction 106-180 microns), and using a flow rate composed of 5-5-10 sccm (H_2-D_2-Ar). The conversion was evaluated over a wide T range from room T to 600K. All samples were previously reduced in a 20%H_2 environment for 2h @ 400 °C

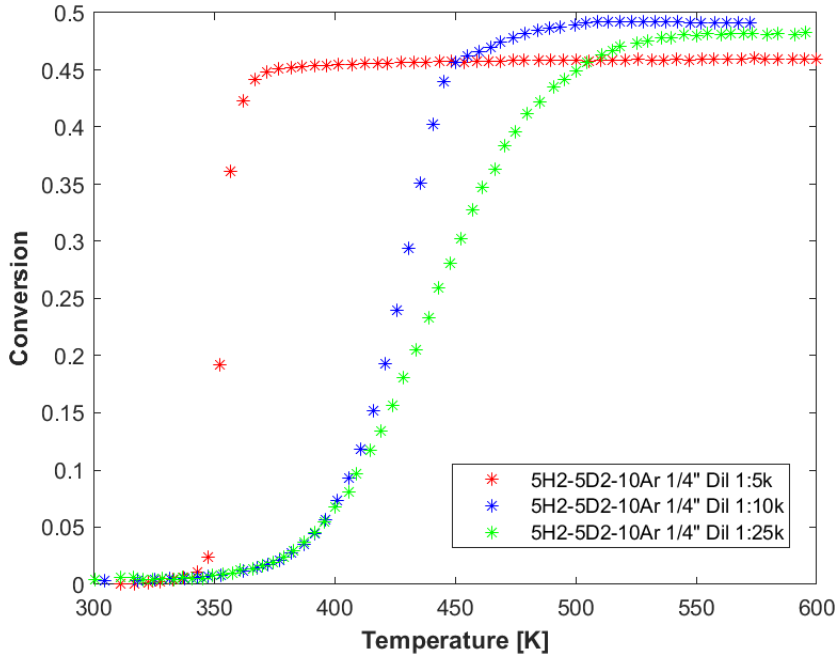

Figure 3.8: Dilution ratio effect on X vs T for $Pt_{1.9nm}/Al_2O_3$ sample.

From Figure 3.8 is noticeable that the lower the dilution ratio the lower the temperature necessary to reach equilibrium conversion. The non-linear fitting for the different kinetic parameters was found to be extremely sensitive to the transition T range (the temperature

Table 3.7: Kinetic parameters for different dilution ratios $Pt_{1.9nm}/Al_2O_3$ catalysts

		Dilution ratios [mcat:mdiluent]		
	Kinetic parameters	1:25k	1:10k	1:5k
Adsorption	E_{ads} [kJ/mol]	0 ±3	0 ±5	-
	v_{ads} [1/s/Pa]	2.4 x $10^{-1\pm0.2}$	4.6 x $10^{-3\pm0.1}$	
Desorption	E_{des} [kJ/mol]	96 ±4	204 ±13	-
	v_{des} [1/s]	1.2 x $10^{15\pm0.5}$	2.0 x $10^{28\pm1.6}$	-

range where the conversion dramatically increases). In table 3.7 we can notice how the desorption kinetic parameters E_{des} almost doubled from 96 ± 4 to 204 ± 13 kJ/mol when going from 1:5k to 1:10k dilution ratio. Similarly, v_{des} values show an increase from 3.2 x $10^{12\pm0.5}$ to 5.25 x $10^{25\pm1.6}$ when comparing the previous mentioned dilution ratios. This effect continued increasing while decreasing the dilution ratio so that for the 1:5k the numerical solutions gave results with $E_{des} > 300$ kJ/mol due to the narrower T range where the pronounced increase of conversion occurs. Retaking the 1:5k dilution ratio case, we believe that the sudden increase of conversion over T occurs as a consequence of local increases of T due to the higher amount of heat released during the isotopic exchange reaction. In order to assure that no mass or energy transfer limitations were happening for the 1:25k case, we made sure to comply with the external and intraparticle mass and energy transfer limitations criterion described in Appendix B. From this set of experiments, we decided that for the light-off experiment only dilution ratios greater than 1:25k should be used during light-off experiments in order to avoid mass and energy transfer limitations.

3.4 $Pt_{1.9nm}/Al_2O_3$ kinetic parameters

To determine the energy barriers and pre-exponential factors for adsorption and desorption for the $Pt_{1.9nm}$ particle size we made use of both light-off experiments and Arrhenius experiments at low temperatures and high coverages to be able to compare the values of

the parameters using two different types of experiments. The results for the light-off experiments are shown in Fig 3.9 where both HD flow rate and coverage are represented by solid lines by modeling equations 3.1 and 3.2 (see Appendix C for development of equations) using the kinetic parameters extracted from the non-linear fitting. The root mean square error function was used the perform the non-linear fitting by following Equation 2.8 in the previous chapter: $Error = \frac{1}{N}\sum_{i=1}^{N}\left(F_{HD,out,i}^{exp} - F_{HD,out,i}\right)^2$. Details regarding the determination of uncertainties for the non-linear fitting are described in Appendix E. No significant change in the numerical value of the kinetic parameters was detected depending on the number of experimental points used at conversions near equilibrium. In contrast, fitting values were sensitive to the shape of the light-off plots. Such an effect was previously shown and described in section 3.3.1.

Arrhenius experiments (Figure 3.10) were carried at temperatures below 100 °C to evaluate the activity under high coverage which allowed us to extract E_{des} and k_{des} (See Appendix C.3 for high and low coverage regime equation derivation). Kinetic parameter values for the $Pt_{1.9nm}$ are summarized in table 3.8.

$$F_{HD,out} = F_{H_2,feed}\left(1 - \exp\left(-\frac{mk_{ads}P_{total}}{F_{total}\left(1+\sqrt{2\frac{k_{ads}}{k_{des}}P_{H_2feed}}\right)^2}\right)\right) \tag{3.1}$$

$$\theta = \frac{\sqrt{2\frac{k_{ads}}{k_{des}}P_{H_2feed}}}{1+\sqrt{2\frac{k_{ads}}{k_{des}}P_{H_2feed}}} \tag{3.2}$$

As we can see from table 3.3 for both type of experiments results for the desorption energy barriers and pre-exponential factors seems to be in good agreement with E_{des}=96 kJ/mol ± 4 and E_{des}=96 kJ/mol ± 1 and 3.2 x $10^{12\pm0.5}$ and 3.8 x $10^{13\pm0.2}$ [1/s/Pa] respectively for the light-off and Arrhenius experiments. By the other hand it H_2 adsorption kinetic parameters

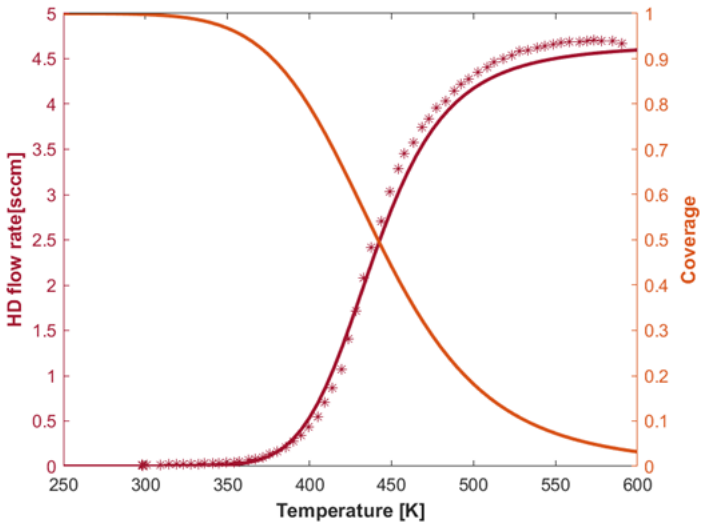

Figure 3.9: Light-off experiment for $Pt_{1.9nm}/Al_2O_3$ sample. Total flow rate = 20 sccm, 5-5-10 sccm (H_2-D_2-Ar). m_{cat}=300 mg. Dil ratio 1:25k. Solid lines theoretical values using equations 3.1 and 3.2 and kinetic parameters from non-linear fitting. * experimental data points.

were determined only for the non-linear fitting performed to the light-off experiments. A E_{ads}= 0 ± 3 and v_{ads}= 2.4 x $10^{-1\pm0.2}$. The explanation behind why E_{ads} is so low might be related to the fact that for Nanoparticles is easier to dissociate H_2 molecules. Conversely, due to the stronger interaction between Pt-H in the nanoparticle regime is more difficult to desorp H or D atoms once they are recombined in the catalytic surface following a recombination mechanism (Table 1.2 and Appendix C.1 for more details regarding the reaction mechanism).

Table 3.8: Kinetic parameters $Pt_{1.9nm}/Al_2O_3$

	Kinetic parameters	Light-off	Arrhenius	Literature
Adsorption	E_{ads} [kJ/mol]	0 ±3	-	-
	v_{ads} [1/s/Pa]	2.4 x $10^{-1\pm0.2}$	-	-
Desorption	E_{des} [kJ/mol]	96 ±4	96 ±1	
	v_{des} [1/s]	1.2 x $10^{15\pm0.5}$	7.4 x $10^{15\pm0.2}$	-
	Heat of H_2 adsorption $E_{ads} = E_{ads}$- E_{des} [kJ/mol]	-96 ±7	-	-90[9],a, -96[12],b, -105[7],a.

a: Determined by calorimetry

b: Determined by TPD

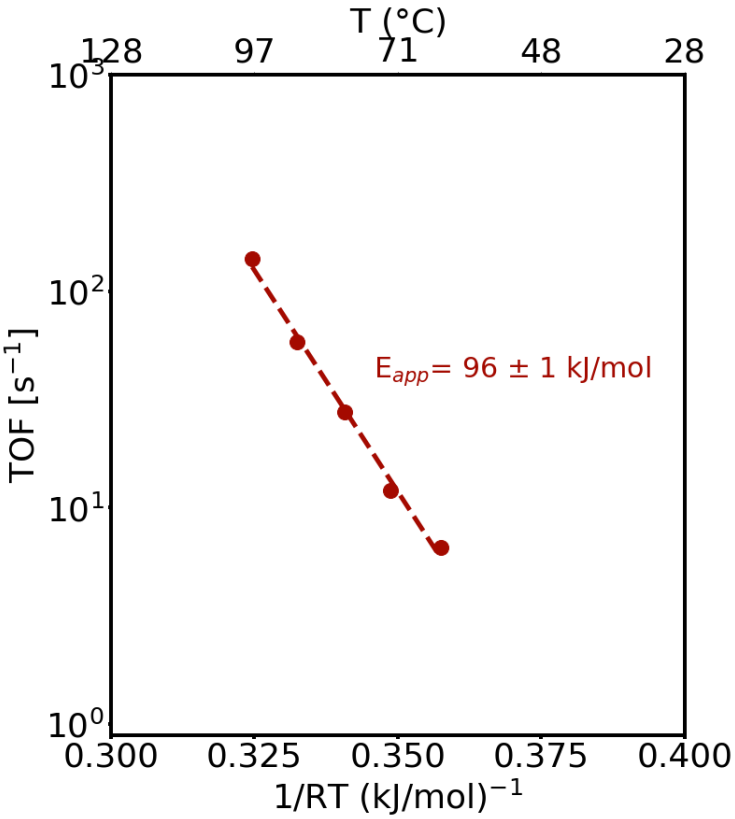

Figure 3.10: Arrhenius plot experiment for $Pt_{1.9nm}/Al_2O_3$ sample. Total flow rate = 20 sccm, 5-5-10 sccm (H_2-D_2-Ar). m_{cat}=250 mg. Dil ratio 1:25k.

Furthermore, values determines from the two different methodologies for this sample are in good agreement with heats of H_2 adsorption previously reported in the literature for supported Pt nanoparticles (90-116 kJ/mol determined by calorimetry or TPD experiments) as well as for the Pt(111) lattice plane (98 kJ/mol).

3.5 Coverage effect on Pt/Al_2O_3 E_{app} during H/D exchange reaction

When applying the E_{app} definition equation to the forward reaction rate derived from the microkinetic model for the recombination mechanism (full derivation in Appendix C.3) we end with different interpretations for E_{app} that strongly depend on the coverage regime under which the activity was evaluated.

If r_f is evaluated in the high coverage regime,that is $\theta \to 1$ where $k_{ads} \gg k_{des}$ the reaction rate equation turns into a function of the associative desorption kinetic parameters k_{des} and v_{des}, so that E_{app}=E_{des} (Equation 3.3).

$$\ln r_f = \ln 2\nu_{des} - \left(\frac{E_{des}}{k_b T}\right) \tag{3.3}$$

Conversely,when r_f is evaluated in the low coverage regime,that is $\theta \to 0$ where $k_{des} \gg k_{ads}$ the reaction rate equation turns into a function of the dissociative adsorption kinetic parameters k_{ads} and v_{ads}, so that E_{app}=E_{ads} (Equation 3.4).

$$\ln r_f = \ln P_{H_2 feed}\nu_{ads} - \left(\frac{E_{ads}}{k_b T}\right) \tag{3.4}$$

Consistent with the previous description, the general E_{app} definition applied on r_f and after simplification is expressed in equation 3.5, which obeys the fact that under high coverage regimes, ($\theta \to 1$), then E_{app}= E_{des}. Conversely, when $\theta \to 0$, then E_{app}= E_{ads}.

$$E_{app} = E_{ads} - \theta\left(E_{ads} - E_{des}\right) \tag{3.5}$$

In order to verify experimentally if coverage has an effect on E_{app} we decided to evaluate the activity at different temperatures and different H_2/D_2 partial pressures. It is known that coverage is a function of both T and P. So, at higher temperatures and lower partial pressures, we should expect lower coverage values. Consequently, E_{app} should show lower values by following equation 3.5.

For the $Pt_{1.9nm}/Al_2O_3$ sample for which parameters were previously determined (Tabe 3.8) we can notice that E_{ads} 0. Thus, equation 3.5 reduces to:

$$E_{app} = \theta E_{des} \tag{3.6}$$

E_{app}=96 kJ/mol was previously determined from the H/D exchange experiment using P_{H_2}= P_{D_2}= 25 kPa inside the T range 333-353 K. In contrast when evaluating the activity for the same sample using P_{H_2}= P_{D_2}= 5 kPa at a T range 383-403 K the E_{app} value decreased to 53 kJ/mol Figure 3.11

We believe that the difference in E_{app} is related to the coverage values corresponding to the temperatures and partial pressures where activity was evaluated. Figure 3.12 shows the theoretical coverage values (Equation 3.2) as a function of T and total pressure $P_{H_2-D_2}$= P_{H_2} + P_{D_2} for the $Pt_{1.9nm}$ sample using the kinetic parameters from table 3.8. As we can notice for a $P_{H_2-D_2}$=12.5 kPa and T range 383-403 coverage values would be between 60-70 %. In order to determine the experimental coverage values for the $Pt_{1.9nm}$ sample, H_2 isotherms over a wide pressure range (0.01 to 10 kPa) were taken at 373, 423, and 473 K (Figure 3.13). As we can see from the isotherms plots, between 373 and 423 K coverage values drop from 0.61 to 0.42 approximately at a total pressure of 10kPa of H_2. Such low coverage values provide more evidence that for the experiment carried out between 383-403 K using P_{H_2}= P_{D_2}= 5 kPa (E_{app}=52 kJ/mol from Figure 3.11) coverage was significantly

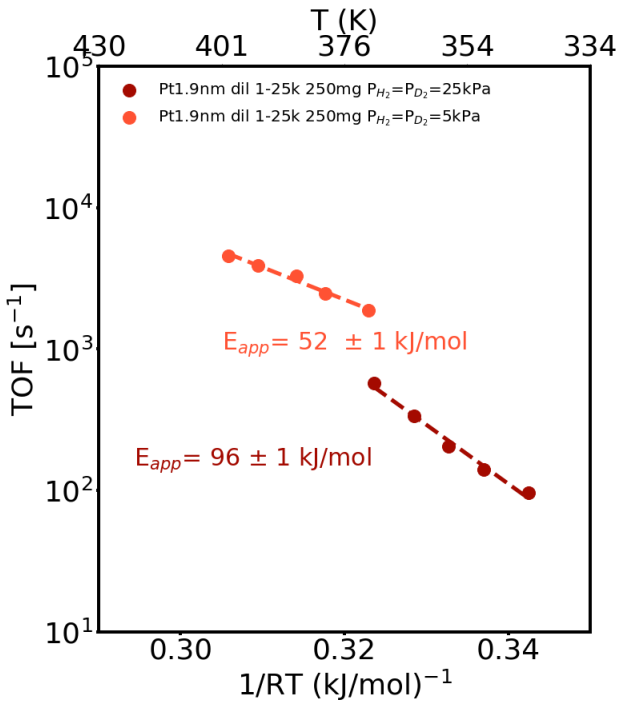

Figure 3.11: $Pt_{1.9nm}/Al_2O_3$ E_{app} at different T ranges and Pp values.

lower than 1, showing the coverage effect predicted from equation 3.6 for the recombination reaction mechanism.

By performing a similar analysis for the $Pt_{0.8nm-SAnm}/Al_2O_3$ sample we also found a difference in E_{app} dependent on the evaluation T range and Partial pressures. When activity was evaluated between 355-380 K and P_{H_2}= P_{D_2}= 25 kPa E_{app}=94 kJ/mol. In contrast, when activity was evaluated at higher Temperatures 385-425K and lower partial pressures P_{H_2}= P_{D_2}= 5 kPa, E_{app}= 69 kJ/mol (Fig 3.14).

We believe that this change in E_{app} is also related to differences in coverage. Something important to notice is that the difference in coverage was less remarked on the $Pt_{0.8nm-SAnm}/Al_2O_3$ (total drop of 25 kJ/mol from 85 to 69 kJ/mol) than for the $Pt_{1.9nm}/Al_2O_3$ (total drop of 44 kJ/mol from 96 to 52 kJ/mol). This can be due to differences in coverage over T and P strongly dependent on the particle size.

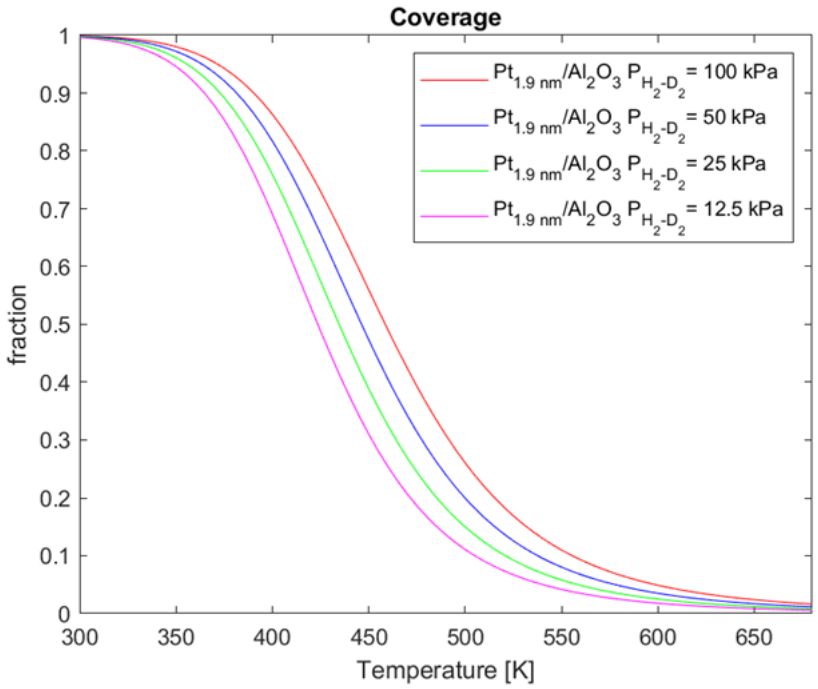

Figure 3.12: $Pt_{1.9nm}/Al_2O_3$ Coverage Vs T simulations at different partial pressures

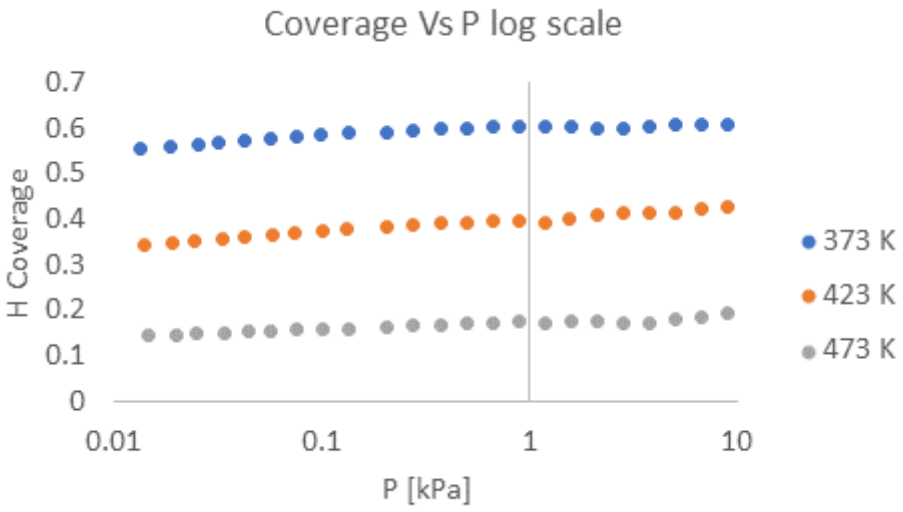

Figure 3.13: $Pt_{1.9nm}/Al_2O_3$ Coverage Vs T simulations at different partial pressures

In addition to the previous results evaluation of Pt_{SA}/Al_2O_3 was also performed between 355-380 K and P_{H_2}= P_{D_2}= 25 kPa and in the T range between 385-425K and lower partial pressures P_{H_2}= P_{D_2}= 5 kPa. In a similar way to the two previous samples with bigger size

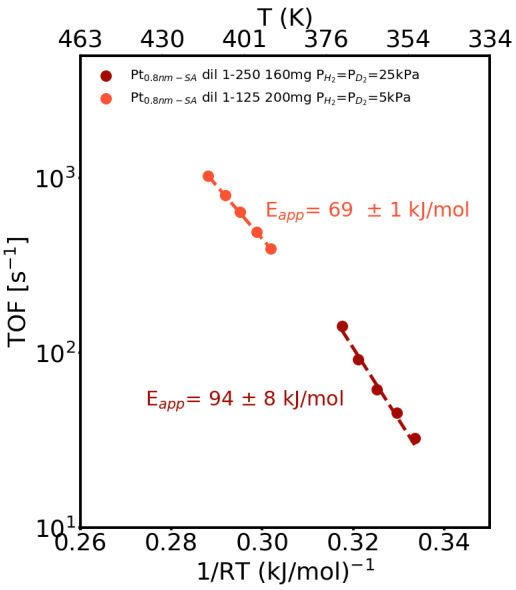

Figure 3.14: $Pt_{0.8nm-SA}/Al_2O_3$ Coverage Vs T simulations at different partial pressures

a drop on E_{app} was observed from 108 to 68 kJ/mol respectively (Figure 3.15). We believe that the drop in E_{app} was also related to changes in the coverage values. Even though this sample was mainly conformed by single atoms it also showed the presence of subnanoclusters as shown in the STEM images (Appendix A. Figure A.4). We believe that the similarities in behavior are derived from the presence of subnanoclusters in this sample. Further evidence for this is the similar E_{app} values but lower TOF which indicates the exchange reactions might be taking place on the same type of active site, i.e. NP and subnanoclusters. Further quantitative analysis of the kinetic parameter values determined during the H/D exchange reaction is described in the next section.

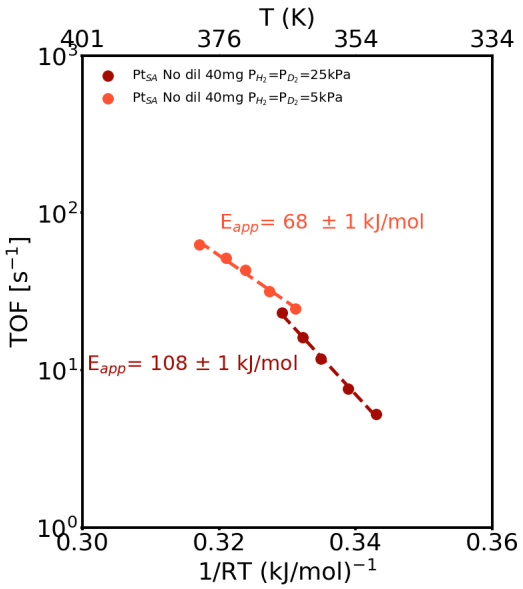

Figure 3.15: Pt_{SA}/Al_2O_3 Coverage Vs T simulations at different partial pressures

3.6 Structure sensitivity for Pt/Al_2O_3 during H/D exchange reaction

Figure 3.16 shows the activity in TOF from Arrhenius experiments at similar T ranges and Table 3.9 the values for the kinetic parameters for adsorption and desorption of H_2 on the $Pt_{1.9nm}$, $Pt_{0.8nm-SA}$, and Pt_{SA} samples. E_{des} decreased from 96± 1 to 85 ± 4 and then increased to 108 kJ/mol ± 3 when downsizing the particle size from 1.9 to 0.8nm (subnanoclusters) and then to SA respectively, Conversely, the frequency factor v_{des} decreased from 7.4 x 10^{15} ± 0.2 for the 1.9 nm size to 2.8 x $10^{15\pm0.1}$ 1/s for the 0.8nm particle size and then increased to 1.4 x $10^{17\pm0.8}$ for SA, suggesting a possible compensation effect between the different particle size regimes (NP, subnanoclusters, and SA). However, the more negative value of heats of H_2 of adsorption of the NP compared to the subnanoclusters suggests a greater stability of H_2 adsorbed on bigger nanoparticles and hence more activity. Figure 3.14 shows the difference in activity (normalized per Pt site) from Arrhenius plots at low T and high coverage regime (E_{app}=E_{des}) for samples $Pt_{1.9nm}$, $Pt_{1.3nm}$ and $Pt_{0.8nm-SA}$. As it can be noticed the $Pt_{0.8nm-SA}$ and Pt_{SA} showed lower activity compared to the $Pt_{1.9nm}$ sample.Something important to notice is the similarity in the trending as a function of particle size where an increase in activity was observed when increasing the particle size from SA to clusters to NP. This is in good agreement with the acetylene semi-hydrogenation reaction activity trends on Pt/TiO_2 catalysts where the catalytic activity increases while increasing the Pt particle size [5]. We believe that the lower activity on subnanoclusters and SA is because they are limited by the dissociative adsorption step. Recalling Van der Hoeven et al. work [16] they found that on dilute Pd-in-Au allot nanoparticle catalysts an increase in Pd ensemble size results in an enhanced rate due to entropic effects, with a pronounced increase of the pre-exponential factors. The aforementioned is due to that for small ensembles

dissociative adsorption is not favored while the associative desorption step is more favored. Conversely, The opposite is true for big ensemble sizes. For our case of study using Pt, we observe a similar effect were the v_{des} values are bigger for the $Pt_{1.9nm}$ (v_{des} equal to 7.4 x $10^{15\pm0.2}$ than for the $Pt_{0.8nm-SA}$ (2.8 x $10^{15\pm0.1}$ 1/s, respectively). In contrast, Pt_{SA} showed a higher v_{des} value (1.4 x $10^{17\pm0.8}$) when compared to the $Pt_{1.9nm}$ but also a higher E_{des} (108 kJ/mol ± 3 vs 96± 1 kJ/mol for SA and NP, respectively) showing a compensation effect (increase in v_{des} accompanied by an increase on E_{des}) that can explain the differences in activity in the evaluated T range.

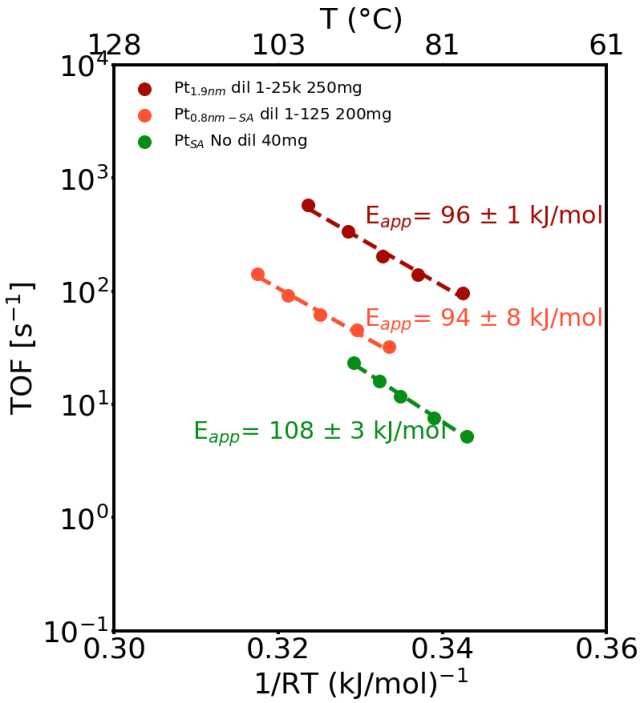

Figure 3.16: Arrhenius plot experiment for $Pt_{1.9nm}$ (red), $Pt_{0.8nm-SA}$ (orange) and Pt_{SA} samples. Total flow rate = 20 sccm, 5-5-10 sccm (H_2-D_2-Ar).

Another explanation for the lower activity but similar E*app* ranging from 94-108 kJ/mol can be due to the H/D exchange reaction taking place on the same type of sites. For this case, we suspect that the isotopic exchange reactions are taking place on the Pt atoms that form part of NP with a lower contribution from the nanoclusters and even lower to the negligible

Table 3.9: Kinetic parameters Pt/Al_2O_3 catalysts

	Kinetic parameters	Pt_{SA}	$Pt_{0.8nm-SA}$	$Pt_{1.9nm}$
Adsorption	E_{ads} [kJ/mol]	-	-	0 ±3
	v_{ads} [1/s/Pa]	-	-	2.8 x $10^{-1\pm0.2}$
Desorption	E_{des} [kJ/mol]	108 ±3	94 ±8	96 ±1
	v_{des} [1/s]	1.4 x $10^{17\pm0.8}$	2.8 x $10^{15\pm0.1}$	7.4 x $10^{15\pm0.2}$
	Heat of H_2 adsorption E_{ads} = E_{ads}- E_{des} [kJ/mol]	-108 ±3	-94 ±8	-96 ±4

contribution of activity from SA. The aforementioned was based on the percentage of NP and subnanoclusters present in each sample. By looking at the Atomic percentage from the STEM section (Appendix A): $Pt_{1.9nm}$ was mainly conformed by NP > 1nm and was also the catalysts that showed the greatest activity during the H/D exchange. Following we had the $Pt_{0.8nm-SA}$ that besides its average particle size it showed an atomic percentage of 12 % of NP. Lastly even though the Pt_{SA} sample was conformed by SA some subnanoclusters were detected in the STEM images (Figure A.4). Further evidence of a lower amount of NP and subnanoclusters on the different samples was previously shown in the DRIFTS results where the intensity in absorbance units for the CO-Pt interaction decreased sequentially by orders of magnitude for the $Pt_{1.9nm}$, $Pt_{0.8nm-SA}$, and Pt_{SA} samples as shown in Figure 3.2. Since no CO-Pt peak was detected for Pt SA we think that the differences in intensities are mainly due to the different Pt atomic % coming from NP and subnanoclusters present on the samples.

To have a deeper understanding of the difference in energy barriers it is important to recall the Bronsted Evan Polany principle. This model (equation 3.3) says that when starting from identical initial positions in the energy vs reaction coordinate diagram, the higher energy the final position has, the higher energy the transition point has (Fig 3.17). Thus it should've been expected that a decrease in E_{des} was accompanied by an increase in E_{ads}. For the $Pt_{1.9nm}$ an E_{ads}= 0 ± 3 was determined from the light-off experiments given that the pretreatment

temperatures of this sample allowed us to evaluate T as high as T=400 °C where coverage was close to 0. However, the determination of E_{ads} by evaluating activity at high temperatures (where coverage is close to 0) for the $Pt_{0.8nm-SA}$ and Pt_{SA} samples was difficult since these samples were reduced at 200 °C. Therefore, the evaluation at Temperatures above 200 °C where the coverage is considerably lower would imply the modification of the structure and particle size of the samples.

$$E = E^{\circ} + \alpha \Delta H \tag{3.7}$$

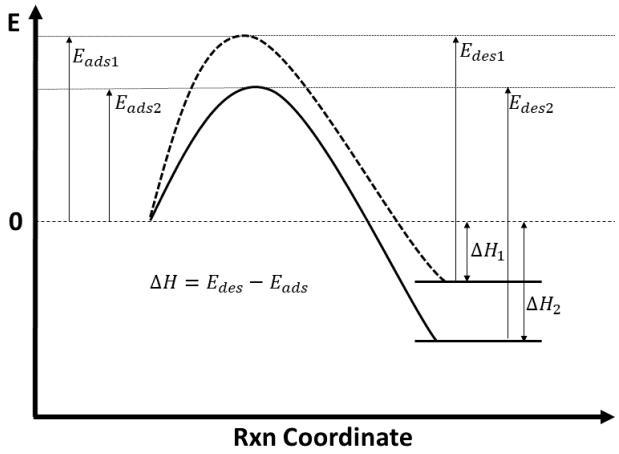

Figure 3.17: E vs Rxn coordinate diagram. BEP principle

3.7 Reaction mechanism for Pt/Al_2O_3 during H/D exchange reaction

r Vs P_{H_2} experiments were carried out in order to determine which reaction mechanism the H/D exchange follows on the Pt/Al_2O_3 catalysts. Recalling the reaction mechanism mentioned in the literature review for the H_2-D_2 isotopic exchange on Pt nanoparticles and when assuming full coverage [18], it is believed that the H/D isotopic exchange reactions can follow either the recombination mechanism, where all elementary steps are conformed by dissociative adsorption and associative desorption of the different isotopes (Reaction number 1-3 from Table 1.3) or the non-competitive adsorption mechanism where dissociative-recombination steps are followed by the surface reactions of molecular H_2/D_2 reacting with adatoms of H* and D* (Reaction number 4-5 from Table 1.3). Experimentally if the H/D isotopic exchange follows the recombination mechanism a maximum value of r_f is expected to appear while increasing P_{H_2} (equation 3.8). On the other hand, if the non-competitive adsorption is predominant the r_f should continue increasing with increasing P_{H_2} (equation 3.9).

However, given the importance of the coverage effects as a function of T and P discussed in the previous sections, we decided to include in this analysis the recombination mechanism when considering the coverage effect as well. When considering the presence of empty sites and when $P_{H_2} \neq P_{D_2}$ the resulting forward rate equation takes the shape of Equation 3.10. Determination of reactions rate equations 3.8,3.9 and 3.10 are described in Appendix C.4, C.5, and C.6 respectively.

The expected trends for r_f Vs P_{H_2} (with P_{D_2}= 12.5kPa) depending on the predominant reaction mechanism (Recombination and non-competitive adsorption when considering full coverage or recombination considering coverage effect) are shown in Figure 3.18. Impor-

tant to notice that for the recombination mechanism considering the coverage effect when P_{H_2}=12.5 kPa then θ=0.5 and when $_{H_2}$=75 kPa then θ=0.7. These coverage values as a function of T and P were determined from coverage value simulations (Equation 3.2) using the $Pt_{1.9nm}$ kinetic parameters (from Table 3.8).

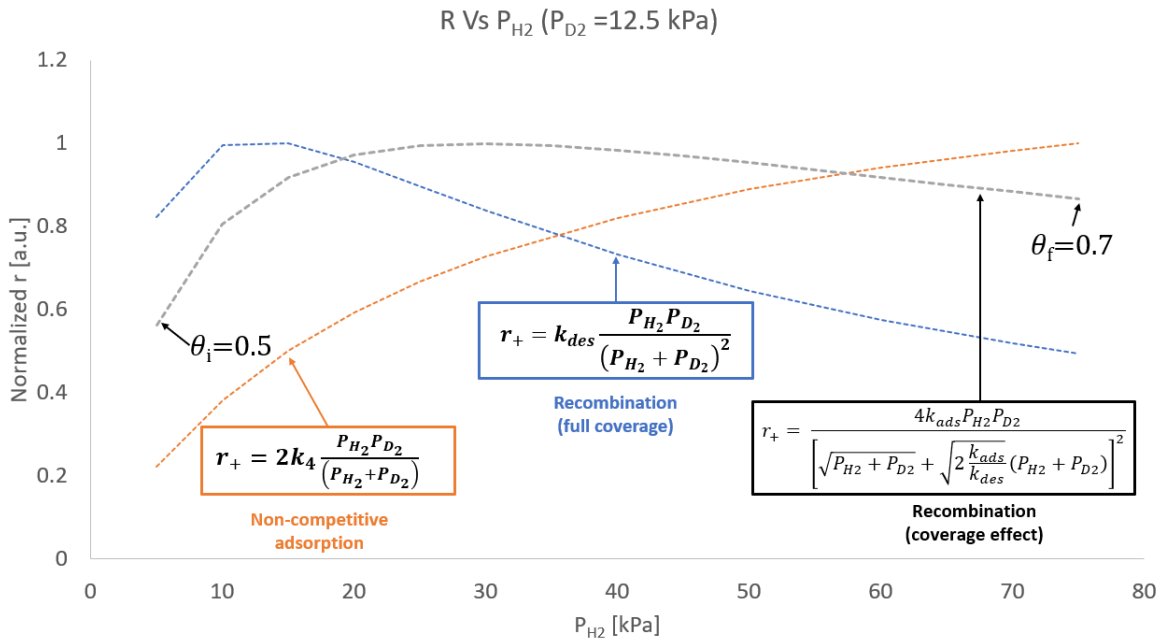

Figure 3.18: r Vs P_{H_2} theoretical trends for the recombination and non-competitive adsorption mechanisms assuming full coverage and recombination mechanism considering coverage effect. P_{D_2}=12.5kPa.

$$r_{HD,f} = k_{des}\frac{P_{H_2}P_{D_2}}{(P_{H_2}+P_{D_2})^2} \tag{3.8}$$

$$r_{HD,f} = 2k_4\frac{P_{H_2}P_{D_2}}{(P_{H_2}+P_{D_2})} \tag{3.9}$$

$$r_{HD,f} = \frac{4k_{ads}P_{H_2}P_{D_2}}{\left[\sqrt{P_{H_2}+P_{D2}}+\sqrt{2\frac{k_{ads}}{k_{des}}}(P_{H_2}+P_{D_2})\right]^2} \tag{3.10}$$

3.7.1 $Pt_{1.9nm}/Al_2O_3$ r Vs P_{H2} experiments

For the $Pt_{1.9nm}/Al_2O_3$ we carried out the r Vs P_{H_2} while keeping P_{D_2}=12.5 kPa and using a total flow of 20 sccm (5-5-10 sccm of H_2-D_2-Ar respectively). The temperatures of evaluation varied depending on the amount of catalyst placed inside the reactor. Conversion values were below 15% for all data points. In summary, when the experiment was carried out in the T range of 60-80 °C the r Vs P_{H_2} showed a profile with a maximum corresponding to the recombination mechanism in the full coverage regime (Figure 3.19). Contrasting, for the same sample with a different amount of catalyst and carried out inside a T range of 120-140 °C the r_f values continue increasing while increasing P_{H_2}, following the theoretical trend of the recombination mechanism when considering the coverage effect (Figure 3.20). We believe that this contrasting results for the same sample evaluated at different Temperatures are a direct consequence of the different coverage regimes under the $Pt_{1.9nm}$ activity was evaluated. When using the kinetic parameters previously determined for the $Pt_{1.9nm}$ in the r_f equation derived from the recombination mechanism considering the coverage effect (Equation 3.10), we found that at T=75 °C the model predicts the appearance of an r_f maximum at P_{H_2}=15 kPa, with $\theta > 0.95$ along the P_{H_2} modeled pressure range. On the other hand at T=130 °C the model predicts an r_f increase over P_{H_2}, with an increase of coverage from 0.5 to 0.7 for P_{H_2} equal to 5kPa and 75 kPa respectively (Figure 3.21). The importance of these simulation results relies on how the same mechanism, the recombination mechanism considering coverages effect as a function of T and P, predicts and explains both contrasting r_f Vs P_{H_2} trends that we got experimentally, where during evaluation in the high coverage regime r_f shows a maximum but at intermediate coverage values (i.e. between 0.50 and 0.70 for this case) r_f would show an increasing behavior over P_{H_2} predicted by theory and confirmed from experimental results as shown in Figures 3.19 and 3.20.

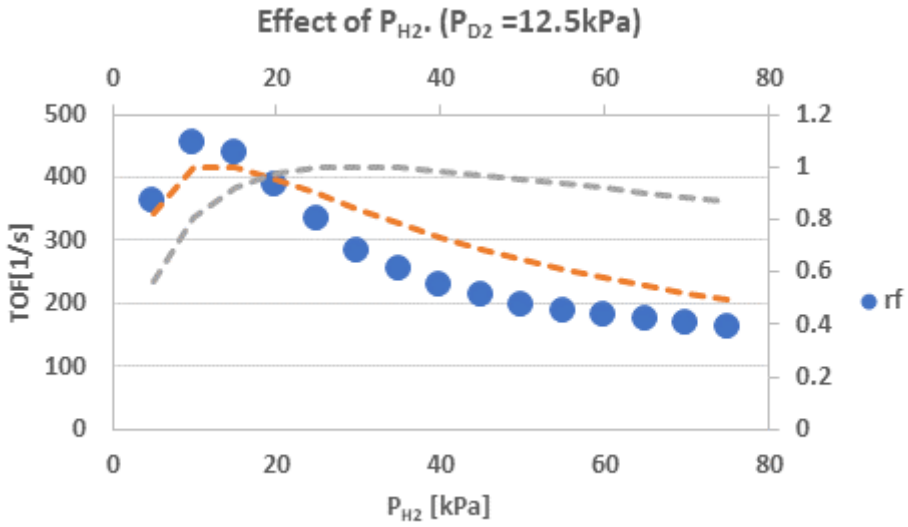

Figure 3.19: r_f vs P_{H_2} at 75 °C using a total flow rate of 20 sccm while keeping P_{D_2}=12.5 kPa for $Pt_{1.9nm}/Al_2O_3$. r_f:forward reaction rate. Blue dots: experimental data. Orange dash line: theoretical trend for recombination mechanism at full coverage. Gray dash line: theoretical trend for recombination mechanism considering coverage effect.

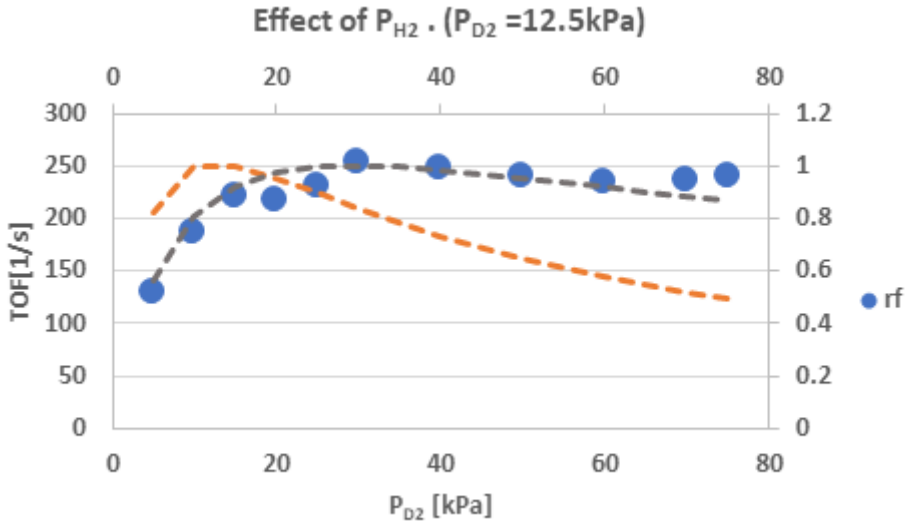

Figure 3.20: r_f vs P_{H_2} at 136 °C using a total flow rate of 20 sccm while keeping P_{D_2}=12.5 kPa for $Pt_{1.9nm}/Al_2O_3$. r_f:forward reaction rate. Blue dots: experimental data. Orange dash line: theoretical trend for recombination mechanism at full coverage. Gray dash line: theoretical trend for recombination mechanism considering coverage effect.

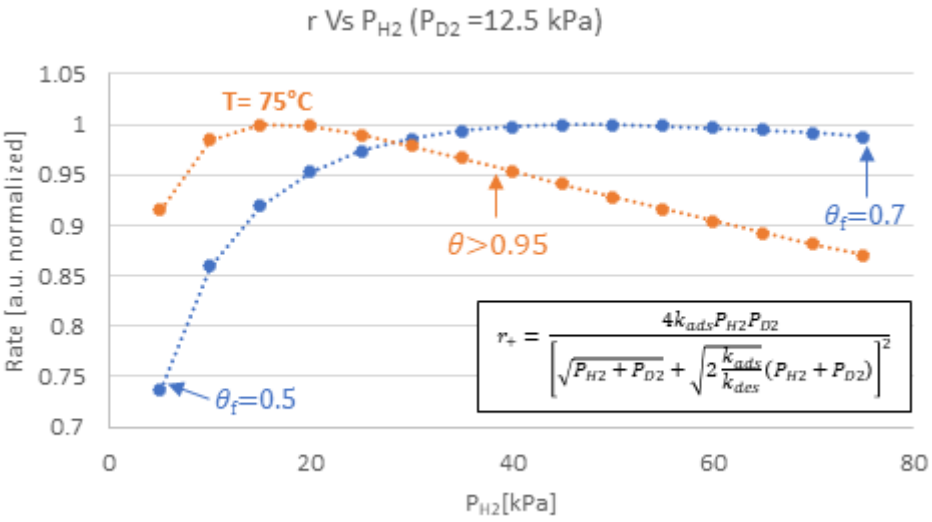

Figure 3.21: r Vs P_{H_2} theoretical trends for the recombination mechanisms considering coverage effect at T=75 °C and T=130 °C. P_{D_2}=12.5kPa.

3.7.2 $Pt_{0.8nm-SA}/Al_2O_3$ r Vs P_{H2} experiments

In order to compare the reaction mechanisms for different particle size regimes (subnanoclusters and SA instead of NP), r_f Vs P_{H2} were carried out on the $Pt_{0.8nm-SA}/Al_2O_3$ sample using a total flow of 20 sccm (5-5-10 sccm of H_2-D_2-Ar respectively). The amount of catalyst was varied in order to keep activity below 15% of conversion at different Temperatures through the different P_{H_2} points evaluated.

At higher T (110 °C) r_f continues increasing while increasing P_{H2} (Figure 3.22). In contrast at a lower T=75 °C, the r Vs P_{H_2} trending corresponds to the recombination reaction mechanism (Figure 3.23).

We believe that the difference in r trending is due to differences in coverage at the different T where activity was evaluated, similar to the $Pt_{1.9nm}/Al_2O_3$ case, where the recombination mechanism model considering coverage effect predicts both contrasting r_f Vs P_{H_2} trends depending on the coverage regime were activity was evaluated as a function of T and P_{H_2}.

Something relevant to notice is the difference in activity where a higher amount of Pt was required for the $Pt_{0.8nm-SA}$ sample in order to achieve similar conversion ranges than for the $Pt_{1.9nm}$ sample. This is in agreement with the difference in activity previously shown and discussed in section 3.6. The fact that the r Vs P_{H_2} followed similar trends at similar T even when contrasting particle sizes might be an indication that the H/D exchange reaction is still happening on the subnanoclusters and few NP percentages present on the $Pt_{0.8nm-SA}$ sample. As shown in the STEM images for $Pt_{0.8nm-SA}$ this sample still presents a small percentage of NP (10%) which is where activity might be coming from.

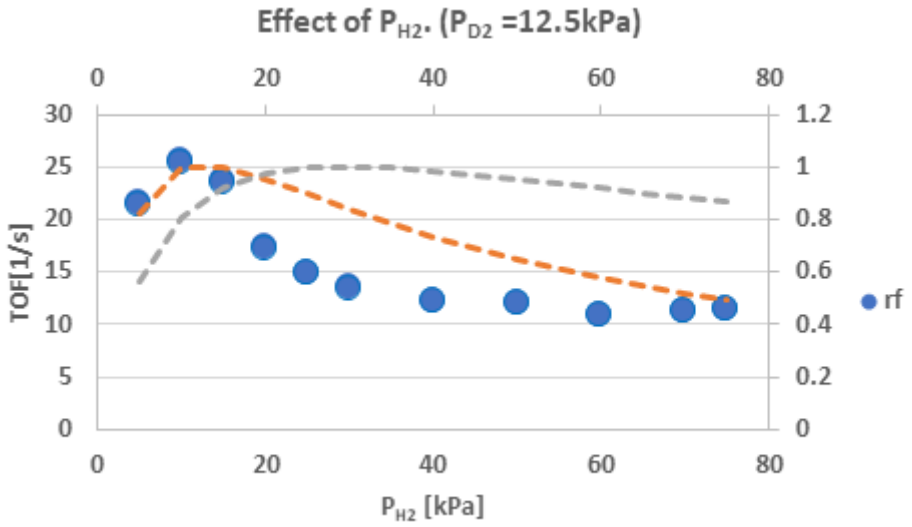

Figure 3.22: r_f vs P_{H_2} at 75 °C using a total flow rate of 20 sccm while keeping P_{D_2}=12.5 kPa for $Pt_{0.8nm-SA}/Al_2O_3$. r_f:forward reaction rate. Blue dots: experimental data. Orange dash line: theoretical trend for recombination mechanism at full coverage. Gray dash line: theoretical trend for recombination mechanism considering coverage effect.

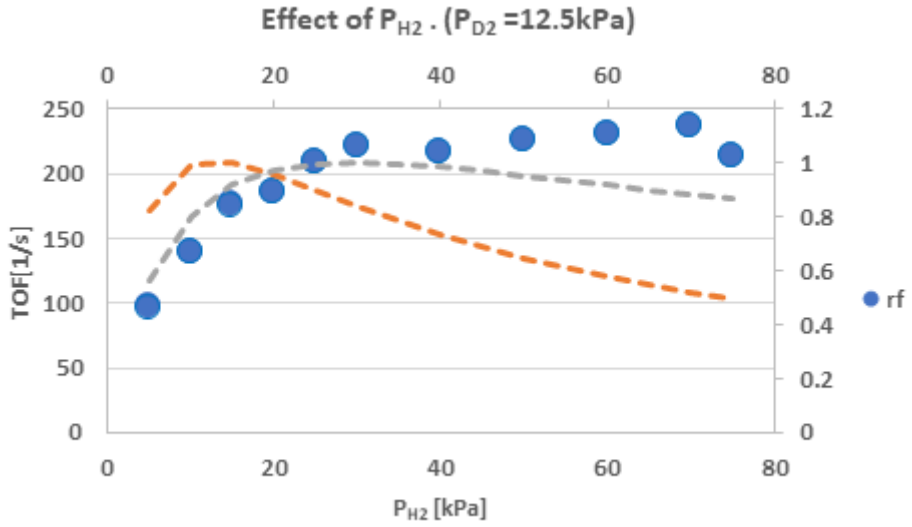

Figure 3.23: r_f vs P_{H_2} at 110 °C using a total flow rate of 20 sccm while keeping P_{D_2}=12.5 kPa for $Pt_{0.8nm-SA}/Al_2O_3$. r_f:forward reaction rate. Blue dots: experimental data. Orange dash line: theoretical trend for recombination mechanism at full coverage. Gray dash line: theoretical trend for recombination mechanism considering coverage effect.

3.7.3 Pt_{SA}/Al_2O_3 r Vs P_{H2} experiments

Similar to the previous two samples r Vs P_{H_2} experiments were carried out for the Pt_{SA}/Al_2O_3 at different temperatures.

At T=43 °C and using 50 mg of non-diluted catalysts the r_f Vs P_{H_2} showed the trend corresponding to the recombination mechanism Figure 3.24. In contrast at T=90 °C using 40 mg of catalyst, the r_f trend was similar to the one predicted by the recombination mechanism considering the coverage effect (Figure 3.25). Similar to the previous two samples ($Pt_{1.9nm}$ and $Pt_{0.8nm-SA}$) we believe that these contrasting results are due to differences in coverage values at the different temperatures evaluated.

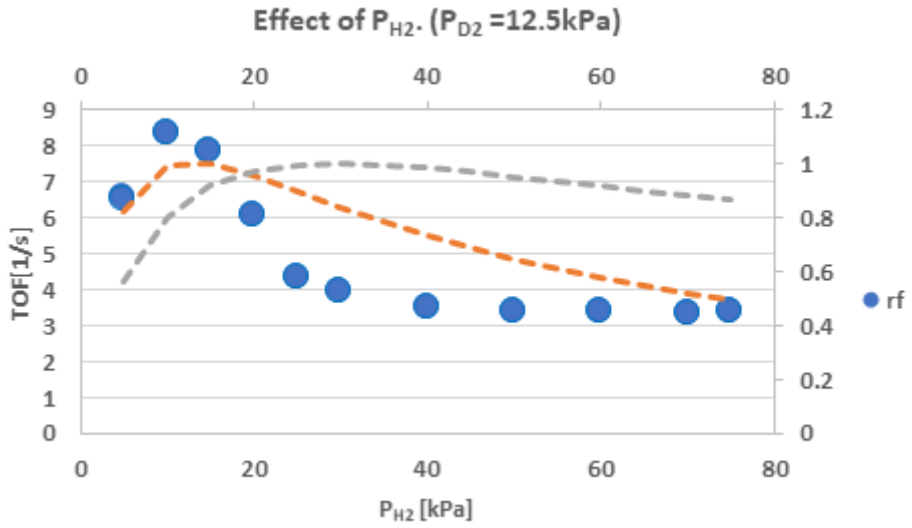

Figure 3.24: r_f vs P_{H_2} at 43 °C using a total flow rate of 20 sccm while keeping P_{D_2}=12.5 kPa for Pt_{SA}/Al_2O_3. r_f:forward reaction rate. Blue dots: experimental data. Orange dash line: theoretical trend for recombination mechanism at full coverage. Gray dash line: theoretical trend for recombination mechanism considering coverage effect.

It should be noted that the similitude between trends at different T but significantly lower TOF for this sample compared to $Pt_{1.9nm}$ and $Pt_{0.8nm-SA}$ might be an indication that in fact, the exchange reaction is mainly taking place on NP and subnanoclusters present in all

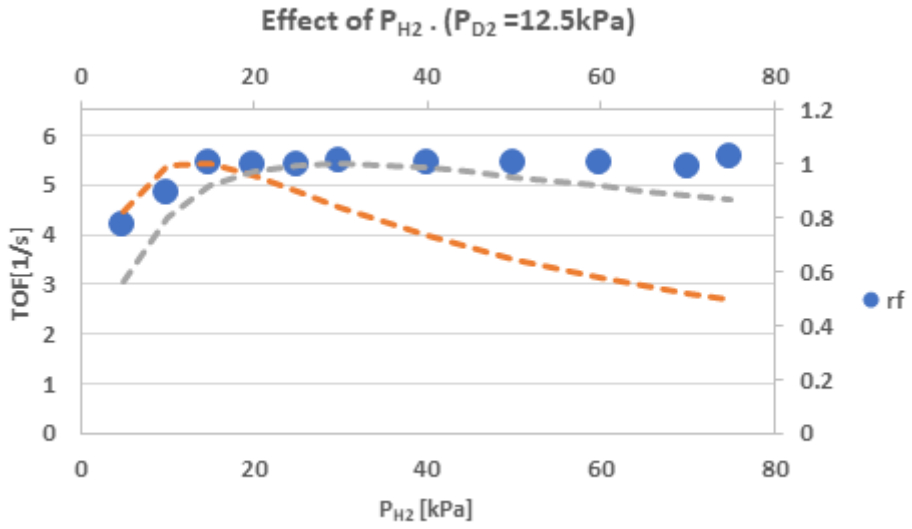

Figure 3.25: r_f vs P_{H_2} at 90 °C using a total flow rate of 20 sccm while keeping P_{D_2}=12.5 kPa for Pt_{SA}/Al_2O_3. r_f:forward reaction rate. Blue dots: experimental data. Orange dash line: theoretical trend for recombination mechanism at full coverage. Gray dash line: theoretical trend for recombination mechanism considering coverage effect.

samples. The aforementioned is due to the similar trends at different temperatures mainly due to differences in coverage on the NP and subnanoparticles over T as previously discussed. Further evidence of the exchange reaction taking place on similar sites is the similar E_{app} values shown in the structure sensitivity section (3.6) ranging from 94 to 108 kJ/mol for the $Pt_{1.9nm}$, $Pt_{0.8nm-SA}$ and Pt_{SA} sizes with significantly lower TOF as we decreased the particle sizes as shown in Figure 3.16. Furthermore, the intensity in absorbance units for the CO-Pt interactions determined in DRIFTS (Figure 3.2) changed by order of magnitude from $Pt_{1.9nm}$ to $Pt_{0.8nm-SA}$ to Pt_{SA} indicating of the presence of a substantially lower amount of Pt sites coming from NP and subnanoclusters.

Chapter 4

Summary and Conclusions

In summary, we characterize the different Pt/Al_2O_3 samples using different techniques such as CO and H_2 chemisorptions, CO-DRIFTS, and, STEM to determine differences in Pt particle sizes. The characterization results from the different methods indicate a difference in particle sizes that were strongly related to the nominal weight loadings of the samples, the calcination, and reduction temperatures with H_2. $5\%Pt/Al_2O_3$ with T_{cal}=T_{red}=400 °C resulted in the $Pt_{1.9nm}$ sample while the $0.05\%Pt/Al_2O_3$ sample with T_{cal}= 300 °C and T_{red}=250 °C resulted in the $Pt_{1.3nm}$ size. Different Pt precursors had an effect on the particle size as well were 0.01 and 0.05 % wt samples prepared using tetraamine Pt (II) nitrate with T_{cal}= 300 °C and T_{red}=200 °C resulting on the Pt_{SA} and $Pt_{0.8nm-SA}$ respectively.

Light-off (integral reactor model) and Arrhenius experiments results (differential reactor) were in good agreement regarding the numerical results obtained for the $Pt_{1.9nm}/Al_2O_3$ sample. Similar associative desorption parameter values E_{des} a v_{des} were determined from the different methodologies. Furthermore, the interpretation of the E_{app} depending on the coverage regime evaluated (low or high coverages at low and high temperatures respectively) was in agreement with the values we obtained experimentally. The heats of adsorption determined for this sample were inside the range of values reported in the literature from calorimetry and TPD experiments for similar particle sizes and Pt(111) lattice surface (Table 1.1).

E_{app} was shown to be affected by the coverage values (θ=f(T,P)) were activity was determined

for the $Pt_{1.9nm}$,$Pt_{0.8nm-SA}$ and Pt_{SA} samples. By applying the general apparent activation energy definition to the forward reaction rate equation derived from the microkinetic model for the recombination mechanism E_{app} is predicted to be proportional to coverage. Experimentally, the apparent activation energy determined at higher T and lower P_{H_2} and P_{D_2} showed lower E_{app} values compared to evaluation at lower temperatures and higher P_{H_2} and P_{D_2} as shown in section 3.5, showing the correlation of E_{app} with coverage predicted from the recombination mechanism microkinetic model.

Structure sensitivity effects were found on the Pt/Al_2O_3 samples reflected on different kinetic parameter values for dissociative adsorption and associative desorption values (E_{ads}, v_{ads}, E_{des}, v_{des}), for the different Pt particle sizes evaluated in this work ($Pt_{1.9nm}$,$Pt_{0.8nm-SA}$ and Pt_{SA}) Table 3.9. The bigger particle size, $Pt_{1.9nm}$, showed an overall greater activity than $Pt_{0.8nm-SA}$ and Pt_{SA} samples during the H/D isotopic exchange. When evaluating the activity in the high coverage regime we found similar E_{des} values (-96 $\pm$ 4, -94 $\pm$ 8 kJ/mol and 108 $\pm$ 3 kJ/mol respectively from NP, nanoclusters and SA), but different v_{des} values (7.3 x $10^{15\pm0.2}$,2.8 x $10^{15\pm0.1}$ and, 1.4 x $10^{17\pm0.8}$ 1/s for NP, subnanoclusters and SA respectively) suggesting that the source of the differences in activity has an entropic sources (difference in pre-exponential factors). We believe that decreasing activity while downsizing the particle size from $Pt_{1.9nm}$ to $Pt_{0.8nm-SA}$ to Pt_{SA} is strongly related to the Pt atomic % coming from NP and subnanoclusters. The aforementioned is based on the STEM and CO-DRIFTS results which shows lower atomic % of Pt atoms coming from NP and subnanoclusters and lower amount of Pt from NP and subnanoclusters respectively for the $Pt_{0.8nm-SA}$ and Pt_{SA} compared to the $Pt_{1.9nm}$, the most active catalysts during this case of study.

EXAFS experiments were carried out on the $Pt_{1.9nm}$ to verify whether or not the coordination of Pt atoms changed between room T and 400 °C. For the first time up today experimental evidence from the EXAFS fitting results for the $Pt_{1.9nm}$ sample under H_2 rich environment

was provided regarding reversible N_{Pt-Pt} and an anomaly in the decreasing trending over temperature. These N_{Pt-Pt} differences over T are relevant since they might be related to the 2D-3D Pt particle transition previously theorized to happen in the presence of oxygen vacancies on the Al_2O_3 in the presence of H_2O generated from the reduction steps. Moreover, a dip in activity during the H/D exchange at similar temperatures where the N_{Pt-Pt} trending changes happened was observed providing more evidence of potential structural changes at high T during the isotopic exchange reaction. For the smaller particle $Pt_{1.3nm}$ sample, EXAFS were performed to verify if different concentrations of H_2 were able to induce sintering of particles.

The r VS P_{H_2} experiments were carried out in order to determine the reaction mechanism the H_2-D_2 exchange follows on the $Pt_{1.9nm}$, $Pt_{0.8nm-SA}$, and Pt_{SA} samples. For all contrasting particle size samples, experiments carried out at temperatures below 80 °C showed a trend corresponding to the Recombination mechanism at coverage values close to 1 where the r_f values showed a maximum while increasing P_{H_2}. On the other hand at Temperatures above 90-100 °C the r_f showed an asymptotic increasing behavior while increasing P_{H_2}. We believe that the increase of r_f with P_{H_2} at higher T is derived from differences in coverage (low coverages or below saturation) where an increase in P_{H_2} will be derived in an increase of the reaction rate. Both contrasting trends were found to be in strong agreement with the trends predicted from the recombination mechanism under high coverage regime and when considering the coverage effect as a function of T and P_{H_2}.

The similarities in behavior for the different samples $Pt_{1.9nm}$, $Pt_{0.8nm-SA}$ and Pt_{SA} during r Vs P_{H2} experiments but pronounced decrease of activity determined from Arrhenius experiments while downsizing the particle size, indicates that the H/D reactions can be taking place mainly on the NP and subnanoclusters present on the samples with a very small or negligible contribution of the SA.

Appendices

Appendix A

Catalyst Synthesis and Characterization

A.1 Pt/Al_2O_3 synthesis by Wetness Impregnation

In this sections, we provide a calculation memory for the synthesis of 5%Pt/Al_2O_3 synthesized by Wet Impregnation method. γ-Al_2O_3 was previously calcined at 550 °C for 4 hours in a muffle furnace using a heating ramp of 5K/min. Pt precursor was a Chloroplatinic acid solution - 8 wt.% in H_2O Sigma-Aldrich

For 2g of support and 5%wt Pt

Mass of support: $m_{sup} = 2g$

Pt weight load % : x_{Pt}

Pt molecular weight: $M_{Pt} = 195.08$ g/g-mol

Pt precursor: Chloroplatinic acid solution - 8 wt.% in H_2O.

H_2Cl_6Pt molecular weight: $M_{Pt}^{prec} = 409.8$ g/g-mol

H_2Cl_6Pt acid solution density at 25°C: ρ_{prec}= 1.05 g/mL

H_2Cl_6Pt wt% concentration: $x_{prec} = 0.08$

To determine the amount of platinum we can use:

$$m_{Pt} = \frac{x_{Pt} m_{sup}}{1 - x_{Pt}} = \frac{0.05 * 2g}{1 - 0.05} = 0.1053g \tag{A.1}$$

To determine the mass of platinum precursor we can use:

$$m_{Pt}^{prec} = m_{Pt} \frac{M_{Pt}^{prec}}{M_{Pt}} = 0.105g \frac{409.81g}{195.084g} = 0.211g \tag{A.2}$$

To determine the volume of platinum precursor we can use:

$$Vol_{prec} = \frac{m_{Pt}}{\rho_{prec} * x_{prec}} = \frac{0.211g}{1.05g/mL * 0.08} = 2.632mL \tag{A.3}$$

The volume of precursor solution was then added to the 2g of support. An additional 2 mL of DI H_2O was added to help form the solution that was mixed for 2h and then left to dry out overnight at 60 °C on the heating plate. The resulting powder was calcined at 300 and 400 °C respectively for the 0.05 and 5% Pt/Al_2O_3 weight loadings.

A.2 Scanning Transmission Electron Microscopy

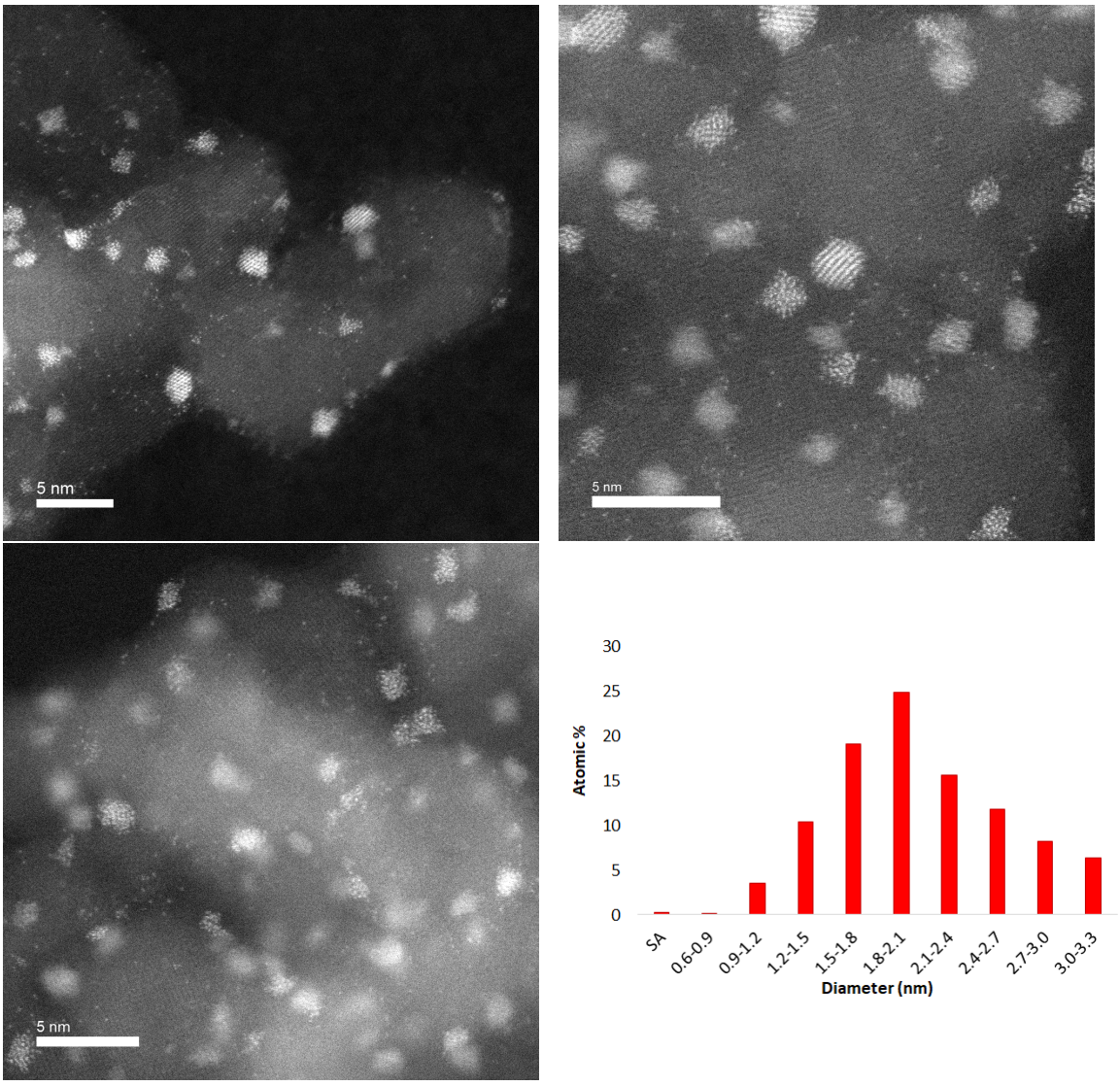

Figure A.1: HAADF-STEM images for 5%Pt/Al_2O_3 after reduction at 400 °C with H_2 and particle size distribution.$Pt_{1.9nm}/Al_2O_3$

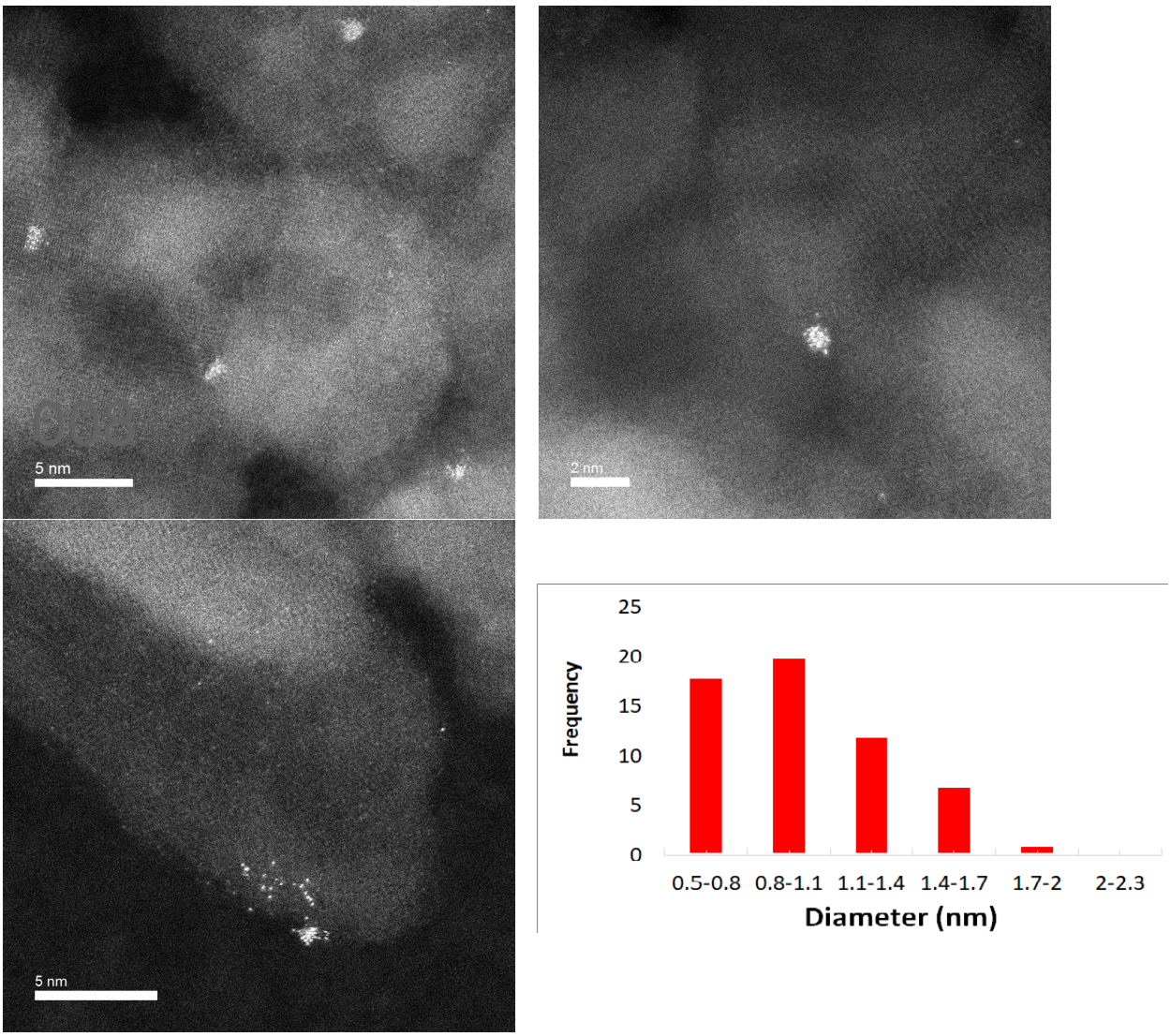

Figure A.2: HAADF-STEM images for 0.05%Pt/Al_2O_3 after reduction at 250 °C with H_2 and particle size distribution. $Pt_{1.3nm}/Al_2O_3$

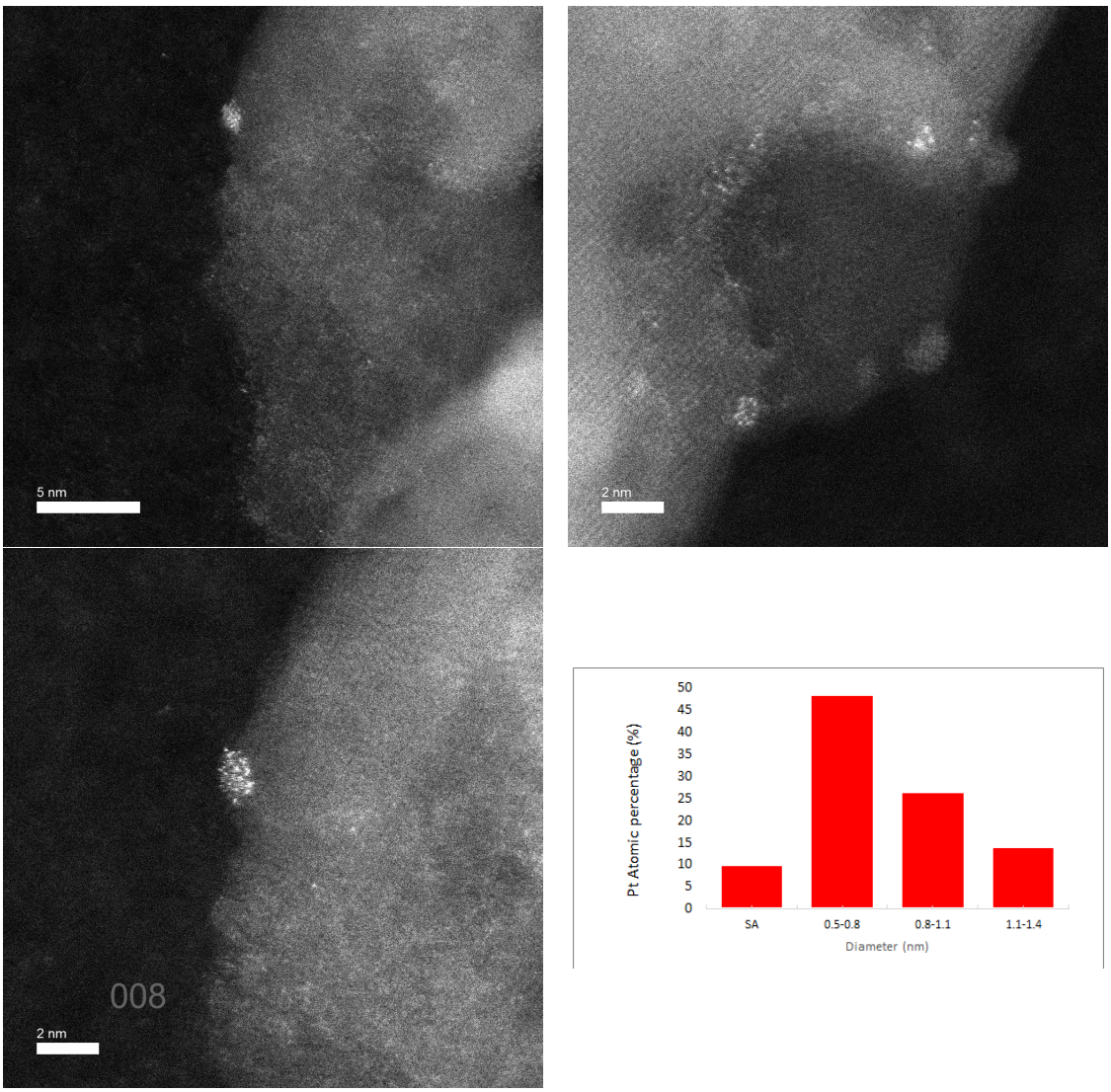

Figure A.3: HAADF-STEM images for 0.05%Pt/Al_2O_3 after reduction at 200 °C with H_2 (using tetraamine platinum as precursor) and particle size distribution. $Pt_{0.8nm-SA}/Al_2O_3$

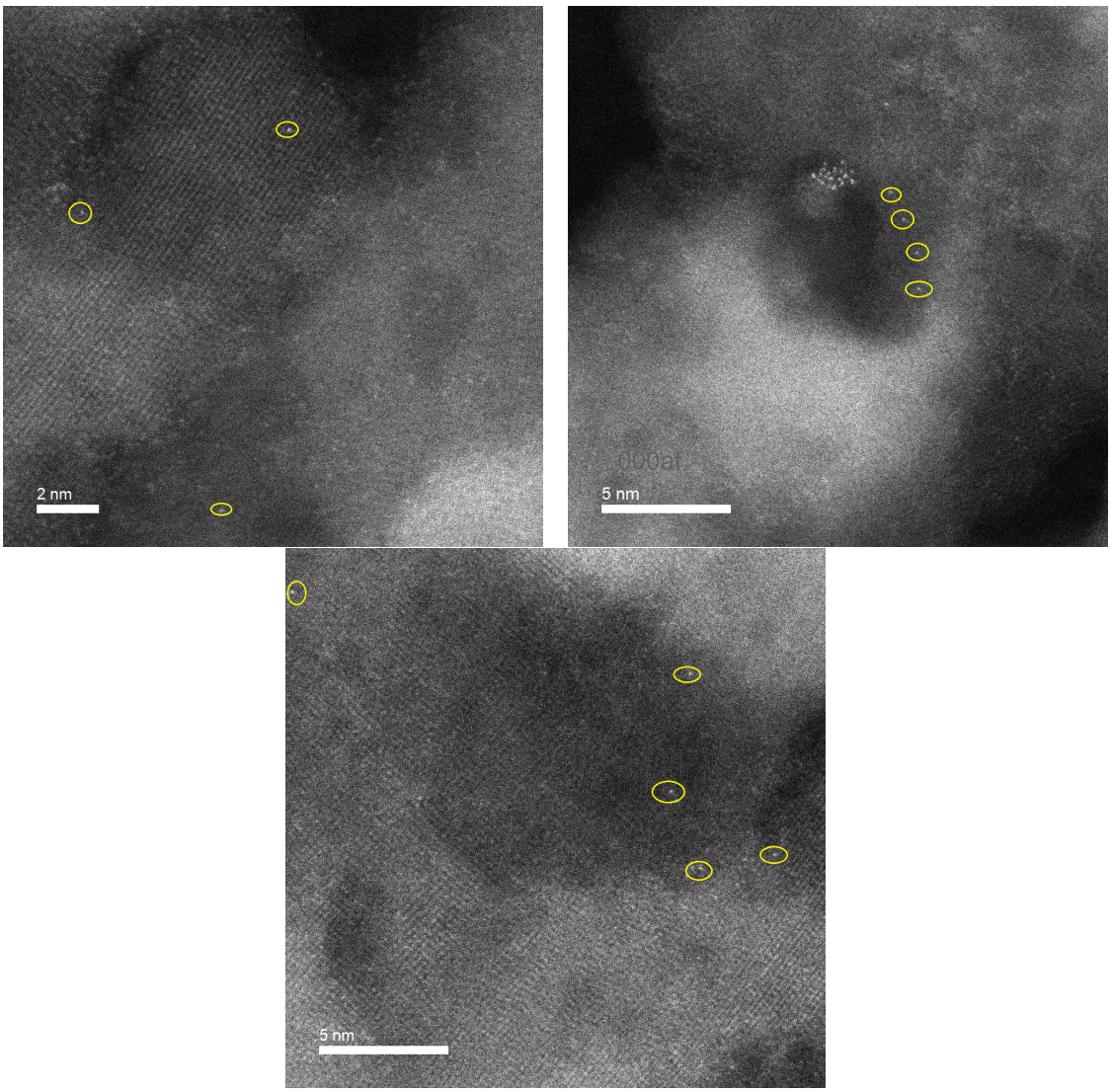

Figure A.4: HAADF-STEM images for 0.01%Pt/Al_2O_3 after reduction at 200 °C with H_2 (using tetraamine platinum as precursor).Pt_{SA}/Al_2O_3

A.3 DRIFTS

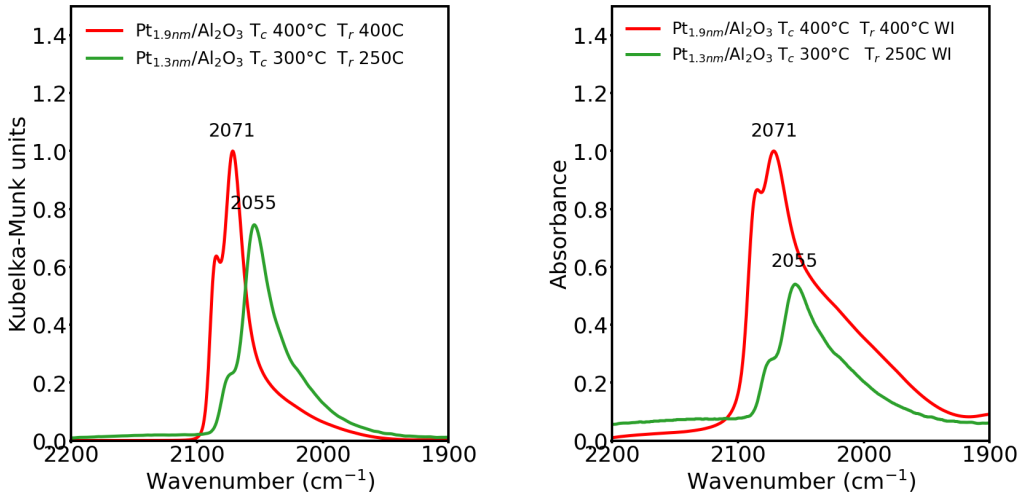

Figure A.5: DRIFTS spectra of CO adsorption on the Pt/Al_2O_3 samples after reduction in H_2 20% environment.

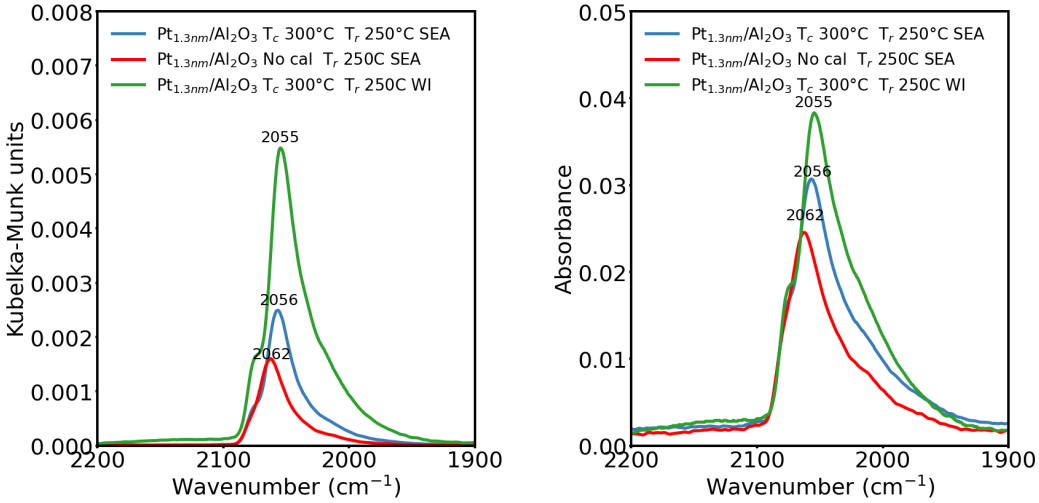

Figure A.6: DRIFTS spectra of CO adsorption on the $Pt_{1.3nm}/Al_2O_3$ samples after reduction in H_2 20% environment at different T_{red} and different synthesis methods in KM and Absorbance units.

Appendix B

Energy and Mass Transfer Limitations

In this section, we made use of different intraparticle and external mass and energy transfer limitations criteria to ensure that the catalytic activity was not affected by any transport phenomena effect. As a calculation example throughout this episode, we made use of the 5%Pt/Al_2O_3 physicochemical properties. The Meeting of the criteria for the other catalysts can be found at the end of this section.

B.1 Reactor dimensions and Operation conditions

Reactor diameter: R_d = 0.40 cm

Particle size: 106-180 μm ; Average particle diameter: d_p=0.0143 μm

Amount of catalyst: m= 300 mg = 3x10^{-4} kg

Total Flow rate: F_T = 20 sccm, 5-5-10 sccm (H_2,D_2,Ar)

B.2 External Mass Diffusion

The ratio of reactor length L to particle diameter d_p needs to satisfy the Satterfield criterion in order to avoid any axial dispersion effect which can prevent the system to achieve equilibrium conversion for the integral reactor case. Assuming a first-order reaction and plug-flow

we have:

$$\frac{L}{d_p} = \frac{20}{Pe_a} \ln \frac{1}{(1-X)} \tag{B.1}$$

where:

$$Pe_a = \frac{d_p U}{D_{AX}} \tag{B.2}$$

and

$$D_{AX} = D_{AB} + \frac{U^2 R_d^2}{192 D_{AB}} \tag{B.3}$$

Where the binary diffusion coefficient D_{AB} was determined for H_2 in Ar (carrier gas) using the Chapman-Enskog equation

For H_2 in Ar @373 K

D_{AB}=1.13 cm^2/s

@373K

U = 20 sccm = 0.455 cm^3/s

using B.3:

$$D_{AX} = 1.13 cm^2/s + \frac{(0.455 cm^3/s)^2 (0.40 cm)^2}{192 * (1.13 cm^2/s)} = 1.13 cm^2/s$$

$$Pe_a = \frac{(0.0143 cm)(0.455 cm^3/s)}{1.13 cm^2/s} = 0.045$$

And thus by considering conversion X=0.48 and using equation B.1

$$L > \frac{20}{Pe_a} \ln \frac{1}{(1-X)} * d_p = \frac{20}{0.045} \ln \frac{1}{(1-0.48)} * 0.0143cm = 4.1cm$$

So the bed length of the catalytic bed should be greater than 4.1 cm in order to avoid axial dispersion limitations.

B.3 Intraparticle Mass Difussion

To determine the intraparticle diffusion limitation we made use of the Weisz-Prater criterion:

$$\frac{k_1 \rho_c R_p^2}{D_e} < 0.6 \tag{B.4}$$

To determine D_e we made use of:

$$D_e = \frac{D_{AB} \phi \sigma}{\widetilde{\tau}} \tag{B.5}$$

Where:

ϕ:void fraction ≈ 0.4

σ: constriction factor≈ 0.8

$\widetilde{\tau}$:tortuosity ≈ 3

Therefore,

$$D_e = \frac{(1.13cm^2/s)(0.4)(0.8)}{3} = 0.121cm^2/s = 1.21x10^{-5}m^2/s$$

@373 K

$$k_1 = 2.1x10^{-4}\frac{m^3}{s * g_{cat}}$$

Bulk density:

$$\rho_b = \frac{m_{cat}}{\pi\left(\frac{R_d}{2}\right)^2 L} = \frac{1.2x10^{-2}g}{\pi * (0.2cm)^2) * 6.5cm} = 0.37\frac{g}{cm^3} = 370\frac{kg}{m3} \tag{B.6}$$

granule density:

$$\rho_c = \frac{\rho_b}{1-\phi} = \frac{370\frac{kg}{m^3}}{1-0.4} = 612\frac{kg}{m^3} \tag{B.7}$$

Substituting in B.4 we have:

$$\frac{k_1\rho_c R_p^2}{D_e} = \frac{2.1x10^{-4}\frac{m^3}{s*kg_{cat}} * 612\frac{kg}{m^3} * (1.4x10^{-4}m)^2}{1.21x10^{-5}\frac{m^2}{s}} = 0.041 < 0.6$$

Thus, there's no intraparticle mass transfer limitation.

B.4 Intraparticle heat transfer

To determine the intraparticle energy transfer limitation we made use of the Mears Criterion for Intraparticle Heat Transfer:

$$\frac{|\Delta H_R|\,\Re R_p^2 E_a}{\lambda_s T_0^2 R_g} < 0.75 \tag{B.8}$$

where

ΔH_R : the heat of reaction, 100000 J/mol

T_0: Temperature of the particle surface, 373K

E_a: Activation energy, 10000 J/mol

$\Re$: measured reaction rate per unit particle volume, 1.1 mol/(m^3*s)

λ_s: particle thermal conductivity, 25.3 W/mK

R_g: ideal gas constant, 8.314 K/molK

R_p: particle diameter, 1.43E-04 m

where the measured reaction rate per unit particle volume was determined using

$$\Re = \frac{k_1 \rho_b C_{H_2}}{1-\phi} = \frac{2.1x10^{-4} \frac{m^3}{s*g_{cat}} 370 \frac{kg}{m3} 8.2 \frac{mol}{m^3}}{1-0.4} = 1.1 \frac{mol}{m^3 * s}$$

$$\frac{|\Delta H_R| \, \Re R_p^2 E_a}{\lambda_s T_0^2 R_g} = \frac{100000 \frac{J}{mol} * 1.1 \frac{mol}{m^3 * s} (1.43x10^{-4})^2 * 10000 \frac{J}{mol}}{25.3 \frac{W}{mK} * (373K)^2 * 8.314 \frac{J}{molK})} = 5.81x10^{-6} < 0.75$$

Therefore, there are no intraparticle heat transfer limitations.

B.5 Interparticle heat transfer

To determine the interparticle energy transfer limitations we made use of the Mears criterion for radial heat transfer:

$$\frac{|\Delta H_R| \, \Re R_t^2}{\lambda_{eff} T_w^2 R_g E_a} \left(1 + \frac{4\lambda_{eff}}{R_d h_w}\right) < 0.4 \tag{B.9}$$

ΔH_R : the heat of reaction, 100000 J/mol

$\Re$: measured reaction rate per unit particle volume, 1.1 mol/(m^3*s)

R_t: Reactor radius, 2x10^{-3} m

λ_eff: particle thermal conductivity, 25.3 W/mK

T_w: Wall temperature, 373K

E_a: Activation energy, 10000 J/mol

R_g: ideal gas constant, 8.314 K/molK

where effective thermal conductivity was determined using

$$\lambda_{eff} = \lambda_g \beta \left(\frac{1-\phi}{\frac{\lambda_g}{\lambda_s} + \psi} \right) \tag{B.10}$$

and the gas thermal conductivity was determined using:

$$\lambda_g = y_{Ar}\lambda_A r + y_{H_2}\lambda_{H_2} + y_{D_2}\lambda_{D_2} \tag{B.11}$$

Considering

λ_{Ar}=0.023 W/mK

λ_{H2}=λ_{D2}=0.23 W/mK

by using B.11:

$$\lambda_g = (0.50)(0.023) + (0.25)(0.23) + (0.25)(0.23)\frac{W}{mK} = 0.13\frac{W}{mK}$$

by substituting using λ_g= 0.13 W/mK, β=1, ψ=0.04 and ϕ=0.4 in B.10 then:

$$\lambda_{eff} = \lambda_g \beta \left(\frac{1-\phi}{\frac{\lambda_g}{\lambda_s} + \psi} \right) = 0.13 \frac{W}{mK}(1) \left(\frac{1-0.4}{\frac{0.13 \frac{W}{mK}}{25.3 \frac{W}{mK}} + 0.04} \right) = 1.7 \frac{W}{mK}$$

to determine the wall heat transfer h_w:

$$h_w = \frac{1.2 \lambda_g}{d_p} = \frac{1.2 * 0.13 \frac{W}{mK}}{1.43 x 10^{-4} m} = 1060 \frac{W}{m^2 K} \tag{B.12}$$

When substituting all variables in B.9:

$$\frac{|\Delta H_R| \Re R_t^2 E_a}{\lambda_{eff} T_w^2 R_g} \left(1 + \frac{4 \lambda_{eff}}{R_t h_w} \right) =$$

$$\frac{\left|100000 \frac{J}{mol}\right| 1.1 \frac{mol}{m^3 s} (2 x 10^{-3} m)^2 (10000 \frac{J}{mol})}{1.7 \frac{W}{mK} (373 K)^2 (8.314 \frac{J}{molK})} \left(1 + \frac{4 * 1.7 \frac{W}{mK}}{(2 x 10^{-3} m) 1060 \frac{W}{m^2 K}} \right) = 0.01 < 0.4$$

Therefore, there are no interparticle heat transfer limitations.

Appendix C

Microkinetic model

C.1 Bonhoeffer-Farkas mechanism and Assumptions for H/D exchange

Derivation of rate equations for the integral and differential reactor models comes from the Bonhoeffer and Farkas mechanism for the H_2 - D_2 isotopic exchange on metal surfaces. The assumptions and elementary steps for this mechanism are the following:

1. H_2 and D_2 exchange reaction can be modeled by considering only dissociative adsorption and associative desorption of H_2, D_2 and HD under Steady-state conditions

2. Isotopic effect can be ignored (k_{ads} and k_{des} are the same for H_2, D_2 and HD).

3. The activation barrier and pre-exponent in the rate constant for adsorption and desorption are independent of coverage and temperature. This assumption is only needed for high coverages, or changing coverage at high exit conversion.

4. The coverages of H (θ_H) and D (θ_D) atoms are each assumed to be equal to one-half of the total coverage for an equimolar mixture of H_2 and D_2: $\theta_H = \theta_D = \frac{\theta}{2}$.

Table C.1: Bonhoeffer and Farkas mechanism

Reaction Number	Elementary step	σ
1	$H_2 + 2* \rightleftharpoons 2H*$	1
2	$D_2 + 2* \rightleftharpoons 2D*$	1
3	$H^* + D^* \rightleftharpoons 2HD + 2*$	2
Overall rxn	$H_2 + D_2 \rightleftharpoons 2HD$	

$\sigma : Horiuti's number$

C.2 Rate equation for integral model (High conversions)

The integral Mass balance on HD is:

$$\int_0^{F_{HD}} \frac{dF_{HD}}{r_{HD}} = m \tag{C.1}$$

For the high conversion case, we take into account the reversibility of all elementary steps stated in Table C.1. Departing from reaction 3 we got the following rate equation for HD

$$r_{HD} = 2k_{des}\theta_H\theta_D - k_{ads}P_{HD}(1-\theta)^2 = 2k_{des}\theta_H\theta_D - \frac{k_{ads}F_{HD}P_{total}(1-\theta)^2}{F_{total}} \tag{C.2}$$

where

$$F_{HD} = \frac{F_{total}P_{HD}}{P_{total}} \tag{C.3}$$

From assumption number 4:

$$\theta_H = \theta_D = \frac{\theta}{2} \tag{C.4}$$

When substituting C.4 in C.2 we got:

$$r_{HD} = 2k_{des}\left(\frac{\theta}{2}\right)^2 - \frac{k_{ads}F_{HD}P_{total}(1-\theta)^2}{F_{total}} \tag{C.5}$$

When substituting C.5 in C.1:

$$\int_0^{F_{HD,out}} \frac{dF_{HD}}{2k_{des}\left(\frac{\theta}{2}\right)^2 - \frac{k_{ads}F_{HD}P_{total}(1-\theta)^2}{F_{total}}} = m \tag{C.6}$$

Integrating C.6 and solving for $F_{HD,out}$ gives

$$F_{HD,out} = \frac{k_{des}}{k_{ads}}\frac{F_{total}\theta^2}{2P_{total}(1-\theta)^2}\left(1 - EXP\left(-\frac{mk_{ads}P_{total}(1-\theta)^2}{F_{total}}\right)\right) \tag{C.7}$$

The next step is to determine the value of θ. Using elementary steps 1 and 3 and assuming steady-state we can determine the rate equation for H atoms adsorbed:

$$r_{\theta_H} = 0 = 2k_{ads}P_{H_2}(1-\theta)^2 + k_{ads}P_{HD}(1-\theta)^2 - k_{des}\theta^2 = (1-\theta)^2 k_{ads}\left(P_{H_2} + \frac{P_{HD}}{2}\right) - \frac{k_{des}}{2}\theta^2 \tag{C.8}$$

From the molar balance taking into account the stoichiometry of the overall reaction we know that:

$$P_{H_2feed} = P_{H_2} + \frac{P_{HD}}{2} \tag{C.9}$$

When substituting C.9 in C.8 and after rearranging terms we end with the following quadratic equation:

$$r_{\theta_H} = 0 = \left(k_{ads}P_{H_2feed} - \frac{k_{des}}{2}\right)\theta^2 - 2k_{ads}P_{H_2feed}\theta - k_{ads}P_{H_2feed} \tag{C.10}$$

After solving the quadratic equation we end with the following equation for the total coverage:

$$\theta = \frac{\sqrt{2\frac{k_{ads}}{k_{des}}P_{H_2feed}}}{1 + \sqrt{2\frac{k_{ads}}{k_{des}}P_{H_2feed}}} \tag{C.11}$$

Finally when substituting the coverage equation C.11 into the integrated model equation C.7 we have:

$$F_{HD,out} = F_{H_2,feed}\left(1 - \exp\left(-\frac{mk_{ads}P_{total}}{F_{total}\left(1 + \sqrt{2\frac{k_{ads}}{k_{des}}P_{H_2feed}}\right)^2}\right)\right) \tag{C.12}$$

Equation C.12 represents the amount of HD produced in the integral reactor as a function of the amount of catalyst, the total pressure of the system, partial pressure of H_2, the total flow rate of the system, the flow rate of H_2 and the kinetic constant for dissociative adsorption and associative desorption.

$$k_{ads} = \nu_{ads}\exp\left(-\frac{\Delta E_{ads}}{k_bT}\right) \tag{C.13}$$

$$k_{des} = \nu_{des}\exp\left(-\frac{\Delta E_{des}}{k_bT}\right) \tag{C.14}$$

Equation C.12 was used to perform the non-linear fitting with the experimental data in order to extract the kinetic parameters using $F_{HD,exp}$ Vs T data, where k_{ads} and k_{des} have

Arrhenius forms

C.3 Differential reactor and apparent Activation energy interpretation (Low conversions)

The physical meaning of the kinetic parameters extracted from Arrhenius plots strongly depends on whether or not we are evaluating the activity in a low or high coverage region as a function of temperature.

Recalling the micro kinetic model described in C.1 but now, considering reaction number 3 is the rate determinant step we got the following mechanism:

Table C.2: Modified Bonhoeffer and Farkas mechanism

Reaction Number	Elementary step	σ
1	$H_2 + 2* \rightleftharpoons 2H*$	1
2	$D_2 + 2* \rightleftharpoons 2D*$	1
3 RDS	$H^* + D^* \rightharpoonup 2HD + 2*$	2
Overall rxn	$H_2 + D_2 \rightleftharpoons 2HD$	

$\sigma : Horiuti's number$

From reaction 3 (RDS) we can determine the rate equation for HD.

$$r_{HD} = 2k_{des}\left(\frac{\theta}{2}\right)^2 \tag{C.15}$$

Analysis for coverage determination is similar to the analysis described in Section C.2. After performing the respective analysis now taking into account reaction 3 as RDS we end with the same expression for coverage stated in equation C.11.

By definition in the high coverage region $\theta \rightarrow 1$ and $k_{ads} \gg k_{des}$. When taking this limit in

equation C.15 gives:

$$r_{HD} = 2k_{des} = 2\nu_{des} \exp\left(-\frac{\Delta E_{des}}{k_b T}\right) \tag{C.16}$$

After taking the natural logarithm on both sides:

$$\ln r_{HD} = \ln 2\nu_{des} - \left(\frac{\Delta E_{des}}{k_b T}\right) \tag{C.17}$$

Where Equation C.17 allowed us to extract the desorption kinetic parameters when evaluating the activity in the high coverage region.

By definition in the low coverage region $\theta \to 0$ and $k_{des} \gg k_{ads}$. When taking this limit in the coverage equation C.11 we have:

$$\theta = \sqrt{2\frac{k_{ads}}{k_{des}} P_{H_2 feed}} \tag{C.18}$$

When substituting C.18 in C.15 and after simplifying we got:

$$r_{HD} = P_{H_2 feed} k_{ads} = P_{H_2 feed} \nu_{ads} \exp\left(-\frac{\Delta E_{ads}}{k_b T}\right) \tag{C.19}$$

After taking the natural logarithm on both sides:

$$\ln r_{HD} = \ln P_{H_2 feed} \nu_{ads} - \left(\frac{\Delta E_{ads}}{k_b T}\right) \tag{C.20}$$

Where Equation C.20 allowed us to extract the adsorption kinetic parameters E_{ads} and k_{ads} when evaluating the activity in the low coverage region.

C.4 Differential reactor: Recombination mechanism full coverage and $\mathbf{P}_{H_2} \neq \mathbf{P}_{D_2}$

By departing from the same elementary steps stated in table C.2 from forward reaction 3 (RDS) we have:

$$r_{HD} = 2k_{des}\theta_H\theta_D \tag{C.21}$$

To determine θ_H and θ_D we made use of the pseudo-steady-state approximation for H* and D*.

So that for H* we have:

$$2k_{ads}P_{H_2}\theta_E^2 = k_{des}\theta_H^2 + k_{des}\theta_H\theta_D \tag{C.22}$$

analogously for D* we have:

$$2k_{ads}P_{D_2}\theta_E^2 = k_{des}\theta_D^2 + k_{des}\theta_H\theta_D \tag{C.23}$$

By equating both equations by using the term in common θ_E^2 we have:

$$\theta_E^2 = \frac{k_{des}\theta_H^2}{2k_{ads}P_{H_2}} + \frac{k_{des}\theta_H\theta_D}{2k_{ads}P_{H_2}} = \frac{k_{des}\theta_D^2}{2k_{ads}P_{D_2}} + \frac{k_{des}\theta_H\theta_D}{2k_{ads}P_{D_2}} \tag{C.24}$$

The previous equation can be simplified by Applying the assumption that the surface is covered that is:

$$\theta_H + \theta_D = 1 \tag{C.25}$$

So that when applying C.25 (θ_D=1-θ_H) in C.24 we have:

$$\frac{k_{des}\theta_H^2}{2k_{ads}P_{H_2}} + \frac{k_{des}\theta_H}{2k_{ads}P_{H_2}} - \frac{k_{des}\theta_H^2}{2k_{ads}P_{H_2}} = \frac{k_{des}}{2k_{ads}P_{D_2}} - \frac{k_{des}\theta_H}{k_{ads}P_{D_2}} + \frac{k_{des}\theta_H^2}{2k_{ads}P_{D_2}} + \frac{k_{des}\theta_H}{2k_{ads}P_{D_2}} - \frac{k_{des}\theta_H^2}{2k_{ads}P_{D_2}} \tag{C.26}$$

when simplifying we have:

$$\theta_H \left(\frac{k_{des}}{2k_{ads}P_{H_2}} + \frac{k_{des}}{2k_{ads}P_{D_2}} \right) = \frac{2k_{ads}k_{des}P_{D_2} + 2k_{ads}k_{des}P_{H_2}}{4k_{ads}^2 P_{H_2}P_{D_2}} = \frac{k_{des}}{2k_{ads}P_{D_2}} \tag{C.27}$$

So that H* coverage is equal to:

$$\theta_H = \frac{P_{H_2}}{P_{H_2} + P_{D_2}} \tag{C.28}$$

And analogously D* is equal to:

$$\theta_D = \frac{P_{D_2}}{P_{H_2} + P_{D_2}} \tag{C.29}$$

When substituting θ_H and θ_D in the HD forward rate equation (C.21) we have:

$$r_{HD} = 2k_{des}\frac{P_{H_2}P_{D_2}}{\left(P_{H_2} + P_{D_2}\right)^2} \tag{C.30}$$

Where equation C.30 represents the HD reaction rate equation when following the recombination mechanism and when assuming full coverage.

C.5 Differential reactor: Non-competitive adsorption mechanism full coverage and $\mathbf{P}_{H_2} \neq \mathbf{P}_{D_2}$

Table C.3: Alternative reactions mechanisms for H/D exchange

Reaction Number	Elementary step	σ
1	$H_2 + 2* \rightleftharpoons 2H*$	1
2	$D_2 + 2* \rightleftharpoons 2D*$	1
3	$H^* + D^* \rightarrow 2HD + 2*$	2
4	$H_2 + D* \rightarrow HD + H*$	1
5	$D_2 + H* \rightarrow HD + D*$	1
Overall rxn	$H_2 + D_2 \rightleftharpoons 2HD$	

$\sigma : Horiuti's number$

The rate for HD formation by following the reaction in table C.3 can be described by equation C.X which takes into account the contribution from both the dissociative adsorption reaction (Reaction number 3) and the reaction between H or D adatoms reaction with their respective molecular isotope (Reactions 4 and 5).

$$r_{HD} = 2k_{des}\theta_H\theta_D + k_4 P_{H_2}\theta_D + k_5 P_{D_2}\theta_H \tag{C.31}$$

However, when considering that the contribution from the recombination mechanism is considerably smaller than the HD coming from the reaction between adatoms and molecules and when considering $k_4 = k_5$ (kinetic isotopic effect ignored) the reaction rate equation for HD generation simplifies to:

$$r_{HD} = k_4 \left(P_{H_2}\theta_D + P_{D_2}\theta_H\right) \tag{C.32}$$

To determine θ_H and θ_D we made use of the pseudo-steady-state approximation for H* and

D*.

So that for H* we have:

$$2k_{ads}P_{H_2}\theta_E^2 + k_4\left(P_{H_2}\theta_D\right) = k_{des}\theta_H^2 + k_{des}\theta_H\theta_D + k_4\left(P_{D_2}\theta_H\right) \tag{C.33}$$

However, since dissociative adsorption and associative desorption steps are much slower than the reactions between H_2 and D* then the previous equation can be simplified to:

$$k_4\left(P_{H_2}\theta_D\right) = k_4\left(P_{D_2}\theta_H\right) \tag{C.34}$$

So that the coverage for H* is equal described by the following equation:

$$\theta_H = \frac{P_{H_2}}{P_{H_2} + P_{D_2}} \tag{C.35}$$

By performing a similar analysis for D* we got:

$$\theta_D = \frac{P_{D_2}}{P_{H_2} + P_{D_2}} \tag{C.36}$$

When susbstituting C.35 and C.36 in C.32 we end with the following rate equation:

$$r_{HD} = 2k_4\left(\frac{P_{H_2}P_{D_2}}{P_{H_2} + P_{D_2}}\right) \tag{C.37}$$

Where equation C.37 describes the HD reaction rate when considering that the contribution from the recombination mechanism is considerable smaller and slower compared to the HD coming from the non-competitive adsorption mechanism under full coverage.

C.6 Differential reactor:Recombination mechanism considering empty sites and $\mathbf{P}_{H_2} \neq \mathbf{P}_{D_2}$

By departing from the same elementary steps stated in table C.2 from forward reaction 3 (RDS) we have:

$$r_{HD} = 2k_{des}\theta_H\theta_D \tag{C.38}$$

To determine θ_H and θ_D we made use of the fact that reactions 1 and 2 are faster and under steady-state.

We got respectively Steady State approximation for H* and D*:

$$2k_{ads}P_{H_2}\theta_E^2 = k_{des}\theta_H^2 + k_{des}\theta_H\theta_D \tag{C.39}$$

$$2k_{ads}P_{D_2}\theta_E^2 = k_{des}\theta_D^2 + k_{des}\theta_H\theta_D \tag{C.40}$$

from where we can get a relation between θ_H and θ_D by diving the two previous equations

$$\frac{P_{H_2}}{P_{D_2}} = \frac{k_{des}\theta_H^2 + k_{des}\theta_H\theta}{k_{des}\theta_D^2 + k_{des}\theta_H\theta_D} = \frac{\theta_H}{\theta_D} \tag{C.41}$$

When substituting C.41 in C.39 we can get θ_H as a function of θ_E^2

$$\theta_H = \sqrt{2\frac{k_{ads}}{k_{des}}}\sqrt{\frac{1}{P_{H_2} + P_{D_2}}}P_{H_2}\theta_E \tag{C.42}$$

By using C.41 in C.42 we got for D*:

$$\theta_D = \sqrt{2\frac{k_{ads}}{k_{des}}}\sqrt{\frac{1}{P_{H_2}+P_{D_2}}}P_{D_2}\theta_E \tag{C.43}$$

When considering empty sites we have:

$$\theta_E + \theta_H + \theta_D = 1 \tag{C.44}$$

So that when substituting C.44 and C.45 in C.46 we can get an equation for θ_E

$$\theta_E + \theta_H = \sqrt{2\frac{k_{ads}}{k_{des}}}\sqrt{\frac{1}{P_{H_2}+P_{D_2}}}P_{H_2}\theta_E + \theta_H = \sqrt{2\frac{k_{ads}}{k_{des}}}\sqrt{\frac{1}{P_{H_2}+P_{D_2}}}P_{D_2}\theta_E = 1 \tag{C.45}$$

When isolating θ_E

$$\theta_E = \frac{1}{1+\sqrt{2\frac{k_{ads}}{k_{des}}}\sqrt{\frac{1}{P_{H_2}+P_{D_2}}}P_{H_2}\sqrt{2\frac{k_{ads}}{k_{des}}}\sqrt{\frac{1}{P_{H_2}+P_{D_2}}}P_{D_2}} \tag{C.46}$$

When susbstituting C.46 in C.42 and C.43 we have for θ_H and θ_D

$$\theta_H = \frac{\sqrt{2\frac{k_{ads}}{k_{des}}}\sqrt{\frac{1}{P_{H_2}+P_{D_2}}}P_{H_2}}{1+\sqrt{2\frac{k_{ads}}{k_{des}}}\sqrt{\frac{1}{P_{H_2}+P_{D_2}}}P_{H_2}\sqrt{2\frac{k_{ads}}{k_{des}}}\sqrt{\frac{1}{P_{H_2}+P_{D_2}}}P_{D_2}} = \frac{\sqrt{2\frac{k_{ads}}{k_{des}}}P_{H_2}}{\sqrt{P_{H_2}+P_{D2}}+\sqrt{2\frac{k_{ads}}{k_{des}}}(P_{H_2}+P_{D_2})} \tag{C.47}$$

$$\theta_D = \frac{\sqrt{2\frac{k_{ads}}{k_{des}}}P_{D_2}}{\sqrt{P_{H_2}+P_{D2}}+\sqrt{2\frac{k_{ads}}{k_{des}}}(P_{H_2}+P_{D_2})} \tag{C.48}$$

$$\theta_E + \theta_H = \sqrt{2\frac{k_{ads}}{k_{des}}}\sqrt{\frac{1}{P_{H_2} + P_{D_2}}}P_{H_2}\theta_E + \theta_H = \sqrt{2\frac{k_{ads}}{k_{des}}}\sqrt{\frac{1}{P_{H_2} + P_{D_2}}}P_{D_2}\theta_E = 1 \quad \text{(C.49)}$$

Finally, when substituting C.47 and C.48 in C.38 we have:

$$r_{HD} = \frac{4k_{ads}P_{H_2}P_{D_2}}{\left[\sqrt{P_{H_2} + P_{D2}} + \sqrt{2\frac{k_{ads}}{k_{des}}\left(P_{H_2} + P_{D_2}\right)}\right]^2} \quad \text{(C.50)}$$

Where equation C.49 describes the HD reaction rate when following the recombination mechanism and considering the presence of empty sites.

Appendix D

Mass Spectrometer calibration

For the quantitative analysis calibration of the Quadrupole Mass Spectrometer (QMS) was necessary. Before experimental session we perform both:

Offset calibration.

Mass scale adjust.

In this section, we provided an explanation of each type of calibration as well as instructions regarding how to perform it while operating a Pfeiffer Thermostar QMS 350 using the PVmassSpec software ©

D.1 Offset calibration

This type of calibration takes into account the electronic background or "dark current" of the amplifier measuring the ion current. It needs to be known and subtracted from the Ion current signals in order to have a representative quantitative measure. This type of calibration needed to be done at least every time the QMS is turned off.

To measure the dark current signal the equipment set up a Zero Mass which is a mass where there are no gas masses (i.e. 50.5 amu). The readings are saved and subtracted automatically from the Ion current signals during experiments after performing the offset calibration.

To perform this calibration using the PVMassSpec software ©we need to follow the following track as shown in Figure (X). Main Screen -> Maintenance -> Sensor maintenance -> Calibrate Amplifier offset

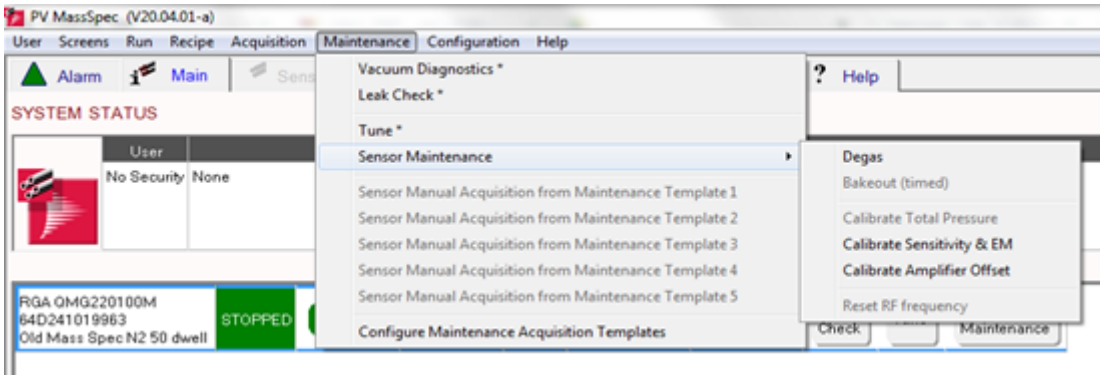

Figure D.1: Offset calibration route in PVMassSpec software ©

D.2 Mass Scale Adjust

In order to ensure a linear response between the Ion Current signals and concentration, the ion current needs to be measured at the tip of the mass peak. So, correction of the mass peak maximum for each mass-to-charge ratio m/z needs to be performed so that they hit the actual peak maxima (example in Fig D.2).

This calibration needs to be performed after changes of the QMS hardware and/or for each new reactive system (i.e. different concentrations and compositions of inlet gas, changes in substances present, different partial pressures, etc.).

To perform this correction in the PVMassSpec software ©we need to follow the route from the main display: Main Screen -> Maintenance -> tune.

Prior perform mass tunning we need to know the initial composition of all of the gasses to be tuned in the gas mixture. Warm-up of the filament and Secondary Electron Multiplier is

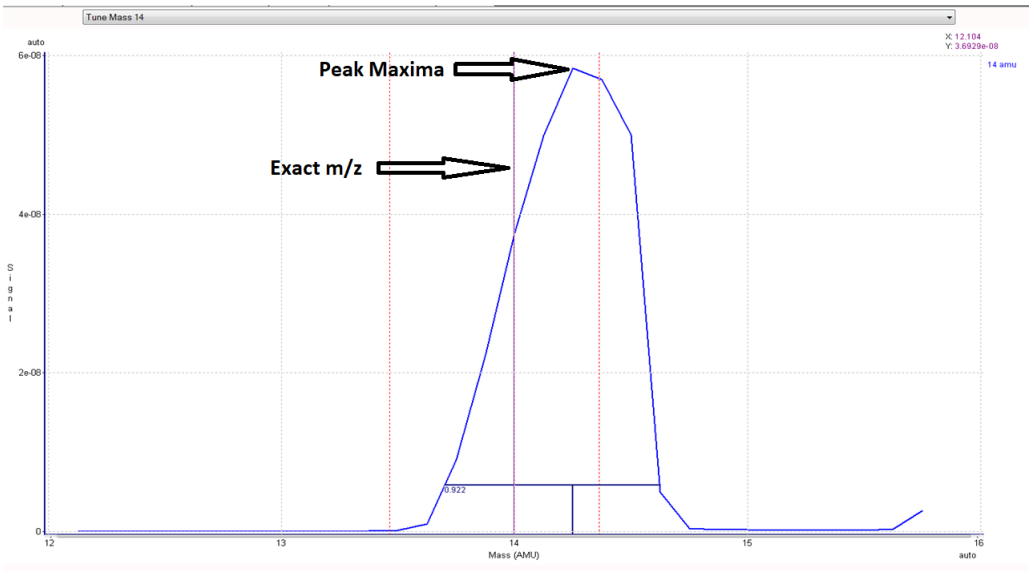

Figure D.2: exact m/z and peak maximum intensity difference example

needed for at least 1 hour.

In the Tune control we have the following options:

- Scan all masses. Performs a scan of all masses at the same time.
- Scan this mass. Performs a scan of the selected mass
- Auto calibrated all masses. Tunes all masses at the same time
- Auto calibrate this mass. automatically tunes the selected mass

After starting to flow the gas mixture for at least 1h we can select the Scan all masses option. this will automatically detect all substances present in the gas mixture. Next, we can select the Auto calibrate all masses option. Calibration takes around 5-15 minutes to perform. Whenever the analysis finishes we can click on the Configure button (on the right side corner Fig D.3) where we can see the corrected m/z values that actually hit the peak maxima.

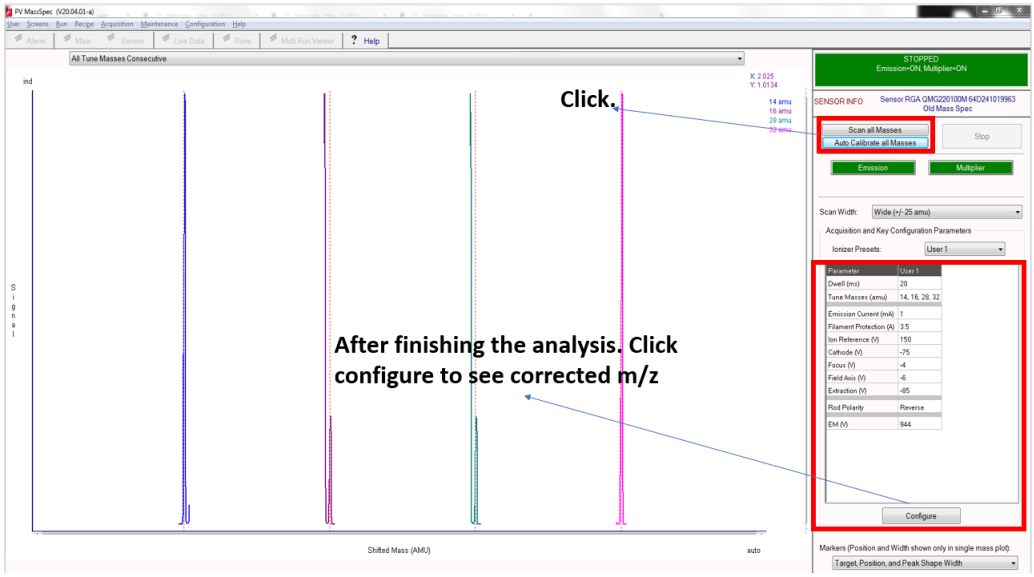

Figure D.3: tunning main screen and options example

In specific for this example as shown in Fig D.4 we can see how the m/z= 14, 16, 28, and 32 were corrected to 14.25, 16.25, 28.25, and 32.38 respectively. Is important to notice that the higher the Dwell value for all calibration functions (ms) the better the resolution of the peaks will be. However, this will also cause longer times to accomplish the calibration steps.

Mass corrections are automatically applied when saving the tuning results.

Calibration	
Dwell for all Calibration functions (ms)	20
Total Pressure calibration Slope (perform calibration to set)	1
Total Pressure calibration Intercept (perform calibration to set)	0
Tune masses	14, 16, 28, 32 **Corrected m/z**
Tune positions	14 (Actual=14.25), 16 (Actual=16.25), 28 (Actual=28.25), 32 (Actual=32.38)
Sensitivity and EM calibration Type	Specific mass
Sensitivity mass (AMU)	28
EM mass (AMU)	28
EM target Gain	1000
EM target Signal (A)	1e-08
EM target Signal/Pressure (A/P)	1
EM calibration Gain (perform calibration to set)	1000

Figure D.4: corrected m/z values related to the peak maximum for each substance

D.3 Base line effect on kinetic parameters

Throughout the evaluation of the catalytic activity for the differential reactor experiments (low conversions) using the MS we noticed that the baseline values for the HD ion current intensity signals can have a big impact on the E_{app} values depending on the conversion range was activity was evaluated. Here we define 3 different baselines that can be used to perform the quantitative analysis: bypass, reactor, and linear regression. The first two correspond to the signals recorded at room temperature through the bypass and reactor respectively. On the other hand, the baseline from linear regression refers to the value of the y-intercept from an experimental Ion current Vs conversion plot. Using the $Pt_{1.9nm}/Al_2O_3$ Arrhenius plots for the H/D isotopic exchange as an example we were able to notice that at conversions below 5% the value of the baseline has a bigger impact on the E_{app} ranging from 43 to 70 kJ/mol. This is because the ion current signals recorded for HD (m/z=3) are closer to the baseline intensity (Figure D.5). On the other hand, when activity is measured within a conversion range between 5-15 % the effect of the baseline value is less significant since the intensities recorded for HD are significantly greater than the baseline values (Figure D.6).

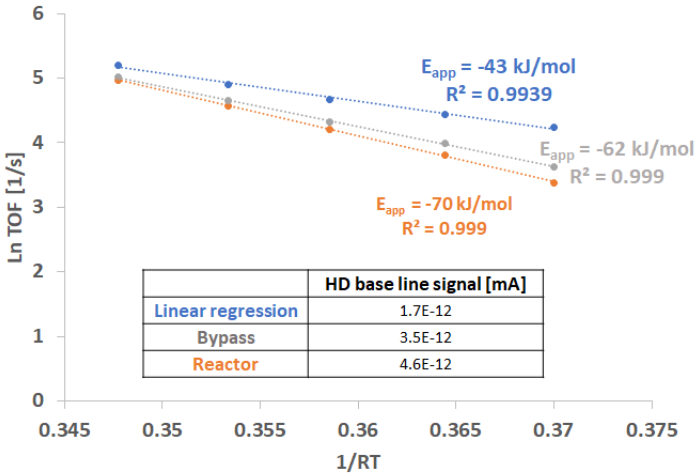

Figure D.5: Baseline values effect on Eapp at X<5% on the Arrhenius plots for $Pt_{1.9nm}/Al_2O_3$ sample for the HD isotopic exchange reaction

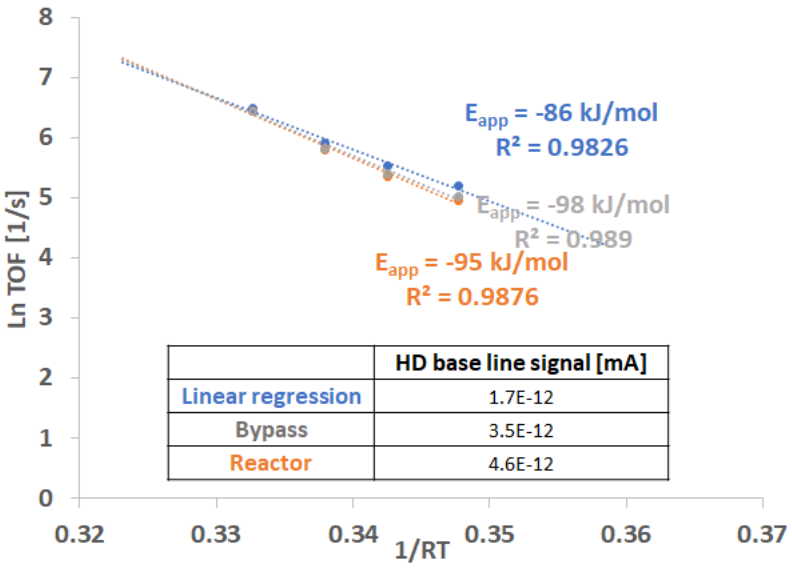

Figure D.6: Baseline values effect on Eapp at 5% < X < 15% on the Arrhenius plots for $Pt_{1.9nm}/Al_2O_3$ sample for the HD isotopic exchange reactio

Appendix E

Non-linear fitting Matlab Code

In this section, we described the code used to perform the non-linear fitting regression in order to minimize the error function (Equation 2.8) in order to extract the kinetic parameters from the light-off experiments.

We made use of the fminsearch function integrated into the Matlab software ©modified to allow us to set lower value boundaries when fitting the kinetic parameters. the maximum times of function evaluations and functions iterations (MaxFunEvals and MaxIter respectively) were set to 10,000. Tolerance of parameter X and of the function value (TolX and TolFun respectively) were set to 10E-16.

```
%%Experimental Data

T=[x1,x2.....xn]; % Temperature values from experimental light-off plot

FHDoutexp=[y1,y2.....yn]; % experimental HD flowrate in sccm

%% System pressures

PT=101325*1.2; %Total pressure of the system [Pa]
PH2feed= PT./4; %Total feed pressure of H2 [Pa]
```

```
PD2feed = PT./4; %Total feed pressure of D2 [Pa]

%% Volumetric flow
FT=20; %Total Vol flow of the system [sccm]
FH2feed=5; %Total Vol flow of H2 [sccm]
FD2feed =5; %Total Vol flow of D2 [sccm]

%%Kinetic Parameters
kb=0.00008617; %Boltzman constant [eV]
f=1.34*10^6; %unit conversion factor from mL/min to mol/s normal conditions
A=m ; %amount of platinum [g]


%%Error function equivalent to equation 2.8

fun=@(x) sum((((FH2feed.*(1-exp((-(10.^x(1).*exp(-x(3)./(kb.*T))).*PT.*A)
./(FT./f.*(1+(2*(10.^x(1).*exp(-x(3)./(kb.*T)))*PH2feed./(10.^x(2)
.*exp(-x(4)./(kb.*T)))).^(1/2)).^2))))- FHDoutexp)).^2)./size(T,2);

%%Initial guess
x0=[log10(Eads0),log(Ede0s),Ea0,Edes0]

%%Numerical solver part
%numerical solver options
options2= optimset('MaxFunEvals',10000,'MaxIter',10000,'TolX',10e-16,'TolFun'
,10e-16,'PlotFcns',@optimplotfval);
```

```
%parameters optimization
x = fminsearchbnd(fun,x0,[-20,-20,0,0],[],options2)



%%Print results
va=x(1)
vd=x(2)
Ea = x(3)
Ed = x(4)
```

E.1 Uncertainty determination

Standard deviations were determined using R. de Levie Algorithm for multi-parameter non-linear least-squares routines.

Assumptions:

- In fitting a function F(a_i) to N experimental data pairs x,y, all indeterminate uncertainties are restricted to y, and follow a single Gaussian distribution.
- numerical solver has already been used to find a solution y_{calc} based on a mathematical model expression of the type $y_{calc} = F(a_i)$, where a_i are the parameters adjusted
- Partial derivatives were determined using equation E.1 and E.2

$$y_{n_i} = \frac{\partial F_n}{\partial a_i} \tag{E.1}$$

$$\frac{\partial F_n}{\partial a_i} = \lim_{\Delta a_i \to 0} \frac{\Delta F_n}{\Delta a_i} \approx \frac{F_n\left(x_n, a_i(1+\delta), a_{j\neq i}\right) - F_n\left(x_n, a_i, a_{j\neq i}\right)}{a_i(1+\delta) - a_i} \tag{E.2}$$

Standard deviations were then determined by using E.5 following E.3 and E.4 definitions

$$P_{ij} = \sum_{n=1}^{N} y_{n,i} y_{n,j} \tag{E.3}$$

$$\chi^2 = \sum_{n=1}^{N} \left(y_{n,exp} - y_{n,calc}\right)^2 \tag{E.4}$$

$$\sigma_i = \sqrt{\frac{P_{ii}^{-1}\chi^2}{N-P}} \tag{E.5}$$

```
%%MATRIX
%Create new Matrix
P=zeros(4,4); % create Pi,J Matrix from equation E.3
delta=10^-8; % fix delta value for equation E.2

%%HD flow rate [sccm] computed from parameters previously determined
FHDcal=FH2feed.*(1-exp((-(10.^x(1).*exp(-x(3)./(kb.*T))).*PT.*A).
/(FT./f.*(1+(2*(10.^x(1).*exp(-x(3)./(kb.*T)))*PH2feed./(10.^x(2).
*exp(-x(4)./(kb.*T)))).^(1/2)).^2)));

%For vads
%HD flow rate [sccm] computed with delta increase in vads parameter
FHDcalvadsd = FH2feed.*(1-exp((-(10.^(x(1)+delta).*exp(-x(3)./(kb.*T))).*PT.*A).
```

```
/(FT./f.*(1+(2*(10.^(x(1)+delta).*exp(-x(3)./(kb.*T)))*PH2feed./(10.^x(2).
*exp(-x(4)./(kb.*T)))).^(1/2)).^2)));

%% Error function partial derivative with respect of vads
dFdvads=(FHDcalvadsd-FHDcal)./delta;

%% P(1,1) Matrix term
P(1,1)=sum(dFdvads.*dFdvads);

%For vdes
%HD flow rate [sccm] computed with delta increase in vdes parameter
FHDcalvdesd =FH2feed.*(1-exp((-(10.^x(1).*exp(-x(3)./(kb.*T))).*PT.*A).
/(FT./f.*(1+(2*(10.^x(1).*exp(-x(3)./(kb.*T)))*PH2feed./(10.^(x(2)+delta).
*exp(-x(4)./(kb.*T)))).^(1/2)).^2)));

 %% Error function partial derivative with respect of vdes
dFdvdes=(FHDcalvdesd-FHDcal)./delta;

%% P(2,2) Matrix term
P(2,2)=sum(dFdvdes.*dFdvdes);

%For Eads
%HD flow rate [sccm] computed with delta increase in Eads parameter
FHDcalEadsd = FH2feed.*(1-exp((-(10.^x(1).*exp(-(x(3)+delta)./(kb.*T))).*PT.*A).
/(FT./f.*(1+(2*(10.^x(1).*exp(-(x(3)+delta)./(kb.*T)))*PH2feed./(10.^x(2).
*exp(-x(4)./(kb.*T)))).^(1/2)).^2)));
```

```
% Error function partial derivative with respect of Eads
dFdEads=(FHDcalEadsd-FHDcal)./delta;

%% P(3,3) Matrix term
P(3,3)=sum(dFdEads.*dFdEads);

%For Edes

%HD flow rate [sccm] computed with delta increase in Edes parameter
FHDcalEdesd = FH2feed.*(1-exp((-(10.^x(1).*exp(-x(3)./(kb.*T))).*PT.*A).
/(FT./f.*(1+(2*(10.^x(1).*exp(-x(3)./(kb.*T)))*PH2feed./(10.^x(2).
*exp(-(x(4)+delta)./(kb.*T)))).^(1/2)).^2)));

% Error function partial derivative with respect of Edes
dFdEdes=(FHDcalEdesd-FHDcal)./delta;

%% P(4,4) Matrix term
P(4,4)=sum(dFdEdes.*dFdEdes);

%%Rest of Matrix elements.

P(1,2)=sum(dFdvads.*dFdvdes);
P(1,3)=sum(dFdvads.*dFdEads);
P(1,4)=sum(dFdvads.*dFdEdes);
```

```
P(2,1)=sum(dFdvdes.*dFdvads);
P(2,3)=sum(dFdvdes.*dFdEads);
P(2,4)=sum(dFdvdes.*dFdEdes);

P(3,1)=sum(dFdEads.*dFdvads);
P(3,2)=sum(dFdEads.*dFdvdes);
P(3,4)=sum(dFdEads.*dFdEdes);

P(4,1)=sum(dFdEdes.*dFdvads);
P(4,2)=sum(dFdEdes.*dFdvdes);
P(4,3)=sum(dFdEdes.*dFdEads);

%% Calculating uncertainties.
M=inv(P);
X=sum(((FHDoutexp-FHDcal).^2));

E1=((M(1,1).*X)./(size(T,2)-4)).^(1/2) %Uncertainty for vads

E2=((M(2,2).*X)./(size(T,2)-4)).^(1/2) %Uncertainty for vdes

E3=((M(3,3).*X)./(size(T,2)-4)).^(1/2) %Uncertainty for Eads

E4=((M(4,4).*X)./(size(T,2)-4)).^(1/2) %Uncertainty for Edes
```

Bibliography

[1] Gabor A. Somorjai and Jose Carrazza. Structure sensitivity of catalytic reactions. 25(1):63–69. Publisher: American Chemical Society.

[2] Lichen Liu and Avelino Corma. Metal catalysts for heterogeneous catalysis: From single atoms to nanoclusters and nanoparticles. 118(10):4981–5079. Publisher: American Chemical Society.

[3] Leilei Zhang, Maoxiang Zhou, Aiqin Wang, and Tao Zhang. Selective hydrogenation over supported metal catalysts: From nanoparticles to single atoms. 120(2):683–733.

[4] Jacques C. Védrine. Heterogeneous catalysis on metal oxides. 7(11).

[5] Chun-Te Kuo, Yubing Lu, Libor Kovarik, Mark Engelhard, and Ayman M Karim. Structure sensitivity of acetylene semi-hydrogenation on pt single atoms and subnanometer clusters. 9(12):11030–11041. Publisher: ACS Publications.

[6] Vladimir V. Zhivonitko, Kirill V. Kovtunov, Irene E. Beck, Artem B. Ayupov, Valerii I. Bukhtiyarov, and Igor V. Koptyug. Role of different active sites in heterogeneous alkene hydrogenation on platinum catalysts revealed by means of parahydrogen-induced polarization. 115(27):13386–13391. Publisher: American Chemical Society.

[7] M Vannice. Direct measurements of heats of adsorption on platinum catalysts i. h2 on pt dispersed on SiO2, al2o3, SiO2-al2o3, and TiO2. 95(1):57–70. 57.

[8] BE Spiewak and JA Dumesic. Microcalorimetric measurements of differential heats of adsorption on reactive catalyst surfaces. 290(1):43–53. Publisher: Elsevier.

[9] BE Spiewak, RD Cortright, and JA Dumesic. Microcalorimetric studies of h2, c2h4, and c2h2adsorption on pt powder. 176(2):405–414. Publisher: Elsevier.

[10] B. Hammer and J.K. Nørskov. Theoretical surface science and catalysis—calculations and concepts. In *Advances in Catalysis*, volume 45, pages 71–129. Academic Press.

[11] Matthias Batzill. Surface science studies of gas sensing materials: Sno2. 6(10):1345–1366. Publisher: Sensors (basel).

[12] Chang Lu, Ivan C Lee, Richard I Masel, Andrzej Wieckowski, and Cynthia Rice. Correlations between the heat of adsorption and the position of the center of the d-band: Differences between computation and experiment. 106(13):3084–3091. Publisher: ACS Publications.

[13] I. Toyoshima and G. A. Somorjai. Heats of chemisorption of o2, h2, CO, CO2, and n2 on polycrystalline and single crystal transition metal surfaces. 19(1):105–159. Publisher: Taylor & Francis.

[14] Itsuo Iida. The mechanism of catalyzed hydrogen–deuterium exchange on gold deposited over poly (tetrafluoroethylene). 52(10):2858–2862. Publisher: The Chemical Society of Japan.

[15] Casey P O'Brien, James B Miller, Bryan D Morreale, and Andrew J Gellman. The kinetics of h2–d2 exchange over pd, cu, and PdCu surfaces. 115(49):24221–24230. Publisher: ACS Publications.

[16] Jessi E. S. van der Hoeven, Hio Tong Ngan, Austin Taylor, Nathaniel M. Eagan, Joanna Aizenberg, Philippe Sautet, Robert J. Madix, and Cynthia M. Friend. Entropic control of HD exchange rates over dilute pd-in-au alloy nanoparticle catalysts. 11(12):6971–6981. Publisher: American Chemical Society.

[17] Jakob Nordheim Riedel, Marian David Rötzer, Mikkel Jørgensen, Ulrik Grønbjerg Vej-Hansen, Thomas Pedersen, Bela Sebok, Florian Frank Schweinberger, Peter Christian Kjærgaard Vesborg, Ole Hansen, and Jakob Schiøtz. H 2/d 2 exchange reaction on mono-disperse pt clusters: enhanced activity from minute o 2 concentrations. 6(18):6893–6900. Publisher: Royal Society of Chemistry.

[18] Samuel L. Leung, David Hibbitts, Mónica Gárcia-Diéguez, and Enrique Iglesia. Binding and exchange reactions of hydrogen isotopes on surfaces of dispersed pt nanoparticles. 126(8):3923–3938. Publisher: American Chemical Society.

[19] Alexander S. Lisitsyn and Olga A. Yakovina. On the origin of high-temperature phenomena in pt/al2o3. 20(4):2339–2350. Publisher: The Royal Society of Chemistry.

[20] Steven A. Bradley, Wharton Sinkler, Douglas A. Blom, Wilbur Bigelow, Paul M. Voyles, and Lawrence F. Allard. Behavior of pt atoms on oxide supports during reduction treatments at elevated temperatures, characterized by aberration corrected stem imaging. 142(2):176–182.

[21] Caroline Dessal, Alexis Sangnier, Céline Chizallet, Christophe Dujardin, Franck Morfin, Jean-Luc Rousset, Mimoun Aouine, Matthieu Bugnet, Pavel Afanasiev, and Laurent Piccolo. Atmosphere-dependent stability and mobility of catalytic pt single atoms and clusters on -al2o3. 11(14):6897–6904. Publisher: The Royal Society of Chemistry.

[22] Clelia Spreafico, Waiz Karim, Yasin Ekinci, Jeroen A. van Bokhoven, and Joost VandeVondele. Hydrogen adsorption on nanosized platinum and dynamics of spillover onto alumina and titania. 121(33):17862–17872. Publisher: American Chemical Society.

[23] Sune D. Ebbesen, Barbara L. Mojet, and Leon Lefferts. In situ ATR-IR study of CO adsorption and oxidation over pt/al2o3 in gas and aqueous phase: Promotion effects by water and pH. 246(1):66–73.

[24] John Meurig Thomas. Handbook of heterogeneous catalysis. 2., completely revised and enlarged edition. vol. 1–8. edited by g. ertl, h. knözinger, f. schüth, and j. weitkamp. 48(19):3390–3391. Publisher: John Wiley & Sons, Ltd.

[25] Donald A. McQuarrie. *Statistical Mechanics*. Harper & Row.